

Three-dimensional nanostructures,
pseudocapacitive materials and asymmetric
device configuration – Realizing high
performance supercapacitors

Dissertation

zur Erlangung des Doktorgrades

Dr. rer. nat.

vorgelegt der
Fakultät für Mathematik und Naturwissenschaften der
Technischen Universität Ilmenau

von
Dipl.-Phys. Fabian Grote
Ilmenau



TECHNISCHE UNIVERSITÄT
ILMENAU

Die Arbeit wurde von Prof. Dr. Yong Lei betreut.

1. Gutachter: Prof. Dr. Yong Lei
2. Gutachter: Prof. Dr. Heiko Jacobs
3. Gutachter: PD Dr. Andrea Balducci

Tag der Einreichung: 16.06.2015

Tag der wissenschaftlichen Aussprache: 23.10.2015

Throughout the duration of my Ph.D. I have obtained excellent results in the fields of nanotechnology and energy related applications. These results have been published in 12 papers in SCI-indexed international scientific journals, including *Nano Energy*, *Journal of Power Sources*, *Applied Physics Letters*, *Journal of Materials Chemistry A*, *Small*, *Journal of the American Chemical Society*, *Advanced Energy Materials*, *Advanced Materials* and *Nature Communication*. For more details please refer to the Section “Scientific contributions” on page 123.

Abstract

Supercapacitors are promising electrochemical energy storage devices which exhibit high specific power and long cycle life. However, the specific energy of supercapacitors needs to be enhanced to meet the increasing demands of modern technology. In order to target this challenge new pathways are developed within this thesis and are implemented into a device. Therefore, pseudocapacitive materials with high specific capacitance are utilized, the electrode kinetics and material utilization are optimized by introducing three-dimensional nanostructures, and a novel asymmetric device configuration is realized. An innovative and versatile fabrication process that allows the synthesis of dense three-dimensional nanotube arrays with structural control in the nanometer regime (e.g., length, spacing, diameter, wall thickness, coating, and the selection of open-end and closed-end nanotubes) is developed and three-dimensional nanotube arrays of different pseudocapacitive materials are fabricated, including core/shell nanotube arrays of $\text{SnO}_2/\text{MnO}_2$, SnO_2/PPy and C-TiN. Nano-porous anodic aluminum oxide serves as a template during the synthesis process and the active materials are processed by atomic layer deposition and electrochemical deposition. It is demonstrated that the realization of the three-dimensional nanoscale design of the electrodes in combination with pseudocapacitive materials and an asymmetric electrode configuration (PPy// MnO_2) leads to a supercapacitor device that experiences large specific energy while maintaining high specific power. Thereby, it has been found that one of the essential parameters to design high performance electrodes for supercapacitors is to optimize the utilization of the pseudocapacitive active electrode material by keeping its thin film morphology on a three-dimensionally nanostructured and electrical conductive matrix. Further, an innovative carbon coating technique is developed that can efficiently synthesize thin functional carbon films on three-dimensional nanotube arrays to improve the long-time cycling stability of supercapacitors. The achieved results within this work on three-dimensional nanostructuring and the integration in a supercapacitor device should provide a strong basis and guidance on the design and structure of the next generation of energy storage devices.

Zusammenfassung

Superkondensatoren sind vielversprechende elektrochemische Energiespeicher, die sich insbesondere durch hohe spezifische Leistung und exzellente Zyklenstabilität auszeichnen. Allerdings muss die spezifische Energie von Superkondensatoren deutlich erhöht werden, damit die Anforderungen moderner Technologien erfüllt werden. Um diese Herausforderung gezielt anzugehen werden im Rahmen dieser Arbeit neue Ansätze entwickelt und in ein vollständiges Bauelement implementiert. Hierzu werden pseudokapazitive Materialien mit hoher spezifischer Kapazität verwendet, die Elektrodenkinetik und Materialausnutzung mit Hilfe von dreidimensionalen Nanostrukturen optimiert und eine neuartige asymmetrische Elektrodenkonfiguration realisiert. Ein innovativer und vielseitiger Herstellungsprozess, welcher die Synthese von dicht angeordneten dreidimensionalen Nanoröhren-Arrays mit Strukturkontrolle im Nanometerbereich (z.B. Länge, Abstand, Durchmesser, Wandstärke, Beschichtung und die Auswahl von offenen und geschlossenen Nanoröhren) erlaubt, wird vorgestellt und dreidimensionale Nanoröhren-Arrays aus unterschiedlichen pseudokapazitiven Materialien werden hergestellt ($\text{SnO}_2/\text{MnO}_2$, SnO_2/PPy und C-TiN Kern / Mantel Nanoröhren-Arrays). Nanoporöses anodisches Aluminiumoxid dient als Templat während des Herstellungsprozesses. Die aktiven Elektrodenmaterialien werden mittels Atomlagenabscheidung und elektrochemischer Abscheidung prozessiert. Es wird gezeigt, dass die Realisierung eines dreidimensionalen nanoskaligen Elektrodendesigns in Kombination mit pseudokapazitiven Materialien und einer asymmetrischen Elektrodenkonfiguration (PPy/MnO_2) zu einem Superkondensator mit hoher spezifischer Energie führt. Es hat sich herausgestellt, dass die Optimierung der Ausnutzung des aktiven Elektrodenmaterials ein wesentlicher Parameter ist um Hochleistungselektroden für Superkondensatoren zu entwerfen. Dabei ist insbesondere die Herstellung von dünnen aktiven Schichten auf einer dreidimensionalen nanostrukturierten und elektrisch leitfähigen Matrix vorteilhaft. Darüber hinaus wird eine innovative Kohlenstoffbeschichtungstechnik entwickelt, die es erlaubt, dünne funktionale Kohlenstoffschichten auf dreidimensionalen Nanoröhren-Arrays abzuscheiden. Die im Rahmen dieser Arbeit erzielten Ergebnisse, in Bezug auf dreidimensionale Nanostrukturierung und die Integration in Superkondensatoren, sollten eine starke Basis darstellen um das Design und den Aufbau der nächsten Generation von elektrochemischen Energiespeichern zu optimieren.

Table of Contents

Table of Contents	I
List of Figures	IV
List of Tables	VII
List of Abbreviations	VIII
1 Introduction	1
2 Electrochemical energy storage in supercapacitors	7
2.1 How to distinguish supercapacitor from battery type energy storage? Intrinsic properties of supercapacitor materials	9
2.2 Electric double-layer capacitance.....	10
2.3 Pseudocapacitance.....	11
2.4 Supercapacitor materials	14
2.4.1 Carbon	15
2.4.2 Graphene	15
2.4.3 Electrically conductive polymers.....	16
2.4.4 Metal oxides	17
2.4.5 Metal nitrides.....	19
2.5 Symmetric and asymmetric aqueous based supercapacitors.....	19
2.6 Confusion and uncertainty concerning supercapacitor device performance reported in literature	21
3 Three-dimensional nanostructures: Fabrication strategies and advantages for supercapacitor applications.....	23
3.1 Advantages of three-dimensional and complex core/shell nanostructured materials in supercapacitor applications.....	23
3.2 Atomic layer deposition	25
3.3 Anodic aluminum oxide a nano-porous template for three-dimensional nanostructuring	27

Table of Contents

3.3.1	Structural features of anodic aluminum oxide	28
3.3.2	Formation process of anodic aluminum oxide	31
3.3.3	Steady-state growth of anodic aluminum oxide	31
3.4	Electrochemical deposition and polymerization	32
3.4.1	Electrochemical deposition of manganese dioxide.....	33
3.4.2	Electrochemical polymerization of pyrrole	33
3.5	Functional carbon coating to improve the performance of energy devices – Challenges for three-dimensional nanostructures	34
4	Experiments and methods	37
4.1	Template assisted fabrication of three-dimensional nanostructures.....	37
4.1.1	Anodic aluminum oxide template	37
4.1.2	Atomic layer deposition of SnO ₂	38
4.1.3	Open-end and closed-end SnO ₂ nanotube arrays.....	39
4.1.4	Electrochemical deposition of MnO ₂ and PPy	39
4.1.5	Synthesis of micelles and carbon coating of anodic aluminum oxide	40
4.1.6	Atomic layer deposition of TiN and electrode fabrication.....	40
4.2	Analytical methods.....	41
4.2.1	Field emission scanning electron microscopy	41
4.2.2	Transmission electron microscopy	42
4.2.3	X-ray photoelectron spectroscopy	43
4.2.4	Raman spectroscopy and FTIR.....	43
4.2.5	X-ray diffraction spectroscopy	43
4.2.6	Electrochemical characterization.....	43
5	Results and discussion	47
5.1	Positive electrode: Three-dimensional core/shell SnO ₂ /MnO ₂ nanotube array..	47
5.1.1	SnO ₂ nanotube array	48
5.1.2	SnO ₂ /MnO ₂ core/shell nanotube array	53
5.1.3	Electrochemical performance.....	56

Table of Contents

5.2	Negative electrode: Three-dimensional core/shell SnO ₂ /PPy nanotube array ...	61
5.2.1	Structural investigation	61
5.2.2	FTIR and Raman spectroscopy	63
5.2.3	Electrochemical performance	64
5.3	Asymmetric PPy//MnO ₂ supercapacitor	67
5.3.1	The device operating potential window: Synergetic effect from the asymmetric configuration	67
5.3.2	Electrochemical performance of the asymmetric PPy//MnO ₂ device	69
5.4	Three-dimensional C-TiN and TiN nanotube arrays: Improving the cycling stability of metal nitrides in aqueous supercapacitors	74
5.4.1	Structural investigation	74
5.4.2	Electrochemical performance	79
6	Summary and outlook	83
7	Bibliography	85
8	Appendix	109
	Acknowledgment	121
	Scientific contributions	123
	Extended work	129

List of Figures

2 Electrochemical energy storage in supercapacitors

2-1 Specific power vs. specific energy, also called Ragone plot.....	7
2-2 The different mechanisms of capacitive energy storage.....	9
2-3 Redox reactions leading to pseudocapacitance.	13
2-4 Reported specific capacitance values in literature.....	14
2-5 Comparison of the rate capability of various MnO ₂ based structures	18
2-6 Ragone plot, showing reported specific energy (E) and specific power (P_{real}) values	21

3 Three-dimensional nanostructures: Fabrication strategies and advantages for supercapacitor applications

3-1 Illustration of an ideal 3D supercapacitor electrode.....	25
3-2 Simplified 4 step process of ML by ML film growth in ALD.	26
3-3 ALD window for conformal ML by ML growth in dependence on the deposition temperature.....	27
3-4 Self-organized nano-porous AAO template.....	28
3-5 Pore widening of an AAO template.....	29
3-6 Summary of reported self-ordering regimes of AAO templates	30
3-7 Comparison between conventional and pre-structured AAO templates.....	30
3-8 Schematic illustration of AAO formation	31
3-9 Potential vs. pH diagram for the Mn–O ₂ –H ₂ –H ₂ O system.....	33
3-10 Reaction scheme of the electrochemical polymerization of pyrrole	34

4 Experiments and methods

4-1 The flowchart displays the procedure to fabricate high quality nano-porous AAO templates	38
4-2 ALD process for the fabrication of SnO ₂	39
4-3 ALD process for the fabrication of TiN.....	41
4-4 Swagelok type two-electrode measurement setup	44

5 Results and discussion

5-1 Schematic diagram, illustrating the fabrication processes of (a) open-end SnO ₂ /MnO ₂ nanotube arrays and (b) closed-end SnO ₂ /MnO ₂ nanotube arrays	48
5-2 SnO ₂ deposited inside the AAO pores.....	49
5-3 Cross-section SEM analysis of the SnO ₂ nanotube length	50

List of Figures

5-4 Cross-section SEM investigation of the SnO ₂ nanotube opening	51
5-5 Top view SEM images of the self-supported (a) closed-end SnO ₂ nanotube array and (b) open-end nanotube array	51
5-6 TEM investigation of a SnO ₂ nanotube	52
5-7 XPS spectrum of the Sn 3d orbital of the ALD prepared SnO ₂ nanotube array	53
5-8 SEM investigation of the o-SnO ₂ /MnO ₂ nanotube array	53
5-9 Investigation of the elemental distribution of Mn, Sn and O across a single SnO ₂ /MnO ₂ core/shell nanotube by EDX mapping and EDX line scan performed in TEM. ^[13]	54
5-10 Cross-section SEM image, displaying that an excessive deposition of MnO ₂ is leading to a non-conformal coating	55
5-11 XPS spectrum of the Mn 2p orbital of the electrochemical deposited MnO ₂ nanotube shell	56
5-12 Electrochemical performance of the o-SnO ₂ /MnO ₂ core/shell nanotube array	57
5-13 Performance of the o-SnO ₂ /MnO ₂ and c-SnO ₂ /MnO ₂ nanotube arrays. (a) Rate capability and structure comparison; (b) Literature comparison of various MnO ₂ based structures	57
5-14 Long-time cycling stability and charge efficiency of the o-SnO ₂ /MnO ₂ core/shell nanotube array	58
5-15 Electrochemical impedance spectroscopy of the SnO ₂ /MnO ₂ core/shell nanotube array	59
5-16 Structural investigation of the self-supported 3D SnO ₂ /PPy nanotube array	62
5-17 FTIR spectrum (a) and Raman spectrum (b) of the electrochemically polymerized PPy on a SnO ₂ nanotube array	63
5-18 Electrochemical performance of the SnO ₂ /PPy nanotube array	64
5-19 Electrochemical performance of the SnO ₂ /PPy nanotube array	65
5-20 Electrochemical impedance spectroscopy of the SnO ₂ /PPy core/shell nanotube array	66
5-21 Schematic diagram, illustrating the fabrication and assembling process of the asymmetric three-dimensionally nanostructured supercapacitor device	67
5-22 Investigation of the operating potential window for the 3D asymmetric PPy//MnO ₂ supercapacitor	68
5-23 Electrochemical performance of the 3D PPy//MnO ₂ supercapacitor	69
5-24 Electrochemical performance of the 3D PPy//MnO ₂ supercapacitor investigated in a two-electrode setup in a potential window of 1.7 V	71

List of Figures

5-25 Investigation of the leakage current and open circuit potential	72
5-26 Electrochemical impedance spectroscopy of the asymmetric PPy//MnO ₂ supercapacitor	73
5-27 Schematic diagram, illustrating the template-assisted fabrication process of self- supported TiN (route A) and C-TiN (route B) nanotube arrays	75
5-28 Structural investigation of the synthesized carbon.....	76
5-29 Structural analysis of the synthesized carbon and C-TiN	77
5-30 TEM investigation of a single C-TiN nanotube and crystal structure of the TiN.	78
5-31 (a) Overview and (b) high resolution SEM images of a TiN nanotube array fabricated via route A	79
5-32 Electrochemical investigation of the C-TiN and TiN nanotube arrays	80
5-33 Morphology investigation of the C-TiN and TiN electrode before and after long- time cycling	82
8 Appendix	
A1 Number of publications per year listed in <i>Web of Knowledge</i> ^[381] related to supercapacitors.....	116
A2 Material growth realized by ALD	117
A3 Areal and volumetric energy and power density of the asymmetric PPy//MnO ₂ supercapacitor	118
A4 The asymmetric PPy//MnO ₂ supercapacitor can light up a red LED.....	118
A5 Electrochemical performance of the bare TiN nanotube array	119
A6 Charge/discharge performance of the C-TiN nanotube array at 1 A g ⁻¹ in comparison to a bare C nanotube array without TiN deposition	119

List of Tables

8 Appendix

A1 Literature survey of reported MnO ₂ based core/shell and bare MnO ₂ supercapacitor materials	109
A2 Literature survey of aqueous symmetric and asymmetric supercapacitors.....	112
A3 Specific capacitance values of the o-SnO ₂ /MnO ₂ and c-SnO ₂ /MnO ₂ nanotube array. The data is plotted in Figure 5-13a.....	115
A4 Specific capacitance values of the SnO ₂ /PPy nanotube array. The data is plotted in Figure 5-19a.	115
A5 Device performance of the PPy//MnO ₂ asymmetric device. The data is plotted in Figure 5-24b.....	115
A6 Device performance of the MnO ₂ //MnO ₂ symmetric device. The data is plotted in Figure 5-24b.....	116
A7 Specific capacitance values of the C-TiN and TiN nanotube array. The data is plotted in Figure 5-32c.....	116

List of Abbreviations

AAO	Anodic aluminum oxide
AC	Activated carbon
ACN	Activated carbon nanofiber
Al	Aluminum
ALD	Atomic layer deposition
aMEGO	Activated microwave expanded graphite oxide
Aq	Aqueous
Au	Gold
BL	Barrier layer
c	Specific capacitance in Farad per gram
C	Capacitance in Farad
CB	Carbon black
CE	Counter electrode
CMG	Chemically modified graphene
CNF	Carbon nanofoam
CNT	Carbon nanotube
C-TiN	Carbon coated titanium nitride
CV	Cyclic voltammetry
CVD	Chemical vapor deposition
D_{int}	Interpore distance
D_p	Pore diameter
EDLC	Electric double-layer capacitance
EDX	Energy dispersive X-ray spectroscopy
EGO	Exfoliated graphene oxide
EIS	Electrochemical impedance spectroscopy
EKMU	Electrode kinetics and material utilization
F	Faraday constant
FE-SEM	Field emission scanning electron microscopy
fFWNT	Functionalized few-walled carbon nanotubes
FG	Functionalized graphene

List of Abbreviations

FTIR	Fourier transform infrared spectroscopy
GBM	Graphene based material
GHCS	Graphitic hollow carbon spheres
GO	Graphene oxide
GS	Graphene sheets
HA	Hard-anodization
M	Molar mass
m	Active electrode mass
MA	Mild-anodization
mEC	Micro electrochemical capacitor
MEGO	Microwave exfoliated graphene oxide
MEMS	Micro-electro-mechanical system
ML	Monolayer
Mn	Manganese
MnO ₂	Manganese dioxide
MWCNT	Multiwall carbon nanotube
NiMH	Nickel-metal hybrid battery
NT	Nanotube
OMC	Ordered mesoporous carbon
PANI	Polyaniline
PC	Porous carbon
PEDOT	Poly-3,4-ethylenedioxythiophen
PNM	Polymeric nano-micelle
PPy	Polypyrrole
PVD	Physical vapor deposition
Q	Capacity in Coulomb
R	Universal gas constant
R'	Relative fraction of reagents
R _{CT}	Charge-transfer resistance
RE	Reference electrode
RGM	Reduced graphene based material
RGO	Reduced graphene oxide
R _s	Equivalent series resistance
SAED	Selective area electron diffraction

List of Abbreviations

SEM	Scanning electron microscope
SHE	Standard hydrogen electrode
Si	Silicon
SnO ₂	Tin dioxide
STEM	Scanning transmission electron microscopy
t _{dis}	Discharge time
TEM	Transmission electron microscopy
TiN	Titanium nitride
U	Potential in Volt
V ₂ O ₅	Vanadium pentoxide
VN	Vanadium nitride
VO _x	Vanadium oxide
WE	Working electrode
XPS	X-ray photoelectron spectroscopy
z	Number of electrons
Z	Atomic number
Zn ₂ SnO ₄	Zinc stannate
ZnO	Zinc oxide

1 Introduction

The depletion of fossil fuels^[1] and the ongoing climate change^[2] require society to shift from fossil based energy carriers towards clean, efficient and renewable energy resources. As a result, solar radiation and wind are progressively utilized as renewable energy resources^[3] and electric mobility with low CO₂ emission is developing rapidly.^[4] The intermittent supply of solar radiation and wind, as well as the urge to have electric vehicles with a range compatible to an internal combustion engine, raises the demand of high performance energy storage devices. At the forefront of these are electrical energy storage systems, such as batteries and supercapacitors.^[5,6] However, the performance of current technology has to be improved substantially to meet the requirements of such disparate applications as large scale stationary units (e.g., energy storage in isolated grids, peak leveling of intermittent energy supply from solar cells and wind parks), mid-size storage (e.g., trams, electric vehicles, regenerative braking), and small portable units (e.g., smart phones, intelligent watches, eye-wear, MEMS, energy harvesting).^[7] In the last decade, supercapacitors have attracted much attention as electrochemical energy storage devices to replace batteries or as a complementary unit because they exhibit larger specific power than batteries and can withstand strikingly more charge/discharge cycles.^[6] Thereby, supercapacitors typically rely on earth abundant materials and have limited environmental impact. The high potential of supercapacitors has been stressed by Tesla's CEO Elon Musk. He guesses that it could be capacitors – rather than batteries – that deliver an important breakthrough for electric transportation. "If I were to make a prediction, I'd think there's a good chance that it is not batteries. But capacitors."^[8]

The performance of electrochemical energy storage systems and in particular supercapacitors depends intimately on the properties of their active materials^[9] and is evaluated in terms of three parameter: power capability, cycle life, and specific energy.^[10] Whereas supercapacitors exhibit strong power capability and long cycle life, they cannot compete with batteries in terms of specific energy. Therefore, it is the main objective of today's research to improve the specific energy of the next generation of supercapacitors without sacrificing power and cycle life. The specific energy (E) is defined as:

$$E = \frac{1}{2} c (\Delta V)^2 \quad \text{eq. 1-1}$$

Introduction

with c being the specific capacitance (F g^{-1}) and ΔV the operating potential window (V).

The key to enhance the performance of supercapacitors is based on:

- (i) New active materials that exhibit pseudocapacitive charge storage and thus provide higher specific capacitance values compared to materials that store charge in an electric double-layer (e.g., high-surface-area carbon). The term “pseudocapacitance” describes fast and reversible Faradaic redox reactions which result in charge/discharge profiles comparable to electric double-layer capacitors.^[5,11] Promising materials that show pseudocapacitance include metal oxides (RuO_2 , MnO_2),^[12,13] conductive polymers (PANI, PPy),^[14,15] and metal nitrates (VN, TiN).^[16,17]
- (ii) Fast electrode kinetics and efficient material utilization (EKMU; *i.e.*, rapid electron transport, short ion diffusion length and porous structure, large surface area) because an enhanced EKMU can directly increase the power capability, improve the system’s reversibility and thus the cycle life, and improve specific energy.^[10]
- (iii) High operating potential windows by intelligent cell design. This aim could be achieved in aqueous supercapacitors by utilizing an asymmetric device configuration^[18] with different active materials at the negative and positive electrode and by ionic liquids^[19,20] in non-aqueous systems.

In order to fulfill these requirements, supercapacitor materials need to exhibit distinct and often divergent functions, as electron and ion conductivity, charge storage, and provide the physical structure of the electrode itself.^[21] Unfortunately, very few individual materials exhibit all of these properties. Thus, there is great promise in developing new composite materials and architectures in which selected components are assembled into multifunctional structures using recent advances in nanoscience.^[21] The need to develop new active material systems and design tailored nanostructures has also been outlined by Gogotsi, who says that “Nanoscale design of the structure and chemistry of electrode materials may enable us to develop a new generation of devices that approach the theoretical limit for electrochemical storage and deliver electrical energy rapidly and efficiently.”^[22]

Nanotechnology offers multiple routes to fabricate active high-surface-area materials for supercapacitors, such as nanotubes,^[23] nanowires^[24] and nanosheets.^[25] During the electrode fabrication in a common supercapacitor the nanometer sized active material is typically mixed with additives like conductive carbon and resistive binders to form a stable thin film on a current collector. Unfortunately, by this approach the active material

Introduction

is randomly distributed in the electrode without control of the EKMU and the high-surface-area might partially be lost by the accumulation of nanostructures in dense electrodes. Here, three-dimensional nanostructures offer a unique possibility to design novel supercapacitor electrodes with respect to an optimized EKMU and to achieve large specific capacitance values (c). In this work, the term “three-dimensional nanostructure” refers to systems that are self-supported (*i.e.*, free-standing) and thus circumvent the use of additives, exhibit a porous high surface area framework where individual components are spatially distributed on the nanoscale^[21] as to facilitate a rapid transport of ions to the electroactive interfaces,^[21] and are composed of low dimensional interconnected nanostructures which are arranged in a volumetric manner (*e.g.*, 1D nanotube array) or are monolithic. Three-dimensional nanostructures can be built up from diverse materials to nano-engineer multiple functions into the supercapacitor electrode, such as a highly conductive core to enhance the electron transport and a pseudocapacitive thin shell to improve the material utilization and thus the energy storage. Thereby, it is widely accepted among scientists that three-dimensional nanostructures can strongly enhance the performance of energy devices.^[26-30] However, up to now nanotechnology is lacking a versatile approach that is capable of growing dense three-dimensional nanostructures in a highly ordered manner as to guarantee a structural control in the nanometer range. Moreover, from a device point of view, it is highly desirable to enlarge the operating potential window (ΔV) of supercapacitors because a twofold increase results in a four times improvement in specific energy. Recently, asymmetric supercapacitors that consist of different electrode materials at the negative and positive electrode have received much attention.^[18] Such configurations circumvent the main limitation of aqueous supercapacitors and extend the operating potential window beyond the thermodynamic limit of 1.23 V to operating voltages as high as 2 V.^[15,18] Thereby, aqueous supercapacitors offer an energy storage solution that is economically viable, safe to operate, and has limited environmental impact.^[18] In particular asymmetric systems with a carbon based negative and a MnO_2 based positive electrode were studied intensively.^[31-35] MnO_2 is one of the most promising pseudocapacitive materials for the positive electrode because of the large theoretical capacitance, high natural abundance, environmental benign nature, and low cost for raw material.^[36] Unfortunately, the choice of promising materials that exhibit a complementary potential window to MnO_2 is limited. Known materials other than carbon materials (*e.g.*, Fe_2O_3 , PEDOT) are only insufficiently investigated as negative electrode materials in MnO_2 based asymmetric supercapacitors.

Introduction

Thereby, materials with higher specific capacitance values compared to carbon materials could offer great potential to further increase the specific energy of supercapacitors.

Hence, it is proposed that the development of an asymmetric supercapacitor device that entirely consists of three-dimensional pseudocapacitive nanostructures should have the potential to boost the performance of supercapacitors.

In this thesis, an innovative approach is developed to synthesize three-dimensional nanotube arrays for aqueous supercapacitors. Nano-porous anodic aluminum oxide (AAO) serves as a template to fabricate vertically aligned self-supported nanotubes with high structural controllability by atomic layer deposition (ALD) and electrochemical deposition. Three-dimensional nanotube arrays of different pseudocapacitive materials (*i.e.*, manganese dioxide, polypyrrole, titanium nitride) are fabricated with the aim to improve the charge storage capability of aqueous supercapacitors by simultaneously increasing the specific capacitance of the active materials and enlarging the voltage window of a device. First, a self-supported SnO₂/MnO₂ core/shell nanotube array is designed to enhance the EKMU and thus circumvent limitations that arise from the large internal electric resistance of MnO₂. The SnO₂ nanotube core provides a conductive matrix and is coated by a thin electrochemically active MnO₂ shell. The material performance is drastically increased by the three-dimensional core/shell structure and large specific capacitance values (*e.g.*, 910 F g⁻¹ at 1 A g⁻¹) with an excellent rate capability (remaining 217 F g⁻¹ at 50 A g⁻¹) being achieved. This material outnumbers the performance of nanostructured electrodes that purely consist of MnO₂ (*e.g.*, a self-supported MnO₂ nanotube array only exhibits 210 F g⁻¹ at 1.9 A g⁻¹)^[36] and importantly, it is among the highest reported values of MnO₂ based core/shell nanostructures. Hence, the nanoscale design of the electrode structure led to an improved energy storage capability. Second, a polypyrrole (PPy) based core/shell nanotube array is fabricated by a similar approach as the SnO₂/MnO₂ core/shell nanotube array. The active electrode material is designed with the aim to exhibit pseudocapacitive charge storage in a complementary voltage window to MnO₂. Importantly, it could be shown that the active PPy material exhibits a larger specific capacitance compared to carbon materials in neutral electrolytes and thus offers great potential to further improve the energy storage capability of asymmetric MnO₂ based devices. Third, the implementation of the PPy and MnO₂ based electrodes into an asymmetric supercapacitor led to an aqueous device that can operate within a large potential window of 1.7 V. The development of the functional self-supported core/shell nanotube arrays in combination with the asymmetric electrode design efficiently enhances the specific energy of the aqueous supercapacitor

Introduction

(e.g., 27.2 Wh kg⁻¹) while maintaining high specific power (e.g., 24.8 kW kg⁻¹). Fourth, self-supported C-TiN nanotube arrays are fabricated. The synthesis is realized by ALD of TiN and an innovative conformal carbon coating technique, which is based on a self-assembly approach of polymeric nano-micelles on a nano-porous AAO template. Here, the functional carbon coating is synthesized first and then the active electrode material is deposited inside. This attempt results in a highly conformal coating on the three-dimensional nanotube array and a good control of the structural parameters. The prepared self-supported C-TiN nanotube array is tested as a negative electrode material for aqueous based supercapacitors. Importantly, the functional conformal carbon coating efficiently improved the long-time cycling stability of TiN and hence, addresses one of the main challenges of metal nitride supercapacitors.^[37]

This thesis is structured as follows. In the Chapter 2, the electrochemical energy storage in supercapacitors is discussed and the underlying charge storage mechanisms are presented (*i.e.*, electric double-layer capacitance and pseudocapacitance). Thereafter, different material systems for supercapacitor applications are introduced and compared with respect to their charge storage capability. A detailed literature analysis is presented. The Chapter 3 discusses strategies to synthesize three-dimensional nanostructures and outlines the advantages that arise for supercapacitors. This chapter highlights the nanostructuring techniques used within this work, such as atomic layer depositing, nano-porous AAO, and electrochemical deposition. The underlying concepts and working principles are discussed with respect to the utilized material systems. The Chapter 4 presents a detailed overview of the experimental conditions and methods that are employed to synthesize and characterize the three-dimensional nanotube arrays. The morphology and the chemical composition are investigated by SEM, TEM, EDX mapping and line scan, XPS, XRD, Raman spectroscopy, and FTIR spectroscopy. The electrochemical performance of the synthesized structures is studied by cyclic voltammetry, charge/discharge, and electrochemical impedance spectroscopy. Three-electrode and two-electrode systems are evaluated. The results are present and discussed in the Chapter 5 which is structured into four main sections. Here, the fabrication route of the SnO₂/MnO₂ and SnO₂/PPy core/shell nanotube arrays is presented and the morphology of the three-dimensional nanostructures is analyzed. The MnO₂ and PPy based structures are further individually characterized as complementary electrodes for aqueous supercapacitors. In addition, an asymmetric PPy//MnO₂ supercapacitor device that can operate within a large voltage window is assembled and characterized with respect to its electrochemical performance. Further, carbon coated

Introduction

TiN nanotube arrays are synthesized to improve the cycling stability of metal nitrides for supercapacitor applications. The Chapter 6 summarizes the results and gives an outlook to this work.

2 Electrochemical energy storage in supercapacitors

Supercapacitors (*i.e.*, electrochemical capacitors, ultracapacitors) represent a fast expanding class of today's energy storage devices. The comparison of the performance characteristics of supercapacitors to conventional solid-state capacitors, which supply high specific power and batteries (*e.g.*, NiMH, lead acid, and Li-ion batteries), which possess high specific energy reveals that supercapacitors build a bridge between both technologies and combine the respective advantages into one single device, as shown in the specific energy versus specific power plot (*i.e.*, Ragone plot) in Figure 2-1.^[5,6] The specific energy (E) and specific power (P) are defined as follows:

$$E = \frac{1}{2} c (\Delta V)^2 \quad \text{eq. 2-1}$$

$$P = \frac{E}{t_{dis}} \quad \text{eq. 2-2}$$

with c being the specific capacitance (F g^{-1}), ΔV the operating potential window (V), and t_{dis} the discharge time (s). Supercapacitors are distinguished from their solid-state counterparts by storing charge at electrochemical interfaces, unlike the formation of an electric field excited across a dielectric as in ordinary solid-state capacitors, which results in specific capacitance values that are orders of magnitudes larger.^[18] The enhanced specific energy of supercapacitors is associated with compromise in specific power,

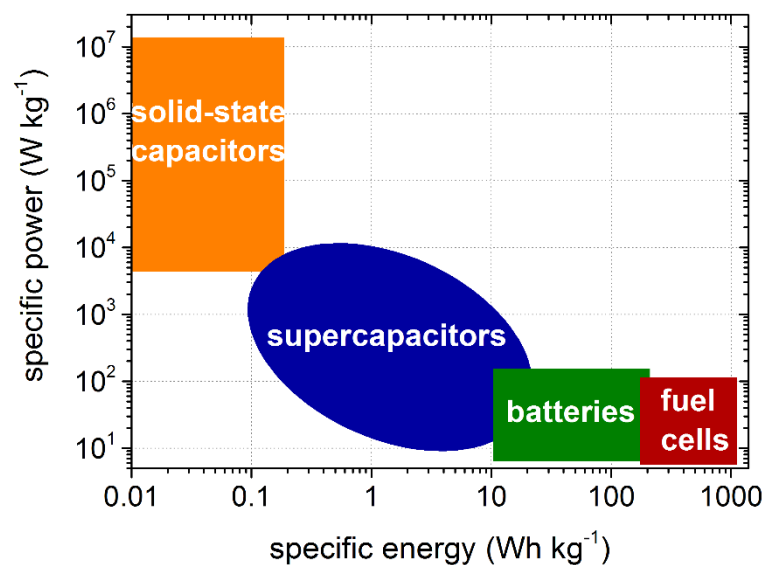


Figure 2-1 | Specific power vs. specific energy, also called Ragone plot, of different energy-storage devices, including solid-state capacitors, supercapacitors, batteries, and fuel cells. (Figure redrawn from Ref.^[18])

Electrochemical energy storage in supercapacitors

resulting from essential ion transport during charging and discharging. In terms of design and functionality supercapacitors are closely related to batteries. Both devices are based on an electrochemical cell that consist of two opposing electrodes which are electrically isolated by a non-conductive separator and contain a liquid or solid-state electrolyte accommodating mobile ions. Supercapacitors are designed to operate at high power density, whereas batteries are typically constructed to deliver a maximum of energy. Thereby, supercapacitors store charge by electrochemical mechanisms occurring near or at the surface of the electrodes (*e.g.*, double-layer capacitance or pseudocapitance), whereas batteries are designed to store energy in the bulk of the electrodes by Faradaic reactions.^[18] Hence, supercapacitors exhibit larger specific power compared to batteries ($1-10 \text{ kW kg}^{-1}$ vs. $< 0.1 \text{ kW kg}^{-1}$ for Li-ion batteries) and show charging and discharging behavior that occurs on the order of seconds and minutes with trade-off in specific energy ($\sim 6 \text{ Wh kg}^{-1}$ vs. $> 100 \text{ Wh kg}^{-1}$ for Li-ion batteries).^[38]

Recently, supercapacitors have attracted a large amount of attention as an energy-storage solution in various applications. In particular, supercapacitors are well-suited to store and release energy in repetitive motion (*e.g.*, regenerative braking,^[39] lift/release of cargo cranes^[40]). This is due to the fast symmetric charge/discharge characteristic and long cycle life which results in an improved energy efficiency and reduced exhaust emission.^[41] Further, supercapacitors can contribute to energy-dense, but power-limited devices (*e.g.*, batteries, fuel cells, combustion engines) by forming a hybrid system. The advantages of such systems have already been shown in applications like cold cranking^[42] and start-stop systems^[43] in trucks and cars. Thereby, supercapacitors increase the systems lifetime, reduce both total system weight and volume, and enhance the systems efficiency by covering peak power demands.^[41,44] Furthermore, the ongoing miniaturization of electric circuits, sensors and wireless sensor networks, and the developing field of energy harvesting create a high demand for energy storage systems that can be integrated completely into the device they power. Especially the development of micro electrochemical energy storage devices, such as micro-batteries^[4] and micro electrochemical capacitors (mECs),^[5,6] has drawn much attention. However, micro-batteries suffer from limited cycle life, which is a major problem in applications where maintenance and replacement are difficult. Further, micro-batteries are not suitable for applications with high power demand, such as wireless data transmission. Therefore, a crucial role is addressed to mECs in order to address the emerging challenges associated with the development of new autonomous systems.^[7, 8]

2.1 How to distinguish supercapacitor from battery type energy storage?

Intrinsic properties of supercapacitor materials

The research field of electrochemical energy storage has expanded dramatically during the last decade and a large variety of active materials have been reported, both for supercapacitor and battery type energy storage. Thereby both technologies rely on electrochemical processes to store energy, but the underlying mechanisms are fundamentally different. In battery materials, conversion from one state to another occurs at a constant potential until a phase transformation is completed. Whereas charge storage in supercapacitors typically includes ion adsorption in electric double-layer capacitors (Figure 2-2a,b; Section 2.2) or fast redox reactions at the surface of active materials (Figure 2-2c,d; Section 2.3).^[5] Thereby the high power density originates from

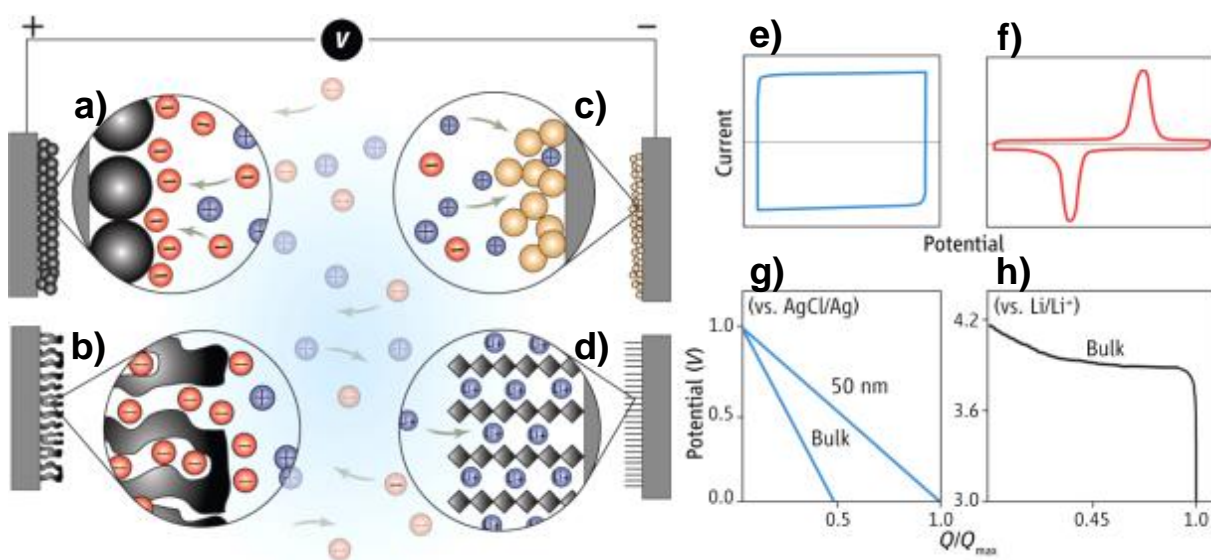


Figure 2-2 | The different mechanisms of capacitive energy storage (a to d). Double-layer capacitance develops at electrodes that are composed of (a) carbon particles or (b) porous carbon. The double layer shown here arises from adsorption of negative ions from the electrolyte on the positively charged electrode. Pseudocapacitive mechanisms include (c) redox pseudocapacitance, as occurring in MnO₂, and (d) intercalation pseudocapacitance. (e to h) Electrochemical characteristics that differentiate supercapacitor and battery materials. Cyclic voltammograms distinguish a supercapacitor material where the response to a linear change in potential is a constant current (e), as compared to a battery material, which exhibits Faradaic redox peaks (f). Galvanostatic discharge behavior (where Q is charge) for a pseudocapacitor (e.g., MnO₂) is linear for both bulk and nanoscale material (g),^[46,47] in comparison a LiCoO₂ bulk material shows a voltage plateau (h).^[48] (Figure taken from Ref.^[45])

the available surface charge and the absence of bulk phase transformation leads to high reversibility and long life (up to 1,000,000 cycles).^[22] However, the blurring of these two electrochemical approaches can cause confusion and may lead to unwarranted claims unless careful attention is paid to fundamental performance characteristics, as emphasized by Patrice et al.^[45] Electrochemical energy storage in supercapacitors can be distinguished from battery materials by potentiostatic and galvanostatic methods, as shown in Figure 2-2e-h. Supercapacitor materials exhibit rectangular cyclic voltammograms where the response to a linear change in potential is a constant current (Figure 2-2e) and show a linear time-dependent change in potential at a constant current (Figure 2-2g).^[22,45] In contrast, battery materials exhibit distinct redox peaks in cyclic voltammograms with a large voltage hysteresis between charging and discharging steps (typically greater than 0.1 to 0.2 V) (Figure 2-2f) and show a broad voltage plateau in galvanostatic experiments (Figure 2-2h).^[45] Hence, materials that experience phase transformations (e.g., NiOOH to Ni(OH)₂) and show sluggish kinetics with highly nonlinear charge/discharge performance and redox peaks in cyclic voltammograms should not be called supercapacitors,^[22] and will not be defined as such in this work. In order to maintain clarity in the terminology used in combination with appropriate measurements and analyses, the term “supercapacitor” will only be applied to material systems that fulfill the following criteria:

1. show rectangular cyclic voltammograms (Figure 2-2e)
2. show linear time-dependent change in potential at a constant current (Figure 2-2g)
3. exhibit high Coulombic efficiency and fast charge/discharge kinetics

2.2 Electric double-layer capacitance

The underlying principles of charge storage in electric double-layer capacitors were developed by Helmholtz in the nineteenth century. However, it took until 1957 that the use of electric double-layer capacitance (EDLC) for storing electrical charge was demonstrated and patented first by Becker and later commercialized by the Sohio group.^[49,50] Today electric double-layer capacitors are available from many international suppliers^[51,52] in the range of single-cells (e.g., 2.7 V) to large scale arrays (e.g., 125 V). Electrochemical double-layer capacitors consist of two high surface area carbon electrodes usually separated by a non-aqueous electrolyte. The energy is stored during charging in the formation of an electric double-layer at the electrode/electrolyte interface

in a non-Faradaic manner. Thereby, positively charged electrolyte ions reversibly assemble at the negative active electrode material and negatively charge electrolyte ions assemble at the positive active electrode material, leading to the formation of an electrostatic energy field between the electrolyte ions and the respective electrode. The electrical energy stored in this field arises from the formation of the EDLC, which can basically be described by the following equation developed by Helmholtz:

$$C = \frac{\epsilon_r \epsilon_0 A}{d} \quad \text{eq. 2-3}$$

with ϵ_r being the electrolyte dielectric constant, ϵ_0 the dielectric constant in vacuum, A the electrode surface area, and d the double-layer thickness (*i.e.*, charge separation distance is in the order of angstrom^[53]). Therefore, high specific capacitance values can be achieved by maximizing the electrodes surface area. In particular, nanostructured carbon materials,^[54,55] including aerogels,^[56] nanotubes,^[57] porous carbons,^[58] and graphene^[59,60] have been utilized successfully. The achieved capacitance densities are situated in the range of 15 to 50 $\mu\text{F cm}^{-2}$.^[61] Besides the increase of specific capacitance a further enhancement in specific energy can be achieved by maximizing the cell potential of the supercapacitor according to eq. 2-1. Thereby, the main challenge is to circumvent the limitations set by electrolyte decomposition at too high cell-potentials (*e.g.*, potentials above ~ 1.23 V for aqueous based electrolytes and ~ 2.7 V for acetonitrile-based electrolytes). Here, the primary attempt for electric double-layer capacitors is based on the development of advanced electrolytes (*e.g.*, ionic-liquids^[19,20]) with potential windows of ~ 3.5 to 4.5 V. However, the ultimate specific energy of electric double-layer capacitors is fundamentally limited by their reliance on EDLC as the primary energy storage mechanism because the device capacity Q (C) is directly proportional to the devices capacitance C (F) (*i.e.*, is proportional to A) according to:^[18]

$$Q = C U \quad \text{eq. 2-4}$$

This limitation of supercapacitors based on ELDC can be circumvented by introducing new active electrode materials that store energy by rapid and reversible redox reactions involving electron-exchange at or near the electrodes surface (*i.e.*, pseudocapacitors).

2.3 Pseudocapacitance

In comparison to electric double-layer capacitors, higher specific capacitance values can be achieved by utilizing redox active materials, including transition metal oxide, conductive polymers, and metal nitrides (see Section 2.4), as first discovered on RuO_2 in an acidic electrolyte by Trasatti et al. in 1973.^[62] These materials store charges, unlike

Electrochemical energy storage in supercapacitors

electric double-layer capacitors, in a Faradaic manner based on fast and reversible redox reactions that occur at or near the surface of the electrode.^[5] The term “pseudocapacitance” is commonly used to describe the charge storage mechanism of these materials because the appearance of broad and symmetric charge/discharge profiles replicates those generated by EDLC. The origin of pseudocapacitance can be derived mathematically by considering a general redox reaction involving z electrons of the following type:^[5,61]



The redox potential E at equilibrium for such redox reactions can be described by the Nernst equation:

$$E = E^0 + \frac{RT}{zF} \ln \frac{[Ox]}{[Red]} \quad \text{eq. 2-6}$$

where E^0 is the standard potential of the redox couple, R is the universal gas constant, F is the Faraday constant, and $[...]$ represents the concentration of the indicated species.

Rearranging and expressing eq. 2-6 in relative fractions $R' = \frac{[Ox]}{[Ox]+[Red]}$ of reagents leads to:

$$\frac{R'}{1 - R'} = e^{\frac{(E-E^0)zF}{RT}} = e^{\frac{\Delta EzF}{RT}} \quad \text{eq. 2-7}$$

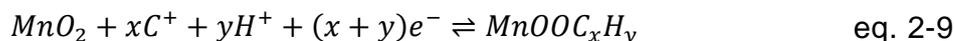
The differentiation of this equation with respect to ΔE yields a formal capacitance C :^[5]

$$\frac{C}{Q} = \frac{dR'}{dE} = \frac{zF e^{\frac{\Delta EzF}{RT}}}{RT(1 + e^{\frac{\Delta EzF}{RT}})^2} \quad \text{eq. 2-8}$$

with Q being the charge associated with the total oxidizable or reducible material. The capacitance derived in eq. 2-8 arises from Faradaic reactions and is not an electrostatic capacitance. It should be noticed that a single redox reaction of this kind can only exceed a potential range of approximately ± 100 mV and thus is not very attractive for charge storage in supercapacitor applications.^[5] However, in certain materials a series of such redox reactions can occur, which is leading to an expansion of the possible operating voltage window (e.g., 1.2 V for RuO_2 and 0.9 V for MnO_2).^[61] The overlap of different redox potentials in such materials give rise to an almost constant net redox capacitance, as illustrated in Figure 2-3a, making pseudocapacitive materials possible candidates for supercapacitor applications. Besides other metal oxide materials (e.g., RuO_2), manganese dioxide (MnO_2) is one of the most promising pseudocapacitive materials. The charge storage mechanism of MnO_2 in mild aqueous electrolytes is based on

Electrochemical energy storage in supercapacitors

surface adsorption of electrolyte cations C^+ (e.g., Na^+ , K^+), as well as proton incorporation, according to the following reaction:[6,63]



Thereby fast, reversible and successive surface redox reactions within a potential window of 0.9 V define the behavior of the cyclic voltammogram, as shown Figure 2-3b. The produced shape is closely related to the ideal rectangular shape observed for EDLC. In terms of specific capacitance MnO_2 based supercapacitors show a clear advantage compared to electric double-layer capacitors, see Figure 2-4. However, the operating potential window of MnO_2 is limited by the upper cut-off voltage at 0.9 V vs. Ag/AgCl because of oxygen evolution which results in a non-reversible redox process and at negative potentials by irreversible reduction and disproportionation of Mn^{4+} to soluble Mn^{2+} , which leads to a loss of active electrode material at each charge/discharge cycle.[18,64-66] These restrictions define the operating potential window of MnO_2 to 0.9 V, which is narrow compared to state of the art electric double-layer capacitors. While considering that the energy stored in supercapacitors is proportional to the square of the operating potential window (see eq. 2-1), it becomes obvious that the enhancement in

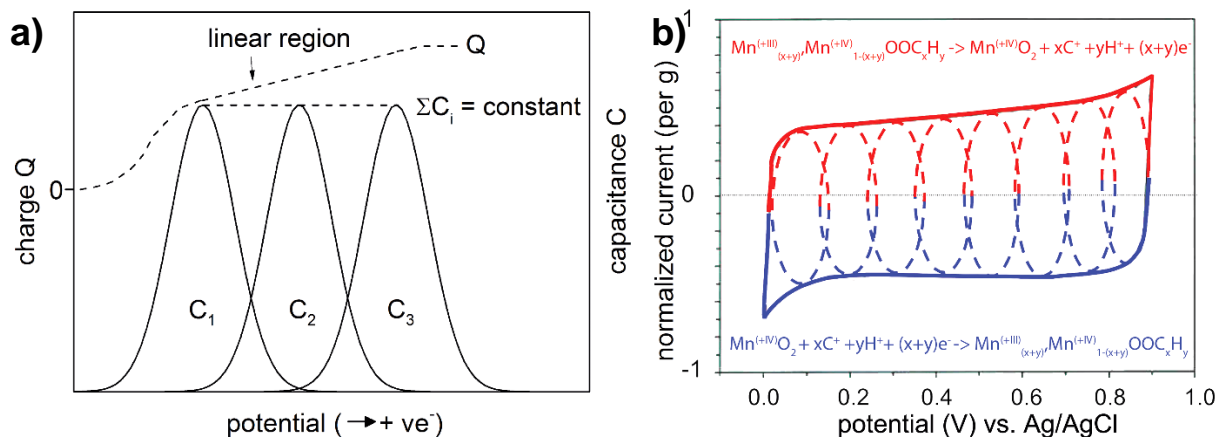


Figure 2-3 | Redox reactions leading to pseudocapacitance. (a) Illustration of the constant net capacitance, arising from three individual redox capacitances C_i over an appreciable potential range and accumulated charge Q . (Figure redrawn from Conway [5], chapter 11); (b) Schematic cyclic voltammogram of a MnO_2 electrode in an aqueous electrolyte, showing successive multiple surface redox reactions that lead to pseudocapacitive charge storage. The red (upper) part is related to the oxidation from Mn^{3+} to Mn^{4+} and the blue (lower) part refers to the reduction from Mn^{4+} to Mn^{3+} . (Figure taken from Ref.[6])

Electrochemical energy storage in supercapacitors

specific capacitance is negated to some extent by the restriction in the operating potential window. Consequently, MnO_2 has limited potential in symmetric $\text{MnO}_2//\text{MnO}_2$ (notated as: negative electrode//positive electrode) supercapacitors. However, the potential of MnO_2 as a positive electrode combined with different negative electrode materials (e.g., carbon based materials, conducting polymers, metal nitrides), that possess capacitive behavior in a complementary potential window to MnO_2 , in an asymmetric aqueous based supercapacitor devices is highly promising (see Section 2.5).

2.4 Supercapacitor materials

Scientists have investigated a large variety of electrode materials for the use in supercapacitor devices. In order to compare the performance achieved among these different materials a summary of the specific capacitance values reported in literature for aqueous supercapacitors is shown in Figure 2-4. The diagram presents an overview of the obtained specific capacitance values among different material systems. It includes electric double-layer materials, such as activated carbon (AC), carbon nanotubes (CNT),

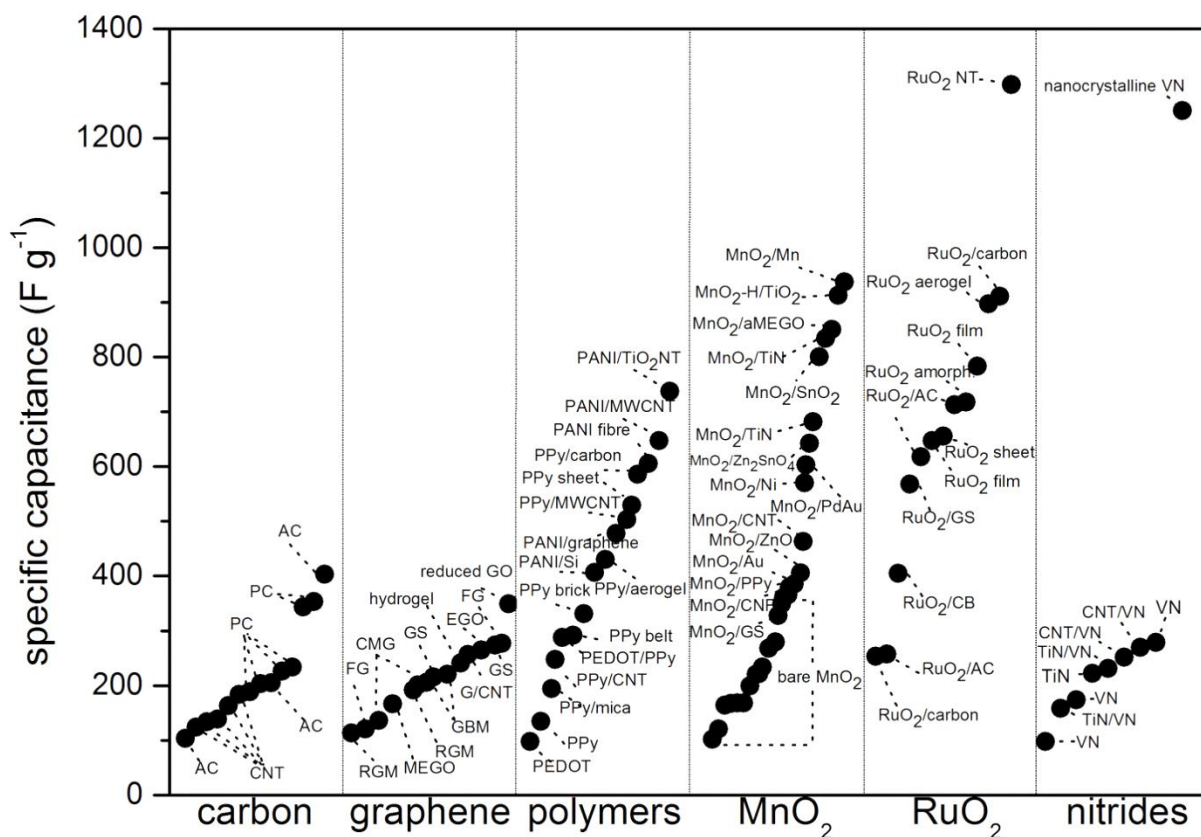


Figure 2-4 | Reported specific capacitance values in literature for the most relevant supercapacitor materials including carbon,^[23,58,67-76] graphene,^[59,77-89] polymers,^[90-103] MnO_2 ,^[24,104-131] RuO_2 ,^[12,132-144] and nitrides.^[16,145-153]

porous carbon (PC), and graphene and pseudocapacitive materials, including polymers (e.g., PEDOT, PPy, PANI), metal oxides (e.g., MnO₂, RuO₂, V₂O₅), and metal nitrides (e.g., TiN, VN). More detailed information about the different material systems are supplied in the following sections and in Table A1 in the appendix.

2.4.1 Carbon

Carbon based supercapacitors are almost exclusively used in commercially available supercapacitors. In particular, porous carbons (PCs)^[58,75,76] and activated carbons (ACs)^[67,68,73,74] are used in today's supercapacitor devices and achieve specific capacitance values between 100 to 400 F g⁻¹. The superior specific capacitance values of PCs and ACs over other carbon structures can be ascribed to the extremely large surface area of these structures, which arises from the complex porous structure of macropores (> 500 Å), mesopores (20 to 500 Å), and micropores (< 20 Å). However, empirical evidence suggests that the porous structure cannot be utilized completely for charge storage.^[54,154,155] It is believed that this effect is caused by too large electrolyte ions, which can not diffuse into small micropores.^[156,157] Therefore, a key challenge to increase the performance of PCs and ACs is the determination of an optimal pore size for a given ion size and the establishing of feasible fabrication routes that can control the pore size distributions.^[74,158,159] Further, CNTs are heavily investigated as a supercapacitor material. The highest reported values of specific capacitance are in the range of 120 to 180 F g⁻¹.^[23,69-71] Even though the overall surface area of CNTs is smaller compared to ACs and PCs are CNTs an attractive candidate for supercapacitor devices. The well-established fabrication processes and the unique properties of CNTs, such as high conductivity and the opened microporous structure, make it a promising material for supercapacitor applications. The mesoporous structure in CNTs is, unlike the microporous structure of ACs and PCs, highly accessible for the electrolyte ions.

2.4.2 Graphene

Graphene is a promising material in a large variety of different applications^[160,161] and has received a tremendous amount of interest since the Nobel Prize of A. Geim in 2010.^[162] In particular, graphene has great potential to enhance the performance of supercapacitor devices. Its unique intrinsic properties, such as large surface area (2630 m² g⁻¹ theoretically), high mechanical strength, and high electric conductivity make it an ideal capacitor electrode material.^[163,164] In literature, several different strategies can be identified to prepare graphene-based electric double-layer capacitors. Graphene-

Electrochemical energy storage in supercapacitors

based electrode materials are mainly prepared by thermal,^[83,89] chemical,^[84,165] electrochemical,^[166] and microwave assisted reduction^[88] of graphene oxide (GO), graphene-based hydrogels,^[85] activation graphene,^[77,81,87] and intercalated graphene-based-sheets.^[77] Recently, graphene showed a strong electrochemical performance among carbon based materials with a high specific capacitance ranging from 100 to 348 F g⁻¹ and has outperformed CNTs as a material for supercapacitor devices. However, significant challenges need to be overcome to turn graphene into an efficient material for applications. In particular, it is difficult to prepare large scale high quality graphene-based materials in a cost-effective way. And further, graphene materials are easy to re-stack, which results in a decrease of its physical properties and make it difficult to process.^[163] Some strategies to overcome this problem have been reported, such as a functionalization of graphene^[161] and the utilization of spacers, as reported by Si et al. by separating graphene with platinum nanoparticles.^[167] However, graphene based electrodes still suffer from a low volumetric energy density.^[168]

2.4.3 Electrically conductive polymers

The most widely investigated polymer materials for energy storage in supercapacitor applications are PEDOT, PPy, and PANI. The reported values of specific capacitance range from ~100 to 740 F g⁻¹ and depend significantly on the polymer used and the fabrication method. For example, pure PEDOT^[94] and PPy^[97] show relatively low specific capacitance values of 100 F g⁻¹ and 137 F g⁻¹, respectively. Whereas a large improvement of the specific capacitance is achieved by coating polymers on a second material that acts as a scaffold and is electronically conductive, as shown in Figure 2-4. Specific capacitance values reported for such composite materials are much higher compared to their bare counterparts. Among all reported polymers PANI is the most promising with specific capacitance values of 740 F g⁻¹ and 650 F g⁻¹ reported for PANI coated TiO₂ nanotubes^[96] and PANI coated MWCNTs,^[91] respectively. Unfortunately, polymer materials suffer from swelling and contracting during the charging and discharging process, which results in capacitance fading and poor cycle life compared to carbon and metal oxide based capacitors.^[6,169,170] Interestingly, Heeger et al. have recently reported a highly stable polymer-supercapacitor with unmatched cycling stability (> 50000) by combining electrochemically active polymers (*i.e.*, PANI) and redox-active electrolytes (*i.e.*, benzoquinone-hydroquinone redox couple) with tailored electrochemical properties.^[14]

2.4.4 Metal oxides

Metal oxides, such as RuO₂, MnO₂, and V₂O₅ possess a high pseudocapacitance because of highly reversible surface redox reactions and hence, are an attractive material class for supercapacitor applications. Among all metal oxides RuO₂ has been studied most intensively in the last two decades. The unique characteristics, such as high intrinsic electrical conductivity ($3 \times 10^2 \Omega^{-1} \text{ cm}^{-1}$), high chemical and thermal resistance, and large theoretical capacitance make RuO₂ an ideal supercapacitor material.^[171] In 1995, Zheng et al. reported that amorphous hydrous RuO₂ prepared by a sol gel process exhibits a specific capacitance of 720 F g⁻¹.^[140,171] However, the prepared electrode material suffered from a poor rate capability. In order to increase the rate performance, scientists have fabricated composite materials of RuO₂ and carbon, such as carbon black,^[143] activated carbon,^[138] carbon nanotube,^[172] and graphene.^[136,171] Further, Hu et al. reported that three-dimensional arrays of polycrystalline hydrous RuO₂ nanotubes exhibit a superior rate capability and show an ultra-high specific capacitance of 1300 F g⁻¹.^[12] The rapid charge/discharge characteristic and the high specific capacitance are attributed to a short ion diffusion length, a good penetration of the electrolyte into the whole metal oxide matrix, and a good utilization of the active material.^[12] Even though RuO₂ is a material that shows excellent electrochemical performance, the high cost for the raw material restricts the use in commercial applications. For this reason, other metal oxides have been investigated. In 1999, Goodenough et al. first reported the use of MnO₂ powders as an active supercapacitor material.^[173] Since then, the interest in MnO₂ has grown rapidly. Its unique features, such as high theoretical capacitance (1233 F g^{-1}),¹ high natural abundance, environmental benign nature, and low cost for raw material have made it into one of the most promising candidates to improve the electrochemical performance of supercapacitor devices.^[64] Until about 2010, various scientists made the attempt to fabricate supercapacitor electrodes of pure MnO₂. The influence of the crystalline structure and the effect of the morphology on the charge storage capability of MnO₂ were investigated. It was found that the specific capacitance of MnO₂ depends on the crystalline structure and decreases in the following order $\alpha \approx \delta > \gamma > \lambda > \beta$.^[174,175] Further, many different morphologies of MnO₂ were reported, such as flowers (168 F g^{-1}),^[104] hollow spheres (167 F g^{-1}),^[105] clews (120 F g^{-1}),^[106] (2x4) tunnel nanorods (140 F g^{-1}),^[107] nanobelt bundles (268 F g^{-1}),^[108]

¹ Theoretical capacitance of MnO₂: $c_{\text{MnO}_2, \text{theory}} = \frac{F}{\Delta V M} = 1233 \text{ F g}^{-1}$ with F, ΔV and M being the Faraday constant, potential window (0.9 V) and molar mass (86.94 g mol⁻¹)

Electrochemical energy storage in supercapacitors

star-shape (360 F g^{-1}),^[125] coral-like (221 F g^{-1}),^[127] ultra-thin nanosheets (267 F g^{-1}),^[176] nanotubes (220 F g^{-1}),^[112] nanoneedles (233 F g^{-1}),^[109] nanowires (167.5 F g^{-1}),^[110] ultra-fine nanowire networks (279 F g^{-1}),^[24] and nanowire arrays on Ti/Si substrate (254 F g^{-1}),^[111] for more details see Table A1 in the appendix. However, all reported values of pure MnO_2 , despite the crystalline structure and morphology, utilize only a small fraction of the theoretical capacitance and show poor rate capabilities. These results are a consequence of the low internal electrical conductivity of MnO_2 (10^{-2} to $10^{-6} \Omega^{-1} \text{ cm}^{-1}$).^[64,120,177,178] In order to overcome this drawback a promising strategy is based on the realization of core/shell materials, whereas a highly conductive material acts as the core material and provides a scaffold for the MnO_2 shell. Figure 2-4 and Figure 2-5 clearly show that core/shell materials based on MnO_2 exhibit higher specific capacitance values and better rate capabilities compared to their bare MnO_2 counterparts. For instance tubular core/shell structures with high specific capacitance based on $\text{H-TiO}_2/\text{MnO}_2$ nanowires (449.6 F g^{-1}),^[179,180] $\text{Zn}_2\text{SnO}_4/\text{MnO}_2$ nanowires (642.4 F g^{-1}),^[121] $\text{SnO}_2/\text{MnO}_2$ nanowires (800 F g^{-1}),^[120] MnO_2/Mn nanotubes (937 F g^{-1}),^[117] MnO_2/TiN nanotubes (834 F g^{-1} , 681 F g^{-1}),^[118,119] $\text{Co}_3\text{O}_4/\text{Pt}/\text{MnO}_2$ (539 F g^{-1}),^[181] and networks of highly conductive metals coated by MnO_2 (385 F g^{-1})^[122,178] were reported. A detailed study is shown in Table A1 in the appendix.

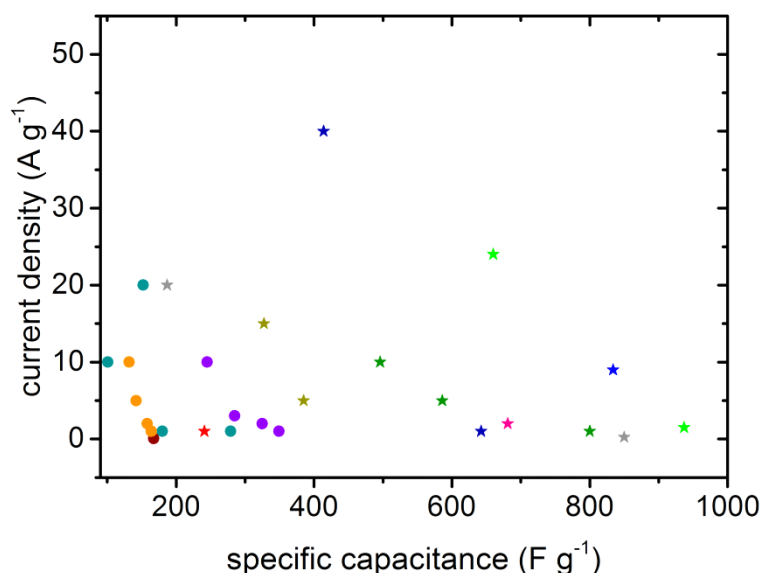


Figure 2-5 | Comparison of the rate capability of various MnO_2 based structures. Star-shape core/shell structures and circle bare MnO_2 structures.

- ★ MnO_2/Mn ,^[117]
- ★ MnO_2/TiN ,^[118] ★ MnO_2/TiN ,^[119] ★ $\text{MnO}_2/\text{SnO}_2$,^[120] ★ $\text{MnO}_2/\text{Zn}_2\text{SnO}_4$,^[121]
- ★ MnO_2/Au ,^[122] ★ MnO_2/Ni ,^[123] ★ $\text{MnO}_2/\text{aMEGO}$,^[124] ★ $\text{MnO}_2 \text{ NT}$,^[115] ★ $\text{MnO}_2 \text{ NW}$,^[24]
- ★ $\text{MnO}_2 \text{ NW}$,^[110] ★ MnO_2/CNT ,^[130]

2.4.5 Metal nitrides

Metal nitrides have received scarce attention for supercapacitor applications in comparison to metal oxides and carbon based materials, which have been extensively studied in literature.^[37] Thereby, metal nitrides exhibit superior properties compared to metal oxides, such as high electrical conductivity, high specific capacitance, and in some cases better chemical stability.^[16,37,151] Among other nitrides, such as molybdenum nitride^[182] and titanium nitride,^[183] is vanadium nitride (VN) considered to be one of the most promising nitride based materials for supercapacitor applications.^[6,151] In previous studies, Choi et al. explored nanocrystalline VN powders and reported an extremely high specific capacitance (1340 F g^{-1}),^[16] Ghimbeu et al. studied VN/CNT composites (270 F g^{-1}),^[149] Zhou et al. analyzed TiN/VN core/shell structures (247.5 F g^{-1}),^[153] and Glushenkov et al. reported porous VN with a high mass loading (186 F g^{-1}).^[147] The large differences in the reported specific capacitance values can most likely be attributed to the large diversity within the material synthesis methods, which often include oxide precursors that will lead to oxy-nitride rather than pure nitride materials, and to the varying characterization procedure. However, the main challenge of metal nitride supercapacitors is based in the poor long-time cycling ability.^[37] Most publications on metal nitride based supercapacitors have not investigated the long-time cycling ability or report an insufficient capacitance retention (e.g., 88 % for TiN-VN fibers after 500 cycles,^[184] 89 % for TiN/VN composite after 500 cycles,^[148] ca. 20 % for TiN nanowires after 4000 cycles^[185]). Merely Lu et al. could report improved cycling ability of TiN by using a PVA/KOH gel electrolyte to prevent structural degradation and, most recently, for hydrothermally glucose coated TiN and VN nanowires (91.7 % and 88.4 % after 15000 cycles).^[185,186]

2.5 Symmetric and asymmetric aqueous based supercapacitors

Aqueous based supercapacitors can generally be classified into two different groups, namely symmetric and asymmetric supercapacitors. Symmetric supercapacitors consist of negative and positive electrodes that are of the same kind (e.g., $\text{MnO}_2//\text{MnO}_2$ or AC//AC). In contrast, asymmetric supercapacitors are built up by utilizing different electrode materials at the negative and positive electrode (e.g., AC//MnO_2). It becomes obvious that symmetric supercapacitor configurations suffer from a major limitation when considering that the stored energy in a supercapacitor is proportional to the operating potential window squared, see eq. 2-1. Namely, the accessible operating voltage window

Electrochemical energy storage in supercapacitors

of symmetric supercapacitors is restricted by water dissociation at potentials above 1.23 V and by irreversible reduction processes that occur in pseudocapacitive materials, as in the case of MnO_2 , which forms lower valence soluble manganese oxides at negative potentials vs. Ag/AgCl .^[187] In order to overcome these restrictions, asymmetric supercapacitors with tailored negative and positive electrodes that show capacitive behavior in complementary voltage windows have been developed with the aim of extending the operating voltage window and by this means drastically increase the amount of energy stored in a supercapacitor. The combination of different materials at the positive and negative electrode enables the expansion of the operating voltage window in aqueous electrolytes beyond the thermodynamic limit of 1.23 V to stable voltage windows as high as 2.0 V. For example, it has been shown that an asymmetric AC/MnO_2 supercapacitor can reversibly operate at 2.0 V, whereas a symmetric $\text{MnO}_2//\text{MnO}_2$ supercapacitor can only work at 0.9 V.^[18] This effect is achieved because of high overpotentials for O_2 and H_2 evolution at the positive and negative electrodes,^[188] respectively. As a result, significantly higher amounts of energy can be stored compared to aqueous symmetric supercapacitors. The electrochemical data reported in literature for various aqueous symmetric and asymmetric supercapacitors is presented in Figure 2-6 and underlines the above discussion. As an example, an asymmetric supercapacitor configuration based on AC/MnO_2 can achieve 28.2 Wh kg^{-1} at 0.5 kW kg^{-1} ,^[189] whereas a symmetric $\text{MnO}_2//\text{MnO}_2$ configuration can only achieve 3.3 Wh kg^{-1} at 0.265 kW kg^{-1} .^[190] A detailed literature comparison that covers a wide range of reported symmetric and asymmetric devices with different material systems is summarized in Table A2 in the appendix. The positive electrode in asymmetric supercapacitors is typically based on a material that stores energy in a pseudocapacitive manner, such as MnO_2 and RuO_2 . While the negative electrode mainly consists of a high surface area activated carbon, where the charge is stored in an electric double-layer. Alternative candidates for negative electrodes are TiO_2 ,^[191,192] iron oxides,^[190,193-195] MoO_3 ,^[196,197] metal nitrides (e.g., TiN , VN)^[185,186,198] and conduction polymers (e.g., PANI, PPy, PEDOT),^[199,200] which exhibit pseudocapacitance in a complementary window to positive electrode materials. Negative electrode materials that show the best electrochemical performance in mild aqueous electrolytes are of particular interest in combination with MnO_2 because in such moderate-pH electrolytes is the performance of carbon based materials limited and typically achieve specific capacitance values of only 100 to 120 F g^{-1} compared to 150 to 400 F g^{-1} as in strong acidic or alkaline aqueous electrolytes.^[18,201] Therefore, alternative negative electrode materials with higher specific

capacitance values can further increase the electrochemical performance of supercapacitors. Hence, the selection of suitable negative and positive electrodes is a key criterion to further improve the electrochemical performance of aqueous supercapacitors. In particular, the search for high performance negative electrode materials is inevitable.^[202] Further, advantages of aqueous asymmetric supercapacitors include: (i) A higher degree of safety during operation compared to supercapacitors based on organic electrolytes; (ii) Less radical environmental conditions during fabrication and assembly; (iii) The circumvention of the use of toxic, expensive and corrosive electrolytes; (iv) Specific energy that can compete with reported values for non-aqueous EDLC.

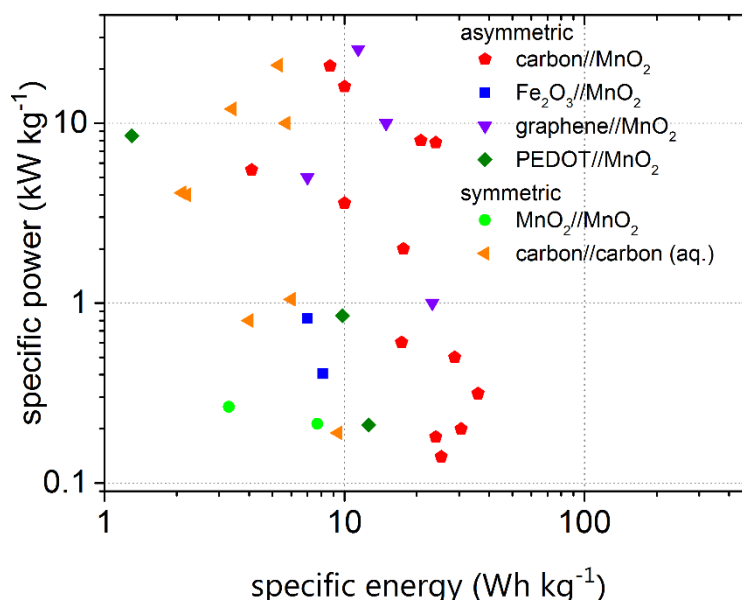


Figure 2-6 | Ragone plot, showing reported specific energy (E) and specific power (P_{real}) values of symmetric (MnO_2 // MnO_2 ,^[190,203] carbon//carbon^[204-206]) and asymmetric supercapacitors (carbon// MnO_2 ,^[32,188-190,207-212] Fe_2O_3 // MnO_2 ,^[190,193] graphene// MnO_2 ,^[33,213,214] PEDOT// MnO_2 ,^[203] and PPy// MnO_2).

2.6 Confusion and uncertainty concerning supercapacitor device performance reported in literature

The research interest concerning supercapacitors has increased rapidly over the last decade (please refer to Figure A1 in the appendix) and various materials and structures have been reported. However, the comparison of reported device and electrode performance metrics among different publications can be quite tedious and may lead to

Electrochemical energy storage in supercapacitors

confusion and uncertainty. While comparing reported supercapacitor devices the following aspects should be considered.

The devices performance depends strongly on the electrochemical testing procedure. It should clearly be distinguished between single-electrode measurements in a three-electrode configuration (*i.e.*, working electrode, counter electrode, reference electrode) and a two-electrode device (*i.e.*, positive electrode and negative electrode). Three-electrode measurements are only valid to determine the specific capacitance of a material (*e.g.*, compare performance of different morphologies), investigate the stable operating potential window, study long-time cycling stability, and performing electrochemical impedance spectroscopy. Such measurements are inappropriate to predict device level performance and should not be used to calculate specific energy and specific power (*i.e.*, in a symmetric device, the device specific energy is at best only 25 % of the single electrode specific capacitance).^[18] The investigation of the device level performance requires the assembly and testing of a two-electrode device. Further, similar device configurations or materials may exhibit different specific capacitance values. This discrepancy may arise from different active material loadings, varying electrode fabrication, and diverse electrolyte compositions. In general, it has been shown that higher mass loadings show lower specific capacitance values and vice versa. In addition, the specific power capability of supercapacitor has been reported in literature using different definitions. The most widely adopted approaches to determine the specific power of a supercapacitor device are (i) matched impedance power ($R = R_S$ (equivalent series resistance)) and (ii) real specific power (P_{real}), which is obtained by dividing specific energy by operational discharge time.^[18] The determination of the specific power is influenced by factors such as cell assembly, the pressure applied to the stack, the amount of electrolyte, and the type of separator. Therefore, the evaluation of specific power (determined using the equivalent series resistance) is often neither comparable with other literature values nor representative of commercial devices.^[18] It should also be noted that the specific power of commercial devices is often characterized by different techniques, such as the min/max method of the U.S. Advanced Battery Consortium and the pulse energy efficiency approach introduced by the University of California.^[215]

3 Three-dimensional nanostructures: Fabrication strategies and advantages for supercapacitor applications

Nanotechnology has developed a large variety of techniques to synthesize 0D (e.g., nanodots), 1D (e.g., nanowires and nanotube) and 2D nanostructures (e.g., nanosheets) in recent decades. However, the realization of functional self-supported 3D nanostructures still remains one of the most challenging topics in nanotechnology today. Existing strategies proposed by scientists can be classified into top-down and bottom-up approaches. Whereas top-down techniques are mainly based on lithography techniques^[216] (e.g., phase-shift lithography,^[217] laser lithography,^[218] two-photon lithography^[219]) and thus suffer from low through-put and high cost, bottom-up approaches are commonly based on self-assembly (e.g., spherical colloidal particles,^[220] DNA bricks,^[221] nanoxerography^[222,223]) and template assisted growth (e.g., anodic aluminum oxide,^[224,225] polystyrene spheres^[226,227]). In general, these fabrication strategies allow a high material through-put, do not require expensive equipment and provide an excellent control of the morphology within the nanometer regime. Hence, it is widely believed among scientists that self-supported 3D nanostructures fabricated from bottom-up approaches are highly promising candidates to accelerate the scientific and technological progress in various fields, including optics (e.g., photonic crystals^[228]), sensors (e.g., gas sensing^[229]), energy conversion (e.g., solar-water splitting,^[230] solar-cells^[231]) and energy storage (e.g., supercapacitors,^[229] Li-ion batteries^[26,232]). The following chapter will introduce the advantages that arise from 3D nanostructures with respect to supercapacitor applications and will emphasize key techniques to synthesize 3D nanostructures from bottom-up approaches with high structural controllability. Therefore, the concept of nano-porous anodic aluminum oxide templates will be introduced in detail and the beneficial use of atomic layer deposition in combination with these templates will be discussed.

3.1 Advantages of three-dimensional and complex core/shell nanostructured materials in supercapacitor applications

Until now, commercially available supercapacitors almost exclusively consist of two-dimensional planar thin film electrodes which experience limitations in energy storage capability. For example, it has been shown that thin films of active electrode materials

Three-dimensional nanostructures: Fabrication strategies and advantages for supercapacitor applications

(*e.g.*, MnO₂) on planar surfaces suffer from both, a low areal capacitance and a poor material utilization as the film thickness (*i.e.*, mass loading) increases,^[233] indicating that only a thin surface-layer contributes to the charge storage mechanism.^[18] Further, it is a crucial aspect, in particular in nanostructured electrode materials, to reach a compromise between specific surface area to guarantee high specific capacitance and pore size distribution (*i.e.*, electrode porosity) to ensure an easy transport of electrolyte ions into the active electrode material.^[9] In order to overcome these challenges the exploitation of a new dimension for charge storage in supercapacitor materials, namely the accomplishment of 3D nanostructures, is inevitable. 3D nanostructured supercapacitors will benefit from one of the most attractive advantages of nanostructured materials, the extremely large surface area and at the same time provide highly porous electrodes to prevent limitations that arise from electrolyte ion transport. In particular, self-supported (*i.e.*, free-standing) dense nanotube and nanowire arrays with high aspect ratios and large surface area have been investigated to fulfill these requirements, including carbon nanotubes,^[23,69] RuO₂ nanotubes,^[12] and MnO₂ nanowires and nanotubes.^[115] Unfortunately, it has been shown that promising high aspect ratio energy storage materials (*e.g.*, MnO₂ nanotubes and nanowires) suffer from high internal resistance,^[36,121] which results in low specific capacitance and poor rate capability, see Section 2.4. In order to overcome these restrictions and further enhance the performance of supercapacitors, advanced and more complex 3D nanostructures need to be developed. An attractive solution to address these challenge is offered by self-supported core/shell nanotube and nanowire arrays.^[6] Such nano-engineered materials combine the unique properties of two materials (*i.e.*, core and shell). Usually, the highly conductive core provides a fast electron transport through the entire electrode matrix and forms a 3D current collector. Whereas the thin shell (~20 nm thick) of the energy storage material (*e.g.*, pseudocapacitive material) ensures a good utilization of the active material and a short ion diffusion path length. Following this discussion, an ideal 3D supercapacitor electrode (see Figure 3-1) should satisfy the following three criteria:^[10] i) The active electrode material needs to coat a 3D scaffold in a thin film manner, as to ensure superior electrode kinetics and material utilization; ii) The 3D scaffold must consist of a porous high surface area framework with a high electrical conductivity; iii) The electrode as a whole must be self-supported or monolithic so that no resistive organic binders are needed for the electrode fabrication.

Three-dimensional nanostructures: Fabrication strategies and advantages for supercapacitor applications

In order to pave the way for such superior electrode materials innovative 3D nanostructuring techniques need to be developed. Mainly template-based techniques have been utilized as efficient methods to prepare functional core/shell nanostructures (e.g., ZnO nanorod template, colloidal nano-spheres, track-etched polymer template).^[234-238] However, the level of controllability of the proposed template-based techniques is partially limited to a few parameters and largely depends on the inherent structural nature of the template itself. Atomic layer deposition, as an efficient technique to prepare conformal thin films or tubular structures, in combination with highly controllable nanoporous anodic aluminum oxide templates, provides an excellent solution to further adjust more structural parameters and fabricate large arrays of high performance 3D core/shell nanotube arrays for supercapacitor electrodes.

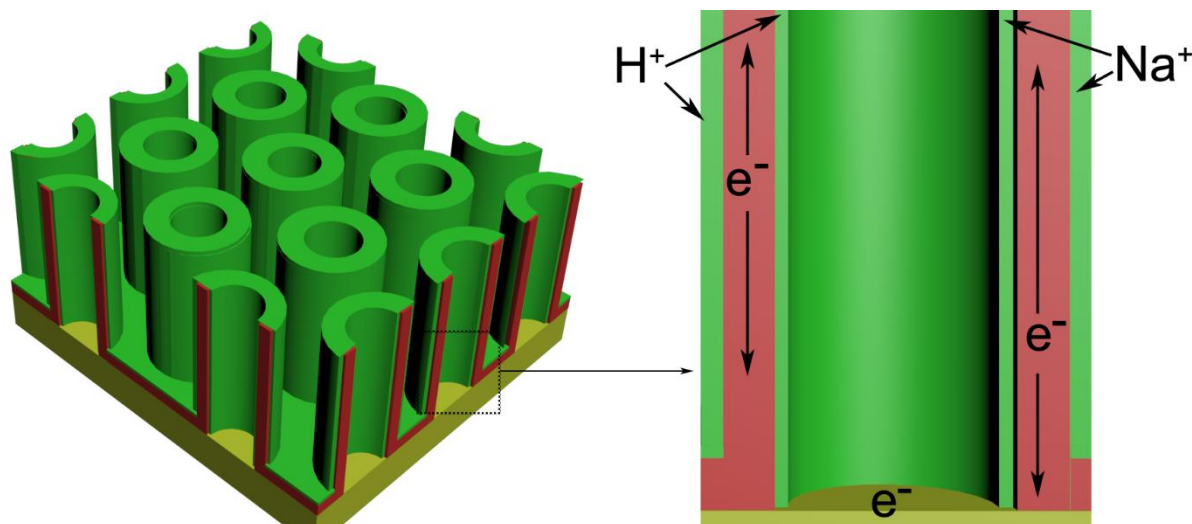


Figure 3-1 | Illustration of an ideal 3D supercapacitor electrode, providing a good electron transport along a conductive core material (red) and a good utilization of the active electrode material in the shell (green) (e.g., H^+ and Na^+ ions).

3.2 Atomic layer deposition

Atomic layer deposition (ALD) is a highly conformal monolayer (ML) by monolayer coating technique that has recently drawn much attention in the field of nanotechnology to fabricate and modify nanostructured materials. The technology was mainly developed by Suntola and coworkers under the name of atomic layer epitaxy in the mid-1970s in Finland.^[239,240] ALD is a unique tool that is capable of coating complex geometries, high aspect ratio materials, and porous 3D nanostructures with a large variety of materials,^[241-243] including metals (e.g., Pt, Ru, Ir, Pd, Cu, Ni, Co, Fe),^[244-249] metal oxides (e.g., SnO_2 , Al_2O_3 , TiO_2 , ZnO , HfO_2),^[250-254] metal sulfides (e.g., ZnS , CuS , GaS),^[255-257] and metal

Three-dimensional nanostructures: Fabrication strategies and advantages for supercapacitor applications

nitrides (e.g., TiN, TaN, WN, NbN)^[254,258-262] (please refer to Figure A2 in the appendix for a detailed overview of processable materials). Thereby, pin-hole free thin films can be fabricated with a precise thickness control in a self-limiting behavior. The easy scalability and manufacturability of this technique makes it not only interesting for scientific research, but also a desired tool for industrial applications, such as the fabrication of high-k gate oxide materials in semiconductor industry and thin films for display technology.^[250,254,263] Thereby, ALD does not require any target preparation as in PVD and no flow control as in CVD processes.

The basic working principle of ALD is generally based on two different precursor molecules that are processed in 4 consecutive steps. Thereby, ALD separates a conventional CVD technique into two half-reactions. Figure 3-2 shows a simplified scheme of a complete ALD cycle. In the first step, the first precursor is introduced into the vacuum chamber by a short pulse (typically 0.1 to 1 s). The precursor chemisorbs on the surface of the specimen.^[264,265] The absorption continues in a self-limiting behavior until one ML is attached to the surface of the specimen.^[266] In the second step, the remaining precursor is purged out of the chamber by an inert gas to prevent CVD like growth in the following process. In the third step, the second precursor is pulsed into the chamber and reacts with the first precursor. The reaction occurs on the surface of the specimen and a conformal atomic scale deposition is achieved (typical growth rate $\sim 0.1 \text{ \AA}$ per cycle). The remaining precursor and reaction by-products are purged out of the chamber in the fourth step, which completes one full cycle. This process can be repeated consecutively until a desired film thickness has been grown.

The successful deposition of thin films by ALD requires the fabrication conditions to be within the so called “ALD window”, as shown in Figure 3-3. This window describes the temperature dependent range within a ML by ML growth is observed. In case of too low temperatures precursor condensation on the specimen can occur or only insufficient energy is available for surface reactions. ALD at too high temperatures will lead to

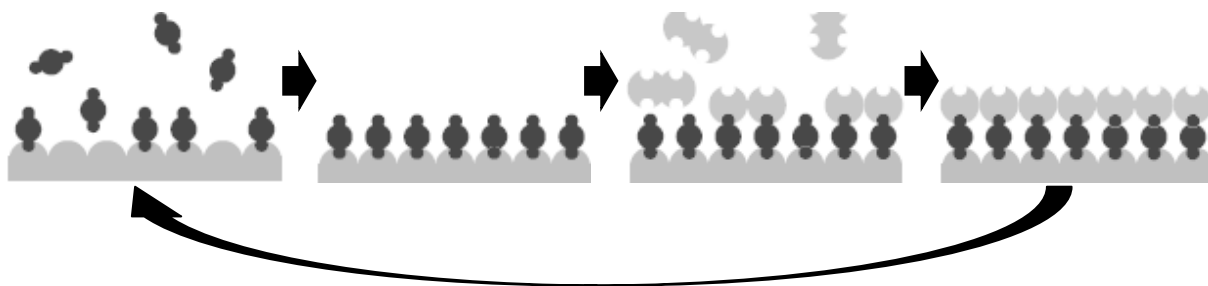
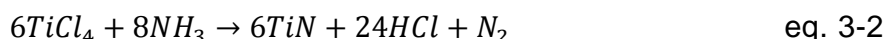


Figure 3-2 | Simplified 4 step process of ML by ML film growth in ALD.

Three-dimensional nanostructures: Fabrication strategies and advantages for supercapacitor applications

precursor desorption from the specimen or precursor decomposition. Therefore, it is a necessity to operate ALD in the suitable process window, which is typically in the range of ~100 to 400 °C depending on the precursor type and the reaction kinetics.

In this thesis, SnO₂ and TiN are deposited by ALD from SnCl₄ and TiCl₄ in combination with H₂O and NH₃ according to the following reactions:



The experimental details can be found in Section 4.1.2 and 4.1.6, respectively.

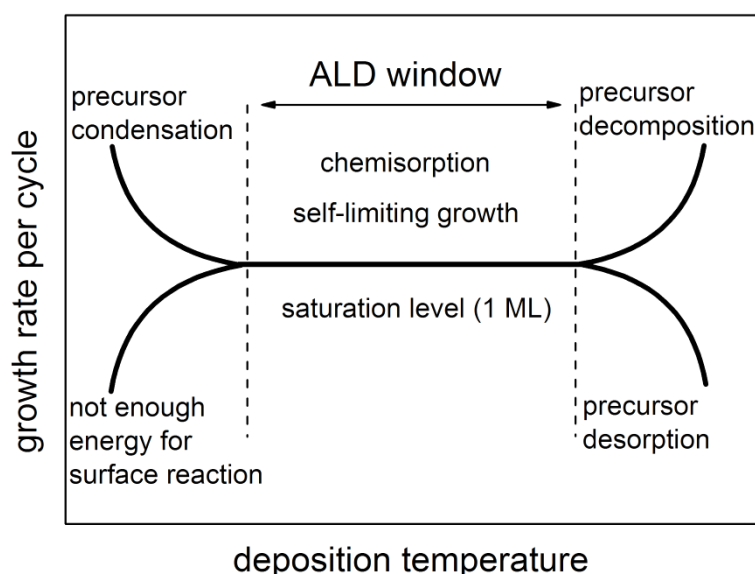


Figure 3-3 | ALD window for conformal ML by ML growth in dependence on the deposition temperature.

3.3 Anodic aluminum oxide a nano-porous template for three-dimensional nanostructuring

Nano-porous anodic aluminum oxide (AAO) was discovered by Keller et al.^[267] in 1953 and has been studied intensively since then.^[224,268-287] AAO is fabricated by electrochemical anodization of aluminum (Al) foils and exhibits a highly ordered hexagonal pore array which is formed by a self-organization process. Thereby, AAO mimics the structure of various materials observed in nature such as the skeleton of diatoms^[288] and the microscopic structure of peacock feathers,^[289] which is responsible for the colors of the plumage. The remarkable properties of AAO such as nanometer sized channels, adjustable pore size and length, thermal stability, hardness, large surface area, high porosity, easy scalability, and good processability (e.g., ALD, PVD,

Three-dimensional nanostructures: Fabrication strategies and advantages for supercapacitor applications

CVD, sputtering, sol-gel coating, electrochemical deposition, layer by layer growth, and coaxial lithography^[290] have made it into a widely used template to synthesize ordered 2D and 3D arrays of different nanostructures. In the last two decades, AAO templates have been utilized to fabricate a large variety of nanowire, nanotube, and nanodot arrays from different materials including metals,^[291-296] semiconductors,^[297-299] polymers,^[300] carbons,^[301,302] and other types of materials.^[303] Thereby, AAO and functional nanostructures based on AAO have been reported in gas- and bio-sensing applications (e.g., NO₂ detection,^[304] glucose sensing^[305]), in biochemical applications (e.g., drug delivery,^[306] cell adhesion^[307]), as a molecular separator,^[308] in catalysts,^[309] in magnetic applications,^[291,310] in electronic devices,^[311] and in energy storage applications (e.g., lithium-ion batteries,^[312,313] metal-insulator-metal capacitors,^[242] supercapacitors^[13,36]).

3.3.1 Structural features of anodic aluminum oxide

The structure of nano-porous AAO is based on a close-packed hexagonal cell arrangement with parallel cylindrical pores, which are orientated perpendicular to the surface and are separated from each other by an Al₂O₃ pore wall. The end of each pore is closed by a hemispherical Al₂O₃ shell termed in literature as the barrier layer (BL). Figure 3-4 shows a top view SEM, cross-section SEM, and schematic diagram of AAO prepared in oxalic acid at 40 V.

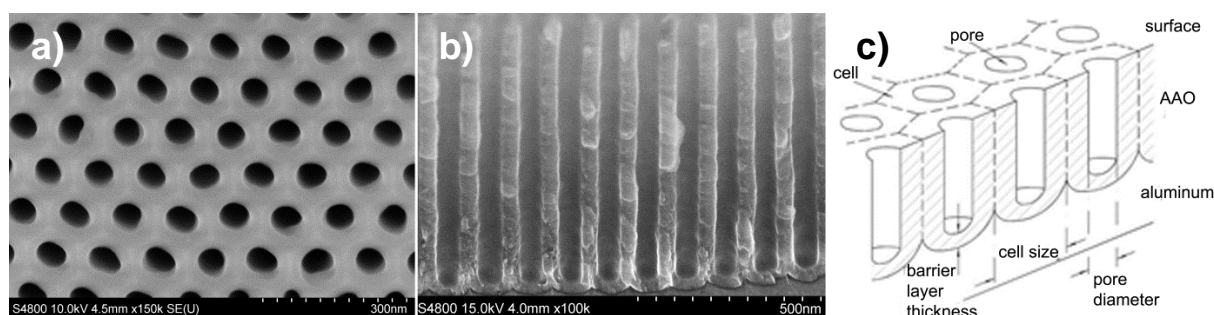


Figure 3-4 | Self-organized nano-porous AAO template fabricated at 40 V in oxalic acid. (a) Top view SEM image, (b) cross-section SEM image and (c) schematic diagram of AAO. (Figure taken from Ref.^[224])

AAO is a highly controllable self-organized nano-porous template that can be characterized by the six following parameters: pore diameter (10 to 400 nm), interpore distance (50 to 500 nm), pore length (10 nm to ~150 μ m), aspect ratio (2 to ~5000), pore density (10⁹ to 10¹¹ cm⁻²), and pore regularity.

The pore diameter (D_p) of AAO can be controlled in a precise manner in the range of 10 to 400 nm by adjusting the anodization voltage. Thereby, it has been found empirically

Three-dimensional nanostructures: Fabrication strategies and advantages for supercapacitor applications

that the pore diameter is linearly proportional to the anodization potential (U) in Volt with a proportional constant $\lambda_p = 1.29 \text{ nm V}^{-1}$: (Ref.^[274], chapter 1.2)

$$D_p = \lambda_p U \quad \text{eq. 3-3}$$

Further adjustments of the pore diameter can be achieved by a post anodization process called “pore widening”. In this process the thickness of the pore wall is reduced and the pore diameter is increased by a chemical etching process, as shown in Figure 3-5.

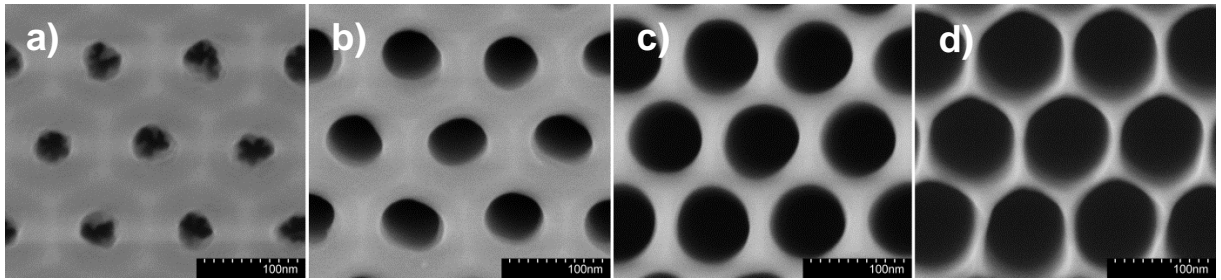


Figure 3-5 | Pore widening of an AAO template in 5 wt. % H_3PO_4 for (a) 0 min, (b) 15 min, (c) 30 min and (d) 45 min. The SEM images display one hexagonal unit-cell and show the increase of the pore diameter and the associated decrease of the pore wall thickness at different etching times. The pore diameters can be adjusted continuously between (a) $(39 \pm 4) \text{ nm}$ and (d) $(89 \pm 4) \text{ nm}$. The presented AAO templates were prepared at 40 V in oxalic acid.

The interpore distance and the self-ordering regimes of AAO are two important factors that need to be considered during the fabrication process, as shown in Figure 3-6. First, the presented diagram describes the relationship between the applied anodization voltage and the resulting interpore distance D_{int} for mild-anodization (MA) and hard-anodization (HA). The interpore distance of AAO prepared by MA using H_2SO_4 , $\text{H}_2\text{C}_2\text{O}_4$, and H_3PO_4 shows an empirically found linear dependence of the applied anodization voltage with a proportional constant $\lambda_{int;MA} = 2.5 \text{ nm V}^{-1}$ and can be controlled in the range of 50 to 500 nm:^[273]

$$D_{int} = \lambda_{int} U \quad \text{eq. 3-4}$$

In comparison, the proportional constant $\lambda_{int;HA} = 2.0 \text{ nm V}^{-1}$ for AAO fabricated by HA is lower than for MA.^[273] Second, Figure 3-6 outlines the self-ordering regimes for AAO prepared in different electrolytes and the associated anodization voltages. Thereby, it is noteworthy that self-ordering of AAO with an interpore distance in the range of $D_{int} = 200$ to 300 nm can only be achieved by HA in $\text{H}_2\text{C}_2\text{O}_4$. Self-ordering regimes with shorter and larger interpore distances are accessible by conventional MA in H_2SO_4 , $\text{H}_2\text{C}_2\text{O}_4$, and H_3PO_4 .

Three-dimensional nanostructures: Fabrication strategies and advantages for supercapacitor applications

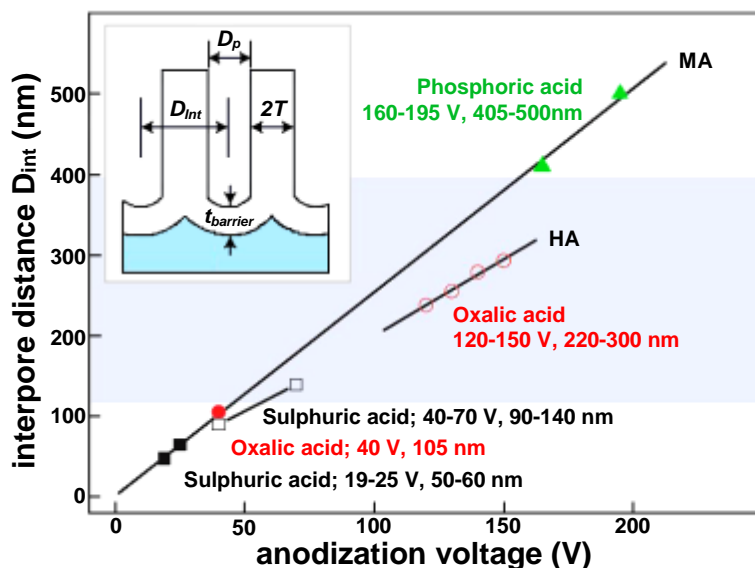


Figure 3-6 | Summary of reported self-ordering regimes of AAO templates fabricated by mild- and hard-anodization and the corresponding interpore distance (D_{int}) for an anodization in sulphuric, oxalic, and phosphoric acid. (Figure taken from Ref.^[273])

AAO templates prepared by a conventional two-step anodization process within the self-ordering regime exhibit perfectly ordered pore arrangements with a domain size of up to a few square micrometers,^[269] as shown in Figure 3-7a. In order to further increase the structural regularity a pre-structuring of the aluminum foil by nano-imprinting can be utilized.^[244,314] The anodization of an imprinted Al foil leads to the growth of perfectly ordered AAO templates without any defect up to square millimeter in size, as presented in Figure 3-7b. It is noteworthy that the geometry of the pore array can be changed by the pre-structuring technique from a hexagonal to a quadratic pore arrangement.

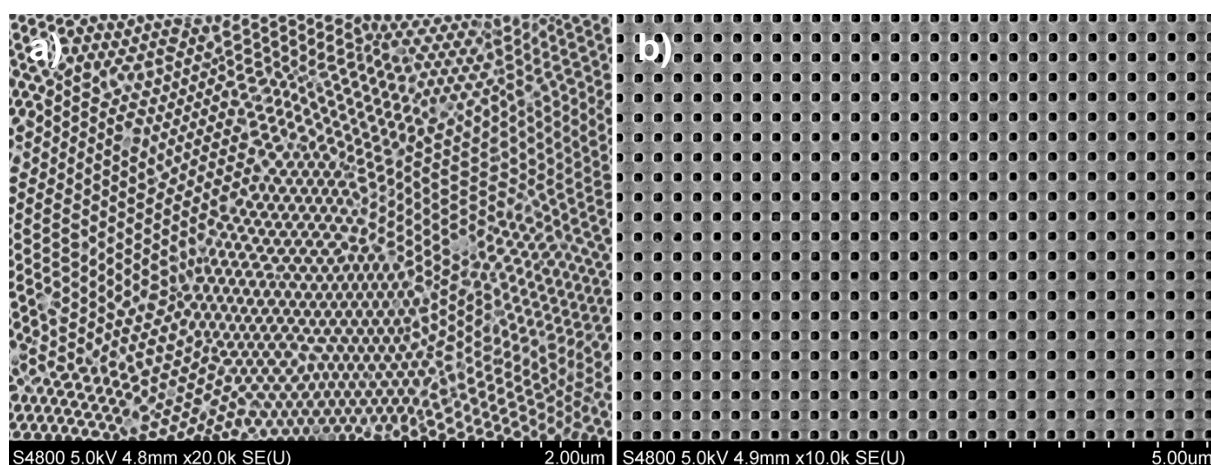


Figure 3-7 | Comparison between (a) conventional templates with highly ordered domains up to μm^2 in size and (b) pre-structured AAO templates with a perfectly ordered pore array up to mm^2 in size.

Three-dimensional nanostructures: Fabrication strategies and advantages for supercapacitor applications

3.3.2 Formation process of anodic aluminum oxide

Anodic aluminum oxide templates are commonly synthesized by an anodization process under constant potential. A typical current density vs. time profile recorded during the anodization from pure aluminum foils to porous AAO is shown in Figure 3-8. At the early stage of the anodization (i) the current decreases rapidly with increasing anodization time. In this step, an aluminum oxide barrier film is formed on the surface of the aluminum and grows with increasing anodization time. Further anodization (ii) results in initiation and formation of pores at impurities, dislocations, grain boundaries, non-metallic inclusions, and surface asperities.^[316,317] The current density increases and reaches a local maximum (iii). Here, the breakdown of the tight barrier film occurs and the porous structure begins to build. (Ref.^[274], chapter 1.3) Finally, the anodization current density levels off (iv) and a steady-state growth of porous aluminum oxide is observed.

3.3.3 Steady-state growth of anodic aluminum oxide

During steady-state growth, the following chemical reactions dominate the anodization process from pure aluminum to AAO in an acidic electrolyte.^[224,277,318]

- i) Al^{3+} ions are formed at the metal/oxide interface:



- ii) Water is electrochemically dissociated at the pore bottom near the electrolyte/oxide interface:

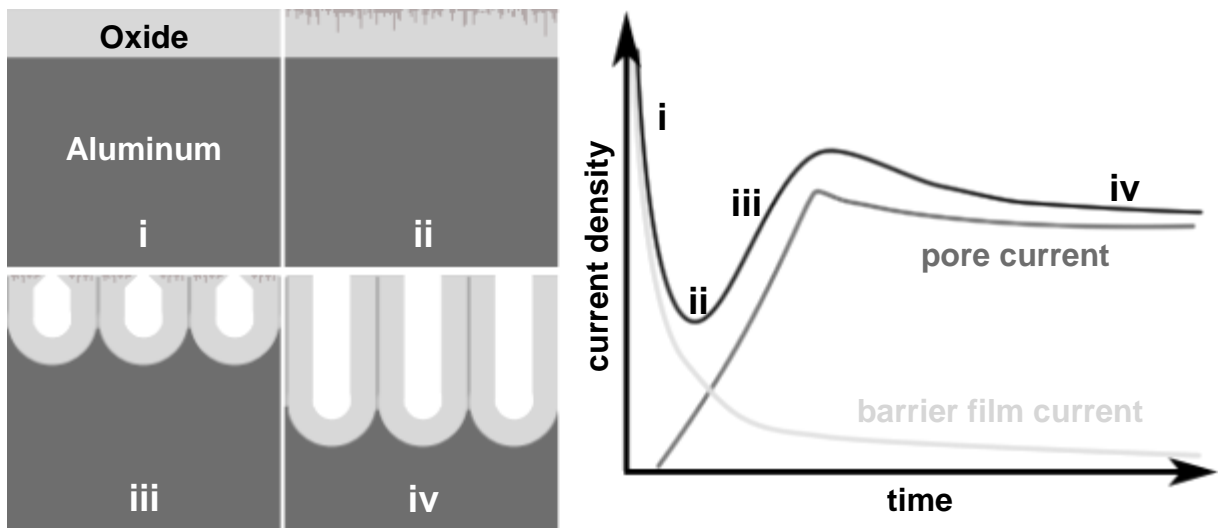
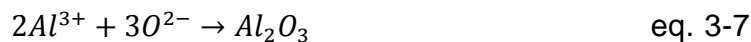


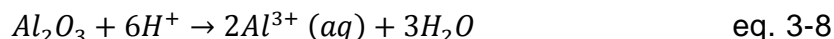
Figure 3-8 | Schematic illustration of AAO formation and the associated kinetics during AAO growth in the potentiostatic regime. (Figure redrawn from Ref.^[274], chapter 1.3)^[315]

Three-dimensional nanostructures: Fabrication strategies and advantages for supercapacitor applications

- iii) The formed O^{2-} ions migrate through the barrier layer from the electrolyte/oxide to the metal/oxide interface and react with the Al^{3+} ions to Al_2O_3 :



- iv) An electric-field-enhanced oxide dissolution occurs at the electrolyte/oxide interface:



In the case of steady-state growth, the electric-field-enhanced oxide dissolution at the electrolyte/oxide interface and the formation of Al_2O_3 at the oxide/metal interface are balanced. This balance is a crucial factor in AAO growth. It leads to a constant thickness of the barrier layer during the entire anodization process and enables steady-state pore propagation into the aluminum. The electric-field-enhanced dissolution separates the nano-porous AAO formation in an acidic environment apart from non-porous alumina, which forms in a neutral solution.^[224] In non-porous alumina anodization the oxide dissolution process is hindered and a continuous Al_2O_3 layer is formed. The thickness of this layer is linearly proportional to the applied anodization potential.^[277]

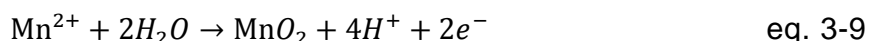
3.4 Electrochemical deposition and polymerization

Electrochemical deposition of metals, metal oxides and electrochemical polymerization of monomers are excellent and widely utilized tools to fabricate conformal thin films on two-dimensional substrates.^[319] In the last two decades, this technique was successfully transferred into nanotechnology and it has been shown that nanostructures (e.g., nanotubes and nanowires^[36]) can be fabricated by this concept. However, this technique is capable of synthesizing more complex and advanced nanostructures. In particular, tailored three-dimensional core/shell nanostructures can be fabricated by coating a thin shell on a three-dimensional conductive scaffold. Therefore, it is crucial to control the deposition time (*i.e.*, charge passed during the deposition process), adjust the electrolyte concentration, apply a suitable deposition potential and identify the best electrochemical technique (e.g., constant potential, constant current, potential sweep). The possibility to process a large variety of materials without the use of expensive equipment emphasizes that electrochemical deposition has great potential to nano-engineer unique functional nanostructures with novel properties.

Three-dimensional nanostructures: Fabrication strategies and advantages for supercapacitor applications

3.4.1 Electrochemical deposition of manganese dioxide

MnO₂ can be electrochemically deposited from soluble Mn²⁺ ions at pH 5 to 6 and a potential of 1 V vs. Ag/AgCl (3 M KCl) (*i.e.*, 1.207 V vs. SHE), as shown in the Pourbaix diagram in Figure 3-9 for the Mn–O₂–H₂–H₂O system. The overall reaction mechanism to form MnO₂ by anodic electrochemical deposition from an aqueous electrolyte containing Mn²⁺ ions, like in manganese acetate, can be formulated as follows:



However, it is unlikely that this reaction occurs in a single step. It is proposed that Mn³⁺ is formed as an intermediate state and either is subsequently disproportionated into Mn²⁺ and Mn⁴⁺ or it may hydrolyze to MnOOH and is then oxidized to MnO₂.^[320]

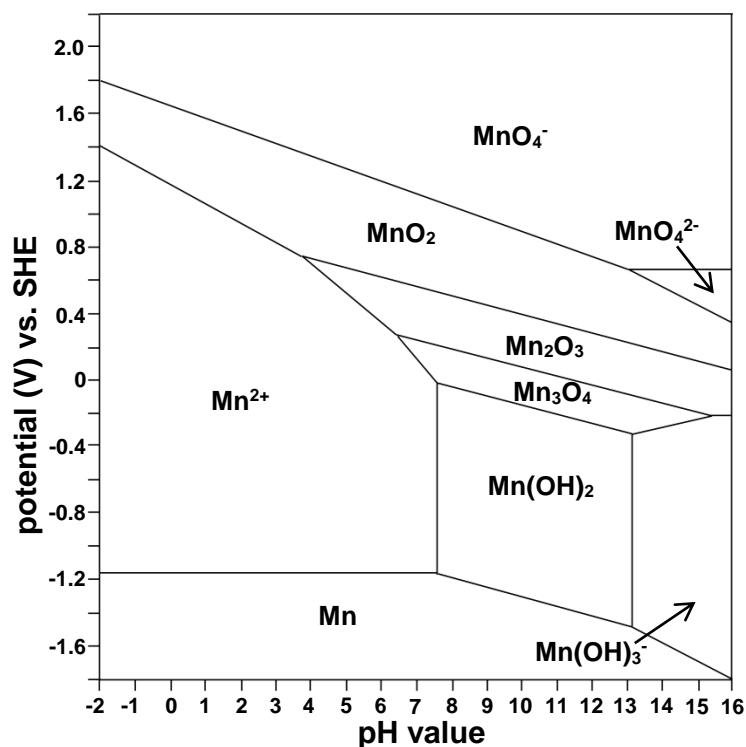


Figure 3-9 | Potential vs. pH diagram for the Mn–O₂–H₂–H₂O system at 25 °C. (Figure redrawn from Ref.^[321], chapter 1.2.1)

3.4.2 Electrochemical polymerization of pyrrole

Polypyrrole can be fabricated by anodic electrochemical polymerization of pyrrole monomers on the surface of a conductive substrate (*e.g.*, 3D nanotube array). Thereby, thin films with a fine thickness control can be synthesized by adjusting the electrochemical polymerization time, voltage and total charge passed. Other polymerization techniques (*e.g.*, chemical polymerization) are not capable for forming

Three-dimensional nanostructures: Fabrication strategies and advantages for supercapacitor applications

conformal thin films of PPy in a 3D manner and in addition, add reactant reagents and by products that may affect the properties of the conducting polymer.

The polymerization mechanism of pyrrole monomer to polypyrrole by electrochemical polymerization has been studied in the past and can be understood as described in Figure 3-10.^[103,322,323] In the initial step, pyrrole monomers are oxidized to radical cations ($C_4NH_5^+$). In the second step, bipyrrole dimers are formed by radical-radical coupling and deprotonation. The polymer chain growth through consecutive re-oxidation and coupling with other radical cations (repeating step three and four) and polypyrrole is synthesized.

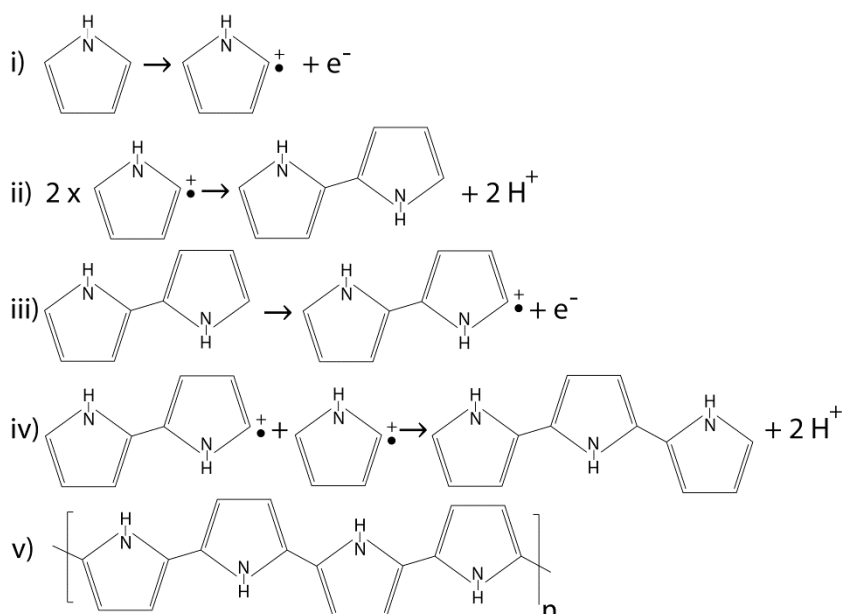


Figure 3-10 | Reaction scheme of the electrochemical polymerization of pyrrole. i) neutral monomer is oxidized to a radical cation; ii) coupling of two radical cations; iii) oxidation of bipyrrole; iv) chain growth; v) polypyrrole.

3.5 Functional carbon coating to improve the performance of energy devices – Challenges for three-dimensional nanostructures

The coating of thin carbon films on functional nanomaterials has attracted great attention in nanomaterials research. It has been shown, that in particular energy related applications, such as solar water splitting, supercapacitors, and Li-ion batteries can strongly benefit from carbon coatings.^[186,324-329] For example, Deng et al.^[324] reported an improved photocurrent of carbon coated hematite nanostructures compared to non-carbon coated hematite for solar water splitting, Lu et al.^[186] showed that hydrothermally

Three-dimensional nanostructures: Fabrication strategies and advantages for supercapacitor applications

carbon coated metal nitrides exhibit improved cycling stability, Wang et al.^[327] investigated the effect of carbon coatings on LiFePO_4 to enhance the electrochemical performance of the material for Li-ion batteries, and Balducci et al. showed that carbon coated iron oxide nanoparticles exhibit very promising performance for Li-ion batteries in terms of both, capacity retention at high current density and cycling stability.^[328,329] Hence, functional carbon coatings can modify the surface of active materials to enhance photoelectrochemical processes, improve long-time cycling stability, prevent the active materials from corrosion and degradation, and increase the conductivity of energy storage materials with poor intrinsic electric conductivity. Today, nanostructured materials are commonly carbon coated by methods such as chemical and physical vapor deposition and hydrothermal glucose coating with subsequent carbonization.^[186,330] It should be noted that in all these techniques the functional carbon coating on the active material is prepared after the active material synthesis, which indicates that the active material needs to undergo high temperature processes, as in hydrothermal glucose coating and chemical vapor deposition, or can only be prepared in a directed manner, as in physical vapor deposition. Hence, these approaches may result in a poor structural controllability, non-conformal coating on self-supported nanostructure arrays, and collapse of the nanostructured active material during high temperature carbonization processes.^[17] Moreover such techniques were developed for thin films and powder samples and are not capable of coating self-supported three-dimensional nanostructure arrays. Hence, nanotechnology is currently lacking a carbon coating technique that is capable of coating complex three-dimensional nanoarchitectures in a conformal manner.

4 Experiments and methods

All experiments and methods throughout this work were performed and carried out according to the procedures described in this section. This section presents the fabrication conditions that were used to prepare the self-supported three-dimensional nanostructures based on AAO templates, ALD, and electrochemical deposition in detail and describes the analytical tools utilized to investigate the morphology, chemical composition and electrochemical performance.

4.1 Template assisted fabrication of three-dimensional nanostructures

4.1.1 Anodic aluminum oxide template

The fabrication of well-ordered nano-porous AAO templates was realized by a two-step anodization process initially proposed by Masuda and Satoh.^[279] Figure 4-1 presents the required steps and conditions in a flow diagram to synthesize AAO templates, using oxalic acid as an electrolyte. All steps are equivalent for AAO preparation in sulphuric and phosphoric acid. The respective conditions can be found in literature.^[285,331,332] The complete synthesis process of AAO consists of three essential steps. The pre-treatment of the aluminum foil, the two-step anodization process and the post-treatment of the AAO. The pre-treatment was required to assure a well-ordered growth of high quality AAO templates. Therefore, high purity aluminum foils (99.999 %) were used as a starting material. The foils were washed in an ultrasonic bath with acetone, ethanol, and water for 10 minutes each to degrease and clean the samples. Afterwards the samples were electrochemically polished in a mixture of perchloric acid and ethanol (vol. ratio 1:7) for 2 minutes to remove surface asperities. The as pre-treated aluminum foils were then anodized in a two-step anodization process. The first anodization step was carried out for 6 h. Thereafter, the formed anodization product was chemically removed at 60 °C in a solution of 6 wt. % H_3PO_4 and 1.8 wt. % H_2CrO_4 . This specimen was anodized again, using the same conditions as the first anodization. The time of the second anodization determines the final thickness of the AAO template, which can be adjusted from a few hundreds of nanometers to several tens of micrometers (approx. growth rate 120 nm min^{-1} for the conditions presented in Figure 4-1). The post-treatment allows the modification of the AAO template in a way to meet the desired requirements. The aluminum base can be removed, the pores size can be adjusted and the barrier layer be

Experiments and methods

removed to fabricate through-hole templates. In this study, AAO templates were fabricated with a second anodization time of 5 to 15 minutes and the pores were widened in a 5 wt. % H_3PO_4 solution for 15 minutes at 30 °C. All other post-treatments were applied after the ALD deposition of SnO_2 and TiN.

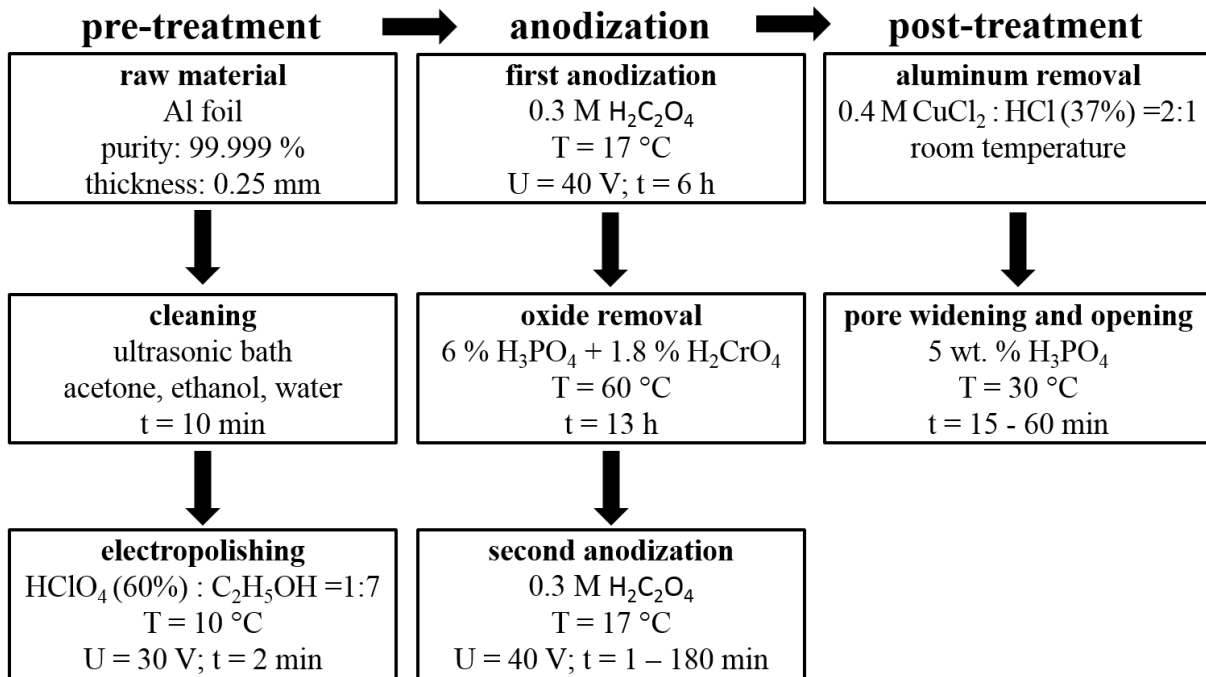


Figure 4-1 | The flowchart displays the procedure to fabricate high quality nanoporous AAO templates by a two-step anodization process, including required pre-treatments and optional post-treatments.

4.1.2 Atomic layer deposition of SnO_2

Atomic layer deposition of conformal SnO_2 films was achieved on a *PicoSun* ALD system by utilizing anhydrous SnCl_4 (98 % purity) purchased from *Stream Chemicals* and H_2O (semiconductor grade) as precursors. The precipitation of SnO_2 was realized according to the process plan shown in Figure 4-2. First, the SnCl_4 precursor was pulsed for 1 s and purged for 4 s and then the H_2O precursor was pulsed for 2 s and purged for 8 s. This procedure defines one ALD cycle and was repeated for 500 to 1500 times, depending on the desired wall thickness of the SnO_2 nanotubes. The reaction chamber temperature was kept constant at 250 °C for the entire process and the chamber pressure was 10 hPa. The carrier gas flow of both precursors was set to 100 sccm.

Experiments and methods

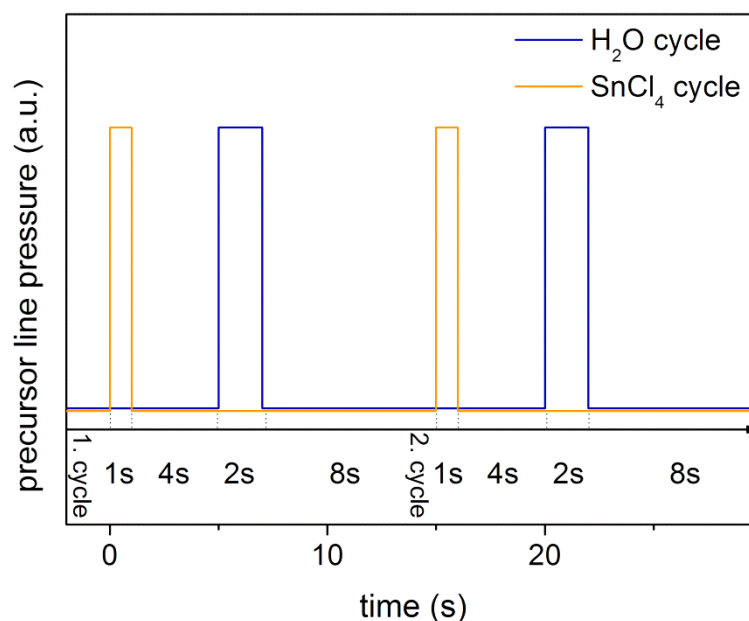


Figure 4-2 | ALD process for the fabrication of SnO₂ from the SnCl₄ and H₂O precursors, showing two full deposition cycles and the required pulse and purge times.

4.1.3 Open-end and closed-end SnO₂ nanotube arrays

Subsequent to the ALD process of SnO₂ a 100 nm thick gold layer was evaporated with a *Kurt J. Leskar* physical vapor deposition equipment onto the top-side of the SnO₂ containing AAO template. This layer served as a current collector on the supercapacitor electrode. Thereafter, the aluminum base was removed in a 2:1 0.4 M CuCl₂ : HCl (37 %) solution and the template was etched in a 5 wt. % NaOH solution at room temperature. Hereby, different processes for open-end and closed-end SnO₂ nanotube arrays were used. For the fabrication of closed-end nanotubes the AAO template was immersed in a NaOH solution for 120 minutes and the entire template was etched in a one-step process. In contrast, the formation of open-end SnO₂ nanotube arrays required a two-step etching process. First, the AAO template was etched for 20 minutes to liberate the nanotube top-ends, which were then removed by scratching the surface of the specimen with a sharp scalpel. Second, the specimen was immersed in the NaOH solution again and the remaining AAO template was removed.

4.1.4 Electrochemical deposition of MnO₂ and PPy

The as-prepared self-supported open-end and closed-end SnO₂ nanotube arrays were coated by either a MnO₂ shell for the use as a positive supercapacitor electrode or a PPy shell for the use as a negative supercapacitor electrode. All electrochemical deposition

Experiments and methods

and electrochemical polymerization processes were performed in a home build three-electrode cell with a Ag/AgCl (3 M KCl) reference electrode and a platinum foil 1 cm² counter electrode. The MnO₂ shell was precipitated from an electrolyte containing 0.1 M Mn(Ac)₂ and 0.1 M Na₂SO₄ at 1 V. The charge passed was controlled to be within the range of 130 to 260 mC. The PPy shell was coated onto the three-dimensional SnO₂ nanotube array from a freshly prepared electrolyte that contained 0.1 M pyrrole monomer (98 %) and 0.2 M oxalic acid at 0.8 V. The charge was controlled to be within the range of 130 to 510 mC. Afterwards all samples were cleaned with water and dried.

4.1.5 Synthesis of micelles and carbon coating of anodic aluminum oxide

In a first step, a low molecular weight phenolic resol was prepared based on a method described by Gu et. al.^[333] 1.4 mL formaldehyde (37 wt. %), 0.4 g phenol and 10 mL 0.1 M NaOH were mixed under continuous stirring for 45 minutes at 70 °C. Afterwards, 10 ml H₂O containing 640 mg of dissolved pluronic F-127 were added to the solution and stirred for 120 minutes at 70 °C. The obtained solution was diluted by adding 35 ml H₂O and then further stirred for 20 h. The color of the solution changed gradually from transparent to Bordeaux red during this process. After the micelle formation, 3 ml of the prepared solution were added into a 30 ml Teflon based autoclave and up to 3 AAO templates were immersed into the solution and kept still for 120 minutes. Thereafter, 26 ml H₂O were added, the autoclave was tightly sealed and placed into an oven for 20 h at 130 °C. After the hydrothermal process all AAO templates were cleaned with H₂O and tissue paper until the AAO templates shimmered slightly yellow. Then, the as-modified AAO templates were annealed at 550 °C for 2 h in N₂ atmosphere (3 °C min⁻¹ ramp rate) to obtain conformally carbon coated AAO templates.^[17]

4.1.6 Atomic layer deposition of TiN and electrode fabrication

C-TiN and TiN nanotube arrays were fabricated from carbon coated AAO templates (Section 4.1.5) and bare AAO templates (Section 4.1.1), respectively. The respective templates were placed into a *Picosun Sunale R-150* ALD reactor, the chamber pressure was decreased to 10 hPa and the temperature was increased to 400 °C. TiCl₄ (Stream Chemicals 99 %) and NH₃ (gas quality 6.0) were used as precursors. TiCl₄ was pulsed for 0.1 s and purged for 6 s. NH₃ was pulsed for 1 s and purged for 10 s. Figure 4-3 displays the full ALD cycle, which was repeated for 500 to 1000 times. The carrier gas flow of both precursors was set to 120 sccm. Subsequent to the ALD process a 100 nm thick gold layer was evaporated with a *Kurt J. Leskar* physical vapor deposition

Experiments and methods

equipment onto the top-side of the C-TiN and TiN containing AAO template. The Au layer served as a current collector for the supercapacitor characterization. Thereafter, the aluminum base was removed in a 2:1 0.4 M CuCl_2 : HCl (37 %) solution and the template was etched in a 5 wt. % NaOH solution at room temperature for 120 minutes.

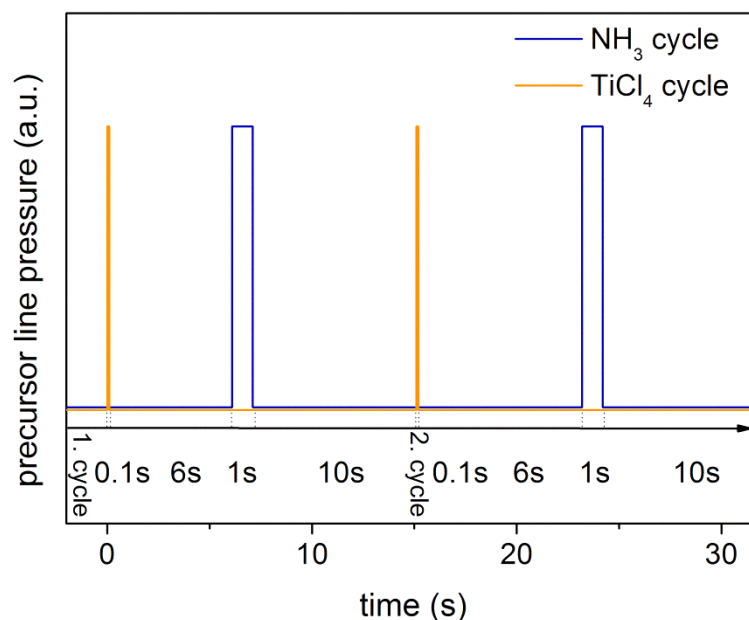


Figure 4-3 | ALD process for the fabrication of TiN from TiCl_4 and NH_3 precursors, showing two full deposition cycles and the required pulse and purge times.

4.2 Analytical methods

4.2.1 Field emission scanning electron microscopy

Field emission scanning electron microscopy (FE-SEM) is an analytical method to study the morphology of a specimen in the nanometer regime. An electron beam with a narrow energy distribution (0.25 to 0.5 eV) is generated in a field emitting cathode at typical acceleration voltages between 1 to 30 kV, focused by an electronic optic and scanned across the specimen. The incident electrons interact with the sample and generate three commonly utilized signals, namely secondary electrons (SE), back scattered electrons (BSE) and characteristic X-ray radiation. The detection of SEs is highly desirable for the visualization of three-dimensional nanostructures. SEs are emitted from the surface (< 50 nm) of a specimen with low kinetic energies (typically < 50 eV) and are detected by an Everharth-Thornley detector.^[334] This detection principle results in images with low noise and a three-dimensional impression of the recorded structure. Therefore, FE-SEM images were almost exclusively utilized in this work to study the prepared

Experiments and methods

nanostructures. The signal from BSEs is mainly analyzed to visualize the material distribution in a specimen by the material contrast (*i.e.*, back scattering is proportional to Z^2). Characteristic X-ray radiation can be accessed to study the chemical composition of a specimen in energy dispersive X-ray spectroscopy (EDX). The imaging of three-dimensional nanostructures further benefits from the high field depth in SEM, leading to a sharp visualization across a long vertical distance, which is highly desirable for high aspect ratio materials (*e.g.*, self-supported nanotube arrays on surfaces). These features make FE-SEM an indispensable tool in nanotechnology. All measurements were performed on an ultra-high resolution *Hitachi S4800* FE-SEM at 4 to 8 mm working distance with acceleration voltages in the range of 5 to 15 kV and a resolution of 1 to 2 nm. More details on the working and detection principles of a FE-SEM and the underlying physical principles that lead to SEs, BSEs and characteristic X-ray radiation can be found in literature.^[335]

4.2.2 Transmission electron microscopy

Transmission electron microscopy (TEM) is a technique whereby a beam of electrons with a narrow energy distribution is transmitted through a thin specimen (less than 200 nm thick) and the interaction of the electrons with the specimen is studied. The interactions reveal information about the morphology and chemical composition of the specimen with a sub-nanometer resolution. In this work, TEM was utilized to study the successful fabrication of nanotubes and core/shell nanotubes and investigate the material distribution across these structures. Therefore, TEM and scanning transmission electron microscopy (STEM) images were recorded by the use of a high angular annular dark field and bright field detector. The chemical composition was analyzed by EDX and the material distribution was studied by EDX line scans and EDX mapping. Further, selective area electron diffraction (SAED) analysis was performed on single nanotubes to investigate the crystallinity of the synthesized structure. All TEM measurements were performed on a *Zeiss Libra 200 FE* TEM with an acceleration voltage of 200 kV. EDX was measured with a Thermo/Noran EDX system. Detailed information of the working principles of TEM, EDX, and the underlining physical principles are widely discussed and can be found in literature.^[336]

The TEM samples for single nanotube investigations were prepared on a Quantifoil R 2/2 TEM grid with a Cu 400 mesh and a 12 nm thick holey carbon film (hole size 2 μm , period 4 μm) according to the following procedure. First, a self-supported nanotube array is placed into a small vessel (*e.g.*, 1.5 ml centrifugal vessel) and deionized water is

Experiments and methods

added. Then the vessel is placed into an ultrasonic bath for 2 minutes. Thereafter, a single drop of the solution is dispersed on a TEM grid and dried at ambient condition.

4.2.3 X-ray photoelectron spectroscopy

X-ray photoelectron spectroscopy (XPS) was performed to verify the oxidization state of Sn in ALD prepared tin oxide and Mn in electrochemically synthesized manganese oxide. All XPS measurements were performed using monochromatic Al K α radiation ($h\nu = 1486.7$ eV) produced by a *PHI 10-610* X-ray source in combination with an *Omicron XM1000* monochromator. All spectra were recorded with an *Omicron 7 channel EA125* hemispherical electron analyzer, operating in the constant pass energy mode. Electrons emitted from the specimen were detected at a takeoff angle of 53° with respect to the surface normal for XPS measurements. Measurements on clean polycrystalline silver were used for the calibration of the experimental setup. With the used analyzer settings, the energy resolution of the XPS measurements is 0.6 eV.^[337] More detailed information on XPS can be found in literature.^[338]

4.2.4 Raman spectroscopy and FTIR

The formation of PPy from Py monomer by electrochemical polymerization was characterized by Raman and FTIR spectroscopy. The Raman spectrum was measured on a NTEGRA spectrometer from *NT-MDT*, using a 532 nm laser. Further information about the spectrometer and the underlying principles of Raman spectroscopy can be found elsewhere.^[339,340] The Fourier transform infrared (FTIR) spectrum was recorded on a SE 900 FT-IR ellipsometer from *Sentech* in reflectance. Please refer to literature for more information on FTIR.^[341]

4.2.5 X-ray diffraction spectroscopy

X-ray diffraction analysis was utilized to study the formation and phase of the ALD prepared TiN nanotube array. The X-ray diffraction measurement was performed on a *Siemens D5000* diffractometer, using the Cu K α radiation. The working principles of XRD are widely discussed in literature.^[342]

4.2.6 Electrochemical characterization

All electrochemical measurements were performed on a *Bio-Logic VSP* electrochemical work station in ambient condition. Three-electrode measurements, consisting of a working electrode (WE), counter electrode (CE) and reference electrode (RE), were

Experiments and methods

measured in a homemade cell with a 1 cm² platinum foil CE and a *Metrohm* double junction Ag/AgCl (3 M KCl) RE. This technique was utilized to study the performance of a single electrode (e.g., specific capacitance, cycle stability, impedance spectroscopy). Two-electrode measurements were performed in a Swagelok type cell, as displayed in Figure 4-4, in order to investigate the supercapacitor device performance (e.g., specific energy, specific power, cycling stability, leakage current, impedance spectroscopy). A *Celgard* 3401 separator (25 μm thick microporous monolayer membrane) was used to electrically isolate both electrodes and a 1 M Na₂SO₄ solution served as the electrolyte during the supercapacitor characterization of the MnO₂ and PPy based electrodes. A 1 M KOH electrolyte was prepared for the characterization of C-TiN and TiN nanotube arrays.

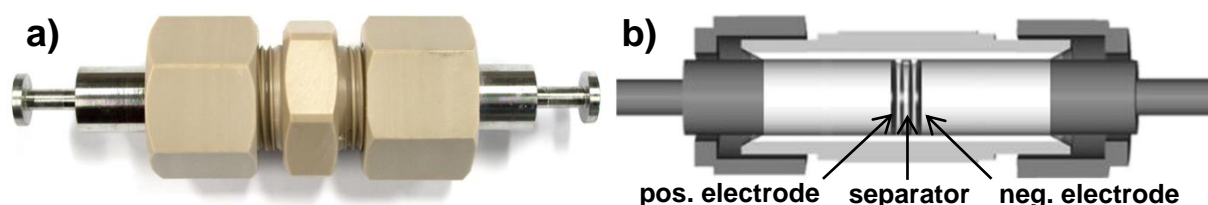


Figure 4-4 | Swagelok type two-electrode measurement setup. (a) Picture of assembled cell; (b) Illustrated cross-section view, displaying the cell arrangement of both electrodes and separator inside the fitting. (Figure redrawn from Ref.^[343])

The prepared electrodes had a diameter of (1.266 ± 0.004) cm and a footprint area of (1.259 ± 0.008) cm². The electrochemical parameters were recorded with a resolution of 50 μV and 760 pA for potentials and currents, respectively.

The investigation of the electrochemical performance of the prepared structures involved cyclic voltammetry (CV), charge/discharge and electrochemical impedance spectroscopy (EIS) measurements. CV measurements and charge/discharge measurements were performed in a fixed potential window at scan rates of 2, 5, 10, 20, 50 and 100 mV s⁻¹ and current densities of 1, 2, 5, 10, 20, 25, 30, 40, and 50 A g⁻¹, respectively. From three-electrode measurements the specific capacitances of the prepared electrodes ($i = [\text{MnO}_2; \text{PPy}; \text{TiN}]$) were calculated from constant current discharge curves according to:

$$c_i = \frac{I\Delta t}{\Delta V m_i} \quad \text{eq. 4-1}$$

with I being the discharge current, Δt the discharge time, ΔV the operating potential window, and m_i the active electrode mass of the respective material. The active electrode mass of the negative (PPy) and positive (MnO₂) electrodes were determined from the total charge (Q) passed during the electrochemical deposition process of the respective active electrode material according to Faraday's law of electrolysis:

Experiments and methods

$$m = \frac{QM}{zF} \quad \text{eq. 4-2}$$

with M being the molar mass of the active electrode material ($M_{MnO_2} = 86.936 \text{ g mol}^{-1}$; $M_{PPy} = 67.09 \text{ g mol}^{-1}$), F the Faraday constant and z the number of transferred electrons per active electrode atom ($z = 2$ for MnO_2 and PPy deposition). A 100 % charge efficiency is assumed. The active electrode masses of PPy and MnO_2 were $(0.108 \pm 0.001) \text{ mg cm}^{-2}$ and $(0.091 \pm 0.001) \text{ mg cm}^{-2}$ during three-electrode investigations. The active electrode mass of the C-TiN and TiN nanotube arrays was determined by a *Mettler-Toledo XP2 microgram balance* (accuracy $0.1 \mu\text{g}$) to ca. $(0.120 \pm 0.001) \text{ mg cm}^{-2}$.

From two-electrode measurements the specific energy (E) and specific power (P) were calculated according to:

$$E = \frac{1}{2} c_{asy} V^2 = \frac{1}{2} \frac{I \Delta t}{\Delta V m_{asy}} V^2 \quad \text{eq. 4-3}$$

$$P = \frac{E}{\Delta t} \quad \text{eq. 4-4}$$

with c_{asy} being the specific capacitance of the two-electrode device, V the voltage after the potential drop and m_{asy} the total active material mass (*i.e.*, combined mass of PPy based negative and MnO_2 based positive electrode is $(0.220 \pm 0.002) \text{ mg cm}^{-2}$). The asymmetric supercapacitor was balanced according to the charges passed across the PPy and MnO_2 based electrode ($q_{PPy} = q_{MnO_2}$) according to:

$$\frac{m_{MnO_2}}{m_{PPy}} = \frac{c_{PPy} \Delta U_{PPy}}{c_{MnO_2} \Delta U_{MnO_2}} \quad \text{eq. 4-5}$$

with $\frac{m_{MnO_2}}{m_{PPy}}$ being the ideal mass ratio of the positive and negative active electrode materials ($\frac{m_{MnO_2}}{m_{PPy}} = 0.56$), c_{PPy/MnO_2} the specific capacitance of the respective electrode material, and $\Delta U_{PPy/MnO_2}$ the respective operating potential window (0.8 V for negative and 0.9 V for positive electrode).

The electrochemical characterization of the individual and asymmetric PPy and MnO_2 core/shell nanotube arrays was performed based on the active material masses that were derived from Faraday's law of electrolysis, as described in eq. 4-2. A contribution of the ALD prepared SnO_2 core to the performance was excluded while calculating the specific capacitance. This approach is in agreement with literature^[3] and is reasonable because the MnO_2 forms a continuous shell around the SnO_2 core. Therefore the SnO_2

Experiments and methods

can rarely contribute to the charge storage capability because the charge is stored near or at the surface of the electrode material through Faradaic reactions.^[3] However, a possible influence of the SnO₂ core on the overall performance of the SnO₂/PPy and SnO₂/MnO₂ core/shell structure is taken into account by measuring the electrochemical performance of a bare SnO₂ nanotube array. The maximum possible contribution of SnO₂ core to the total specific capacitance is calculated according to:

$$c_{Er,i} = \frac{I_{SnO_2} \Delta t_{SnO_2}}{m_i \Delta V} \quad \text{eq. 4-6}$$

with I_{SnO_2} being the discharge current, Δt_{SnO_2} the discharge time, ΔV the potential window and m_i the PPy or MnO₂ mass. The possible contribution is expressed in the errors c_{Er,MnO_2} and $c_{Er,PPy}$. The error bars in Figure 5-13, Figure 5-19a and Figure 5-24b take this correction into account. The absolute values are exclusively presented in Table A3, Table A4, Table A5 and Table A6. In general, the values of c_{Er,MnO_2} and $c_{Er,PPy}$ decrease quickly with increasing current density and the SnO₂ core rarely contributes to the performance during rapid charging and discharging, which is most relevant for supercapacitors.

Further, EIS was utilized to characterize the electrochemical performance of the synthesized structures in more detail. The impedance of the as-prepared electrochemical systems was measured at a steady-state potential by applying a low-amplitude oscillating voltage $V = V_{max} e^{-i\omega t}$ which led to a phase shifted sinusoidal output current $I = I_{max} e^{-i(\omega t + \varphi)}$. The electrochemical impedance $Z(\omega)$ was derived from the relation $Z(\omega) = \frac{V}{I} = |Z(\omega)| e^{-i\varphi} = Z' + iZ''$ with Z' and Z'' being the real part and imaginary part of the impedance, respectively, defined as $|Z'|^2 + |Z''|^2 = |Z|^2$.^[344] EIS was measured at a steady-state potential of 0.1 V for MnO₂ and -0.1 V for PPy based structures with a 10 mV voltage pulse in the frequency range from 100 kHz to 0.05 Hz. The measured impedance data was analyzed and fitted with *ZsimpWin* using a complex nonlinear least-square procedure.

5 Results and discussion

In the following chapter, the results of the fabricated self-supported 3D nanotube arrays are systematically discussed with respect to their structural properties and electrochemical performance. The Section 5.1 presents the fabrication route to synthesize self-supported SnO₂/MnO₂ core/shell nanotube arrays within nano-porous AAO templates and discusses the possible application of the material as a positive electrode in supercapacitor applications. Moreover, the fabrication of the SnO₂ nanotube core is introduced in detail and an innovative approach to fabricate either open-end or closed-end SnO₂ nanotubes is presented. In the Section 5.2, the synthesis and characterization of the SnO₂/PPy core/shell nanotube arrays is discussed. The morphology is investigated and the structure is characterized for a possible application as a negative electrode in supercapacitors. The Section 5.3 reports the obtained results based on an asymmetric supercapacitor device that is built up from the nano-engineered SnO₂/MnO₂ and SnO₂/PPy core/shell nanotube arrays and outlines the synergistic effect that arises from the asymmetric cell design. Thereafter in the Section 5.4, an innovative carbon coating technique is introduced that is capable of coating dense 3D nanostructure arrays. It is shown that a carbon coating on TiN can efficiently improve the long-time cycling stability of the material in supercapacitor applications.

5.1 Positive electrode: Three-dimensional core/shell SnO₂/MnO₂ nanotube array

Manganese dioxide is a highly promising positive electrode material for electrochemical energy storage in supercapacitor applications (see Section 2.4). However, the material suffers from a low internal electrical conductivity (10^{-2} to 10^{-6} Ω^{-1} cm^{-1}),^[64,120,177,178] which results in poor electrode kinetics and material utilization. Therefore, an innovative electrode design was developed, which particularly addresses the challenges associated with MnO₂ and further fulfills the proposed criteria of an ideal 3D supercapacitor electrode (see Section 3.1). The developed electrode design is based on a self-supported SnO₂ nanotube array that serves as a conductive scaffold (typical conductivity of SnO₂ 5 to 74 S cm^{-1}),^[345-347] which is coated in a thin film manner by MnO₂. Figure 5-1 illustrates the fabrication process from nano-porous AAO templates (step i) to either open-end (route a) or closed-end (route b) SnO₂/MnO₂ nanotube arrays by ALD of SnO₂

Results and discussion

(step ii) and conformal electrochemical deposition of MnO_2 onto bare SnO_2 nanotube arrays (step vi or viii). The proposed synthesis strategy facilitates the selective fabrication of open-end (step iii \rightarrow iv) and closed-end (step iii \rightarrow vii) nanotube arrays by precisely controlled AAO template etching and selective nanotube opening. The following section will systematically describe and analyse the morphology and the essential fabrication steps as well as the electrochemical properties of the 3D nanostructured positive supercapacitor electrode.

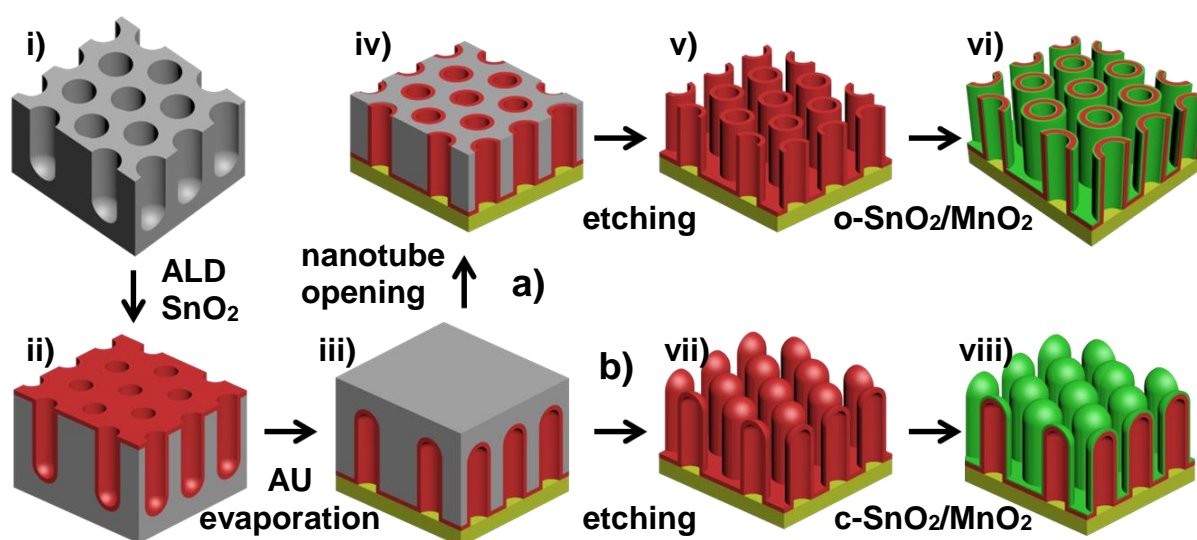


Figure 5-1 | Schematic diagram, illustrating the fabrication processes of (a) open-end $\text{SnO}_2/\text{MnO}_2$ nanotube arrays and (b) closed-end $\text{SnO}_2/\text{MnO}_2$ nanotube arrays. i) Nano-porous AAO template, ii) conformal coating of template with SnO_2 by ALD, iii) turning sample and fabrication of current collector by e-beam evaporation of gold; Process a): iv) partial etching of the nano-porous AAO template and nanotube opening, v) removing of template to gain a highly ordered self-supported SnO_2 nanotube array, vi) electrochemical coating of MnO_2 ; Process b): vii) one-step etching of template, viii) conformal electrochemical deposition of MnO_2 .

5.1.1 SnO_2 nanotube array

The self-supported 3D SnO_2 nanotube arrays are fabricated within nano-porous AAO templates by ALD. The synthesized structure serves as the core material for the $\text{SnO}_2/\text{MnO}_2$ and SnO_2/PPy (Section 5.2) supercapacitor electrodes. The following section discusses the morphology and chemical composition of the nano-tubular structure.

5.1.1.1 Morphology

All SnO₂ nanotube arrays are prepared from AAO templates identically to the one shown in Figure 5-2a. The image displays a typical top view SEM image of an AAO template that is fabricated according to the procedure described in Section 4.1.1. The pore-diameter and the inter-pore distance are 60 and 105 nm, respectively. Figure 5-2b outlines that the utilized conformal ML by ML growth is capable of coating the high aspect ratio material homogeneously by SnO₂. The presented cross-section SEM image is recorded by the use of back scattered electrons and thus contains information about the material distribution within the sample (*i.e.*, Z-contrast). It is shown that the SnO₂ (bright in contrast; $Z_{\text{Sn}} = 50$) is precipitated along the pore walls of the Al₂O₃ template (darker in contrast; $Z_{\text{Al}} = 13$), which indicates that the proposed fabrication strategy is capable of synthesizing nanotube structures with high aspect ratio in the nanometer regime. The structural aspects of the SnO₂ core material, like the variation of the nanotube length and the selective fabrication of open-end and closed-end nanotubes, are analyzed in the following.

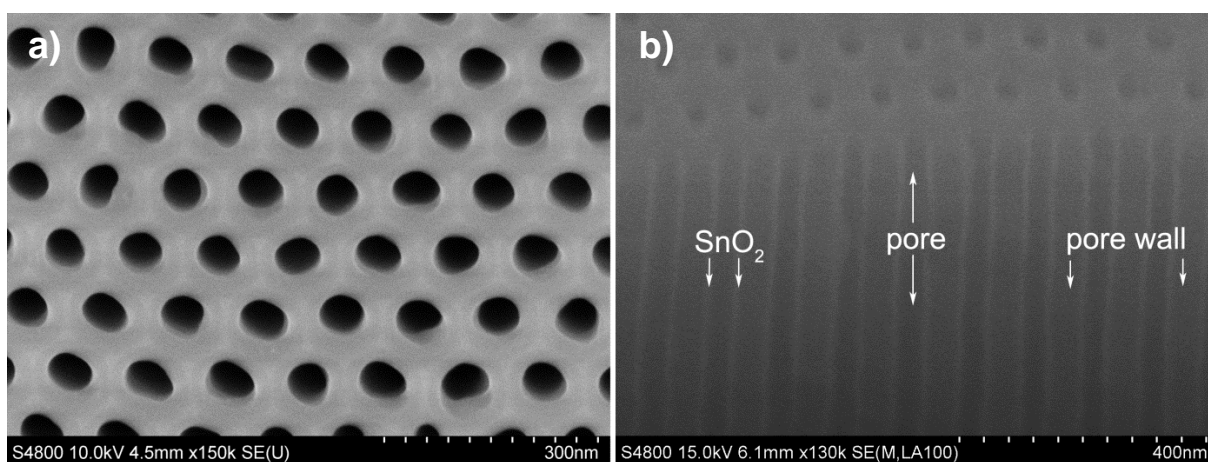


Figure 5-2 | SnO₂ deposited inside the AAO pores. (a) Top view SEM image of the utilized AAO template; (b) Cross-section SEM image of a SnO₂ coated AAO template recorded by the use of back scattered electrons. The obtained material contrast reveals the thin SnO₂ coating (bright) inside the AAO pores.

A major advantage of AAO templates is the high controllability of many structural parameters. Among others, the template thickness (*i.e.*, pore length) can be controlled in a precise manner by adjusting the second anodization time while maintaining the pore diameter and thus change the materials aspect ratio. This feature can be transferred into the ALD prepared SnO₂ nanotube array, as shown in Figure 5-3. The presented cross-section SEM images show the variation of the SnO₂ nanotube length in relationship to

Results and discussion

the second anodization time of the AAO template. It is observed, under the utilized AAO fabrication conditions, that anodization times of 5, 10, and 15 minutes result in nanotube structures with a length of approximately 600, 1200, and 1800 nm, respectively. It should be noted that the synthesized SnO_2 nanotubes are vertically aligned to one another and are self-supported.

The SnO_2 nanotube manufacturing process induces that the top-ends of the prepared nanotubes are initially closed by a spherical half-shell, originating from the AAO barrier layer, see Figure 5-1 step ii. However, it is highly desirable for the final supercapacitor application to gain open-end nanotube structures in order to make not only the outer, but also the inner-tubes surface area available for charge storage. Hence, a novel highly repeatable and well-controllable technique to open the nanotube top-ends is developed. First, the aluminum base material is removed in a CuCl_2 solution, which is followed by a partial pre-etching of the AAO template in a 5 wt. % NaOH solution for 20 minutes to liberate the closed nanotube top-ends (see Figure 5-4a). Subsequently, the liberated closed nanotube top-ends are removed by scratching the samples surface with a sharp scalpel, which results in open-end SnO_2 nanotubes (see Figure 5-4b). In the following open-end and closed-end SnO_2 nanotube arrays will be labeled as o- SnO_2 and c- SnO_2 , respectively.

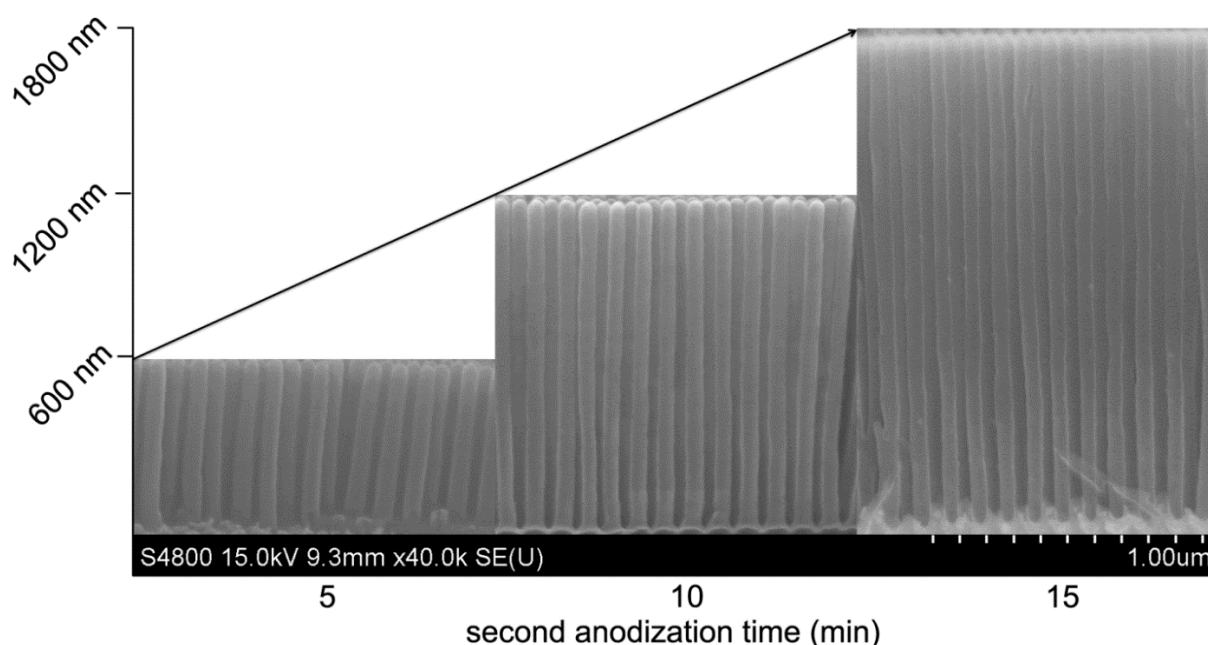


Figure 5-3 | Cross-section SEM analysis of the SnO_2 nanotube length in relation to the second anodization time of the AAO template (*i.e.*, thickness of the template).^[13]

Results and discussion

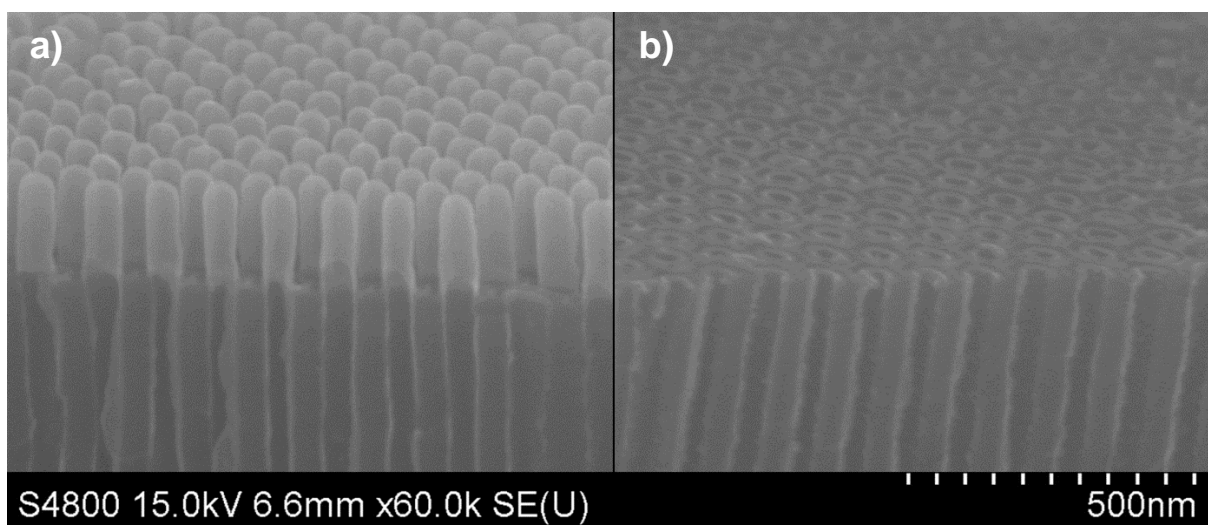


Figure 5-4 | Cross-section SEM investigation of the SnO₂ nanotube opening. (a) Partially etched nanotube array, showing the liberated closed top-ends before the removal; (b) Open nanotube array after removing the closed top-ends by scratching the surface with a sharp scalpel.

Three-dimensional SnO₂ nanotube arrays are constructed after etching the entire AAO template in 5 wt. % NaOH for 120 minutes, either directly to obtain c-SnO₂ nanotubes or by the proposed pre-etching and removal process to gain o-SnO₂ nanotubes. Figure 5-5 displays both self-supported c-SnO₂ and o-SnO₂ nanotube arrays. The presented top view SEM images clearly show that the proposed fabrication process is capable of selectively fabricating c-SnO₂ and o-SnO₂ nanotubes, as to realize route a) and route b) in Figure 5-1. The insets in Figure 5-5 show a large magnification top view SEM image of

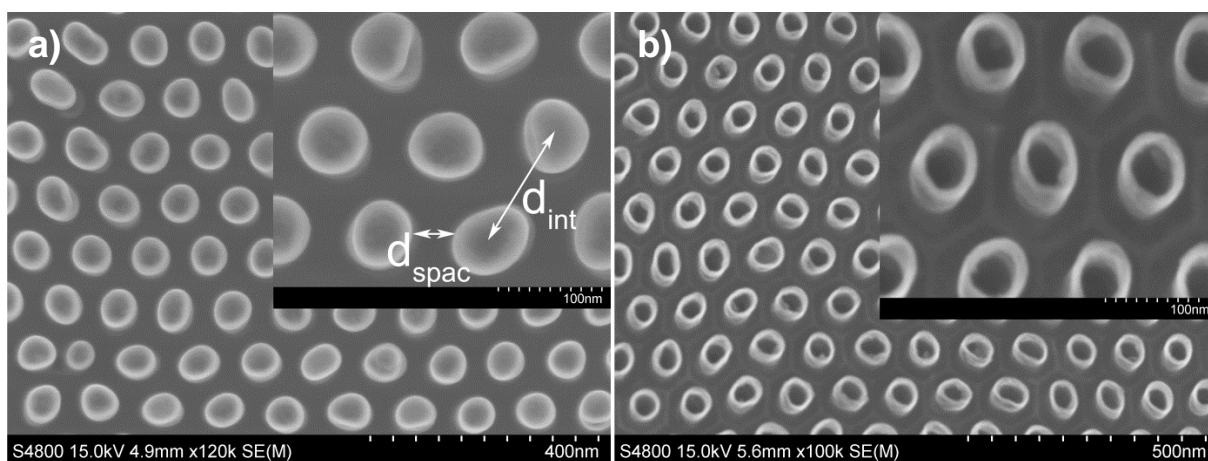


Figure 5-5 | Top view SEM images of the self-supported (a) closed-end SnO₂ nanotube array and (b) open-end nanotube array. The insets show a large magnification of one unit cell with an inter-tube distance $d_{int} = 105$ nm and inter-tube spacing $d_{spac} = 45$ nm.^[13]

Results and discussion

one unit cell. The images reveal that the outer-tube diameter, inter-tube spacing and inter-tube distance of adjacent nanotubes are $d = 60$ nm, $d_{\text{spac}} = 45$ nm, and $d_{\text{int}} = 105$ nm, respectively, and thus are inherited from the AAO template (Figure 5-2a). The wall thickness and the inner-tube diameter of the SnO₂ nanotubes are investigated by TEM measurements. Figure 5-6a displays a TEM image of a single SnO₂ nanotube and reveals a wall thickness of about 8 nm after 1000 ALD cycles, which is evaluated from the contrast profile in Figure 5-6b (using a similar method as described by Perez et al.^[348]). The wall thickness depends on the total ALD cycle number and the growth rate, which is estimated to be approximately 0.08 Å per cycle. It is found that 8 nm is an optimal adjustment of the wall thickness to maximize the overall inner surface area (*i.e.*, enlarge the inner-tube diameter) and, at the same time, keep high mechanical stability of the SnO₂ nanotubes (*i.e.*, thicken the tube walls). Therefore, the synthesized nanotubes with an outer-tube diameter of about 60 nm, inter-tube distance of 105 nm and tube-wall thickness of 8 nm, exhibit an inner-tube diameter and inter-tube spacing of about 44 and 45 nm, respectively. Hence, the synthesized structures have sufficient inner- and outer-tube spaces for the next step of the conformal MnO₂ coating. SAED analysis of the SnO₂ nanotube indicates that the ALD prepared nanotube is of amorphous nature, as presented in Figure 5-6c.

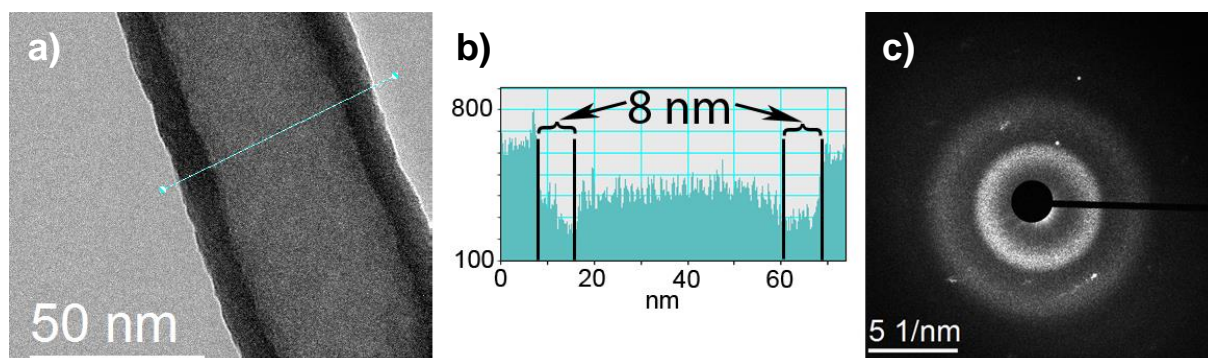


Figure 5-6 | TEM investigation of a SnO₂ nanotube. (a) TEM image of a single SnO₂ nanotube, showing the hollow nature of the nanotube; (b) Contrast profile across the nanotube reveals a wall thickness of approx. 8 nm;^[13] (c) SAED of the presented SnO₂ nanotube.

5.1.1.2 Chemical composition

The chemical composition of the ALD prepared tin oxide nanotube core is analyzed by XPS measurements according to the procedure described in Section 4.2.3. Figure 5-7 shows the Sn 3d core level spectrum of tin with a typical spin orbit splitting of 8.4 eV. The binding energy peaks of the Sn 3d_{5/2} and Sn 3d_{3/2} orbitals are located at 487.3 eV and

Results and discussion

495.7 eV, respectively. These results are in agreement with previously reported binding energy peaks of Sn^{4+} and verify the formation of SnO_2 .^[349]

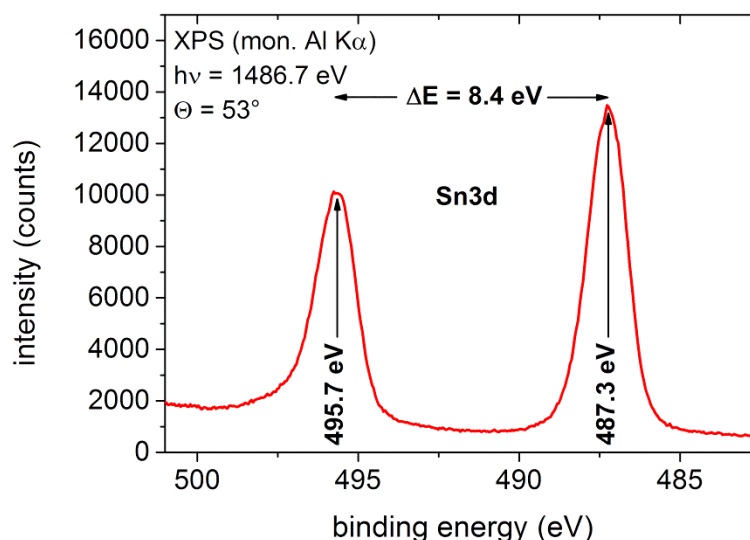


Figure 5-7 | XPS spectrum of the Sn 3d orbital of the ALD prepared SnO_2 nanotube array, showing a spin orbit splitting of 8.4 eV and binding energies of 487.3 eV and 495.7 eV for $\text{Sn } 3d_{5/2}$ and $\text{Sn } 3d_{3/2}$ orbitals, respectively.^[13]

5.1.2 $\text{SnO}_2/\text{MnO}_2$ core/shell nanotube array

5.1.2.1 Morphology

The self-supported 3D $\text{SnO}_2/\text{MnO}_2$ core/shell nanotube array is fabricated by potentiostatic electrochemical deposition of MnO_2 onto a bare SnO_2 nanotube array from a solution containing 0.1 M $\text{Mn}(\text{Ac})_2$ at 1 V vs. Ag/AgCl . The top view SEM image in Figure 5-8a outlines that the open-end nanotube nature could be maintained after the

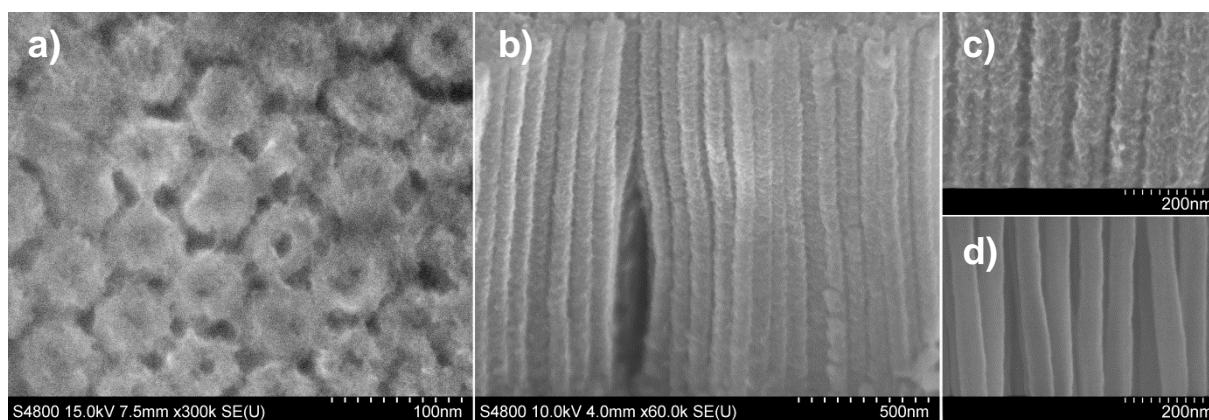


Figure 5-8 | SEM investigation of the o- $\text{SnO}_2/\text{MnO}_2$ nanotube array. (a) Top view, (b) cross-section and (c) large magnification of cross-section; (d) Cross-section of uncoated SnO_2 nanotube array at same magnification as (c) for comparison.^[13]

Results and discussion

electrochemical deposition of MnO_2 onto an o-SnO_2 nanotube array. The cross-section SEM images, as shown in Figure 5-8b and c, indicate the good conformal coating of the SnO_2 core by the MnO_2 shell along the entire nanotube and reveal an average outer nanotube diameter of (72 ± 7) nm. The difference in surface morphology between the coated (Figure 5-8c) and uncoated SnO_2 nanotubes (Figure 5-8d) can clearly be seen. The coated nanotubes exhibit much rougher surfaces compared to the uncoated nanotubes, which is a typical result of electrochemically deposited MnO_2 .

These results are approved by structural and chemical investigations obtained from STEM, EDX mapping and EDX line scan measurements, which are performed on a single $\text{SnO}_2/\text{MnO}_2$ core/shell nanotube. The dark field TEM image in Figure 5-9 shows that the MnO_2 shell is coated conformally on the SnO_2 core with a thickness of approximately 10 to 20 nm. This result is supported by the respective EDX mapping and EDX line scan of the Mn K line, which is recorded across the transverse nanotube axis, showing both a continuous distribution of manganese along the surface of the SnO_2 nanotube. Furthermore, the elemental distribution of Sn confirms the hollow nanotube nature of the core material. The recorded EDX line scan of the Sn L line shows two distinct peaks located at the wall positions of the nanotube. This result is confirmed by EDX mapping, which displays a more intense Sn L signal at the wall positions compared to the hollow nanotube center. The obtained O K signal arises from the oxygen present

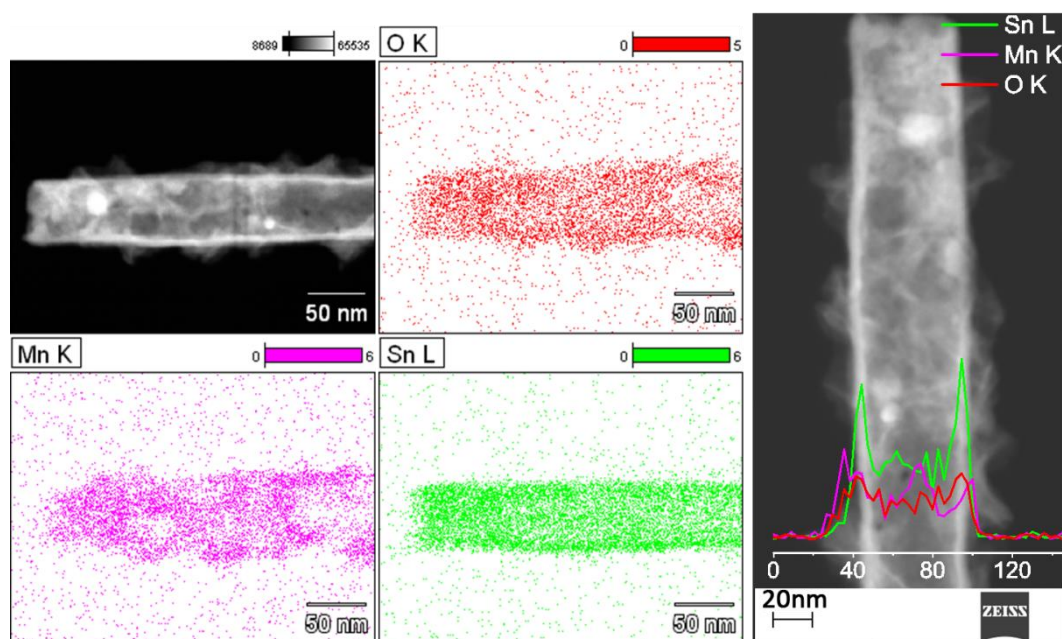


Figure 5-9 | Investigation of the elemental distribution of Mn, Sn and O across a single $\text{SnO}_2/\text{MnO}_2$ core/shell nanotube by EDX mapping and EDX line scan performed in TEM.^[13]

Results and discussion

in MnO_2 and SnO_2 and is homogeneously distributed across the core and shell of the structure. The obtained results from STEM and SEM underline that dense arrays of self-supported 3D core/shell nanostructures are successfully synthesized by the proposed template assisted fabrication strategy.

However, such advanced conformal coatings on a three-dimensional nanostructure array require the use of optimized fabrication conditions (see experimental 4.1.4). In particular, the total amount of material that is being deposited needs to be controlled precisely (*i.e.*, precise control of current flow during electrochemical deposition). An optimal window of 115 to 230 mC cm^{-2} flown charge during the MnO_2 precipitation is determined for SnO_2 nanotube arrays with a length of approx. 1800 nm. It should be noted that an excessive deposition of MnO_2 leads to a non-conformal coating and thick layer growth, as shown in Figure 5-10. Such structures are not desirable for supercapacitor applications because the beneficial effects that arise from the 3D core/shell structure are suppressed and fast electron kinetics and a sufficient active material utilization is hindered.

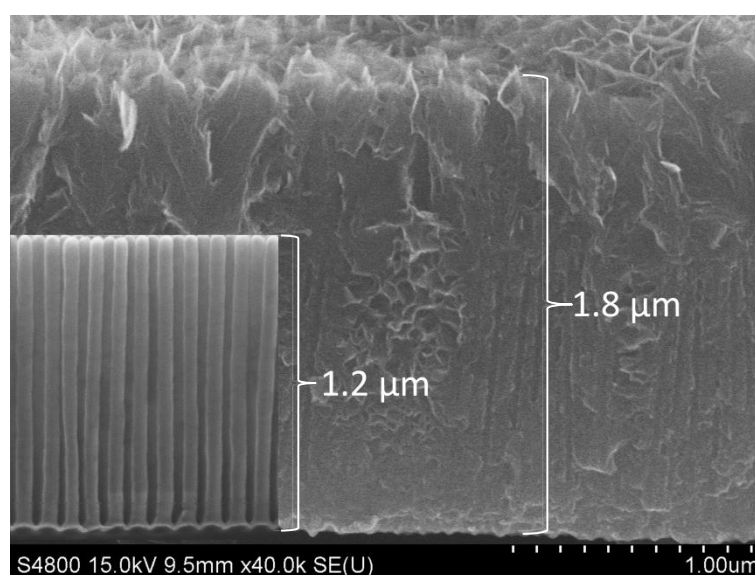


Figure 5-10 | Cross-section SEM image, displaying that an excessive deposition of MnO_2 is leading to a non-conformal coating of the SnO_2 core material. The inset shows the original length of the SnO_2 nanotube array before coating.^[13]

5.1.2.2 Chemical composition

The chemical composition of the electrochemically deposited manganese oxide nanotube shell is analyzed by XPS measurements according to the procedure described in Section 4.2.3. Figure 5-11 shows the Mn 2p core level spectrum of manganese with a typical spin orbit splitting of 11.6 eV. The binding energy peaks of the Mn $2p_{3/2}$ and Mn $2p_{1/2}$ orbitals are located at 653.8 eV and 642.2 eV, respectively. These results are in

Results and discussion

agreement with previously reported binding energy peaks of Mn^{4+} and verify the formation of MnO_2 .^[350]

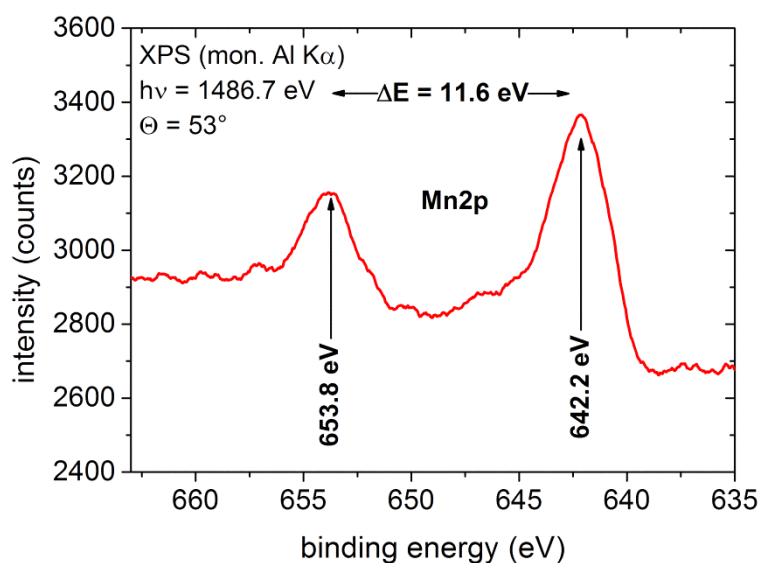


Figure 5-11 | XPS spectrum of the Mn 2p orbital of the electrochemical deposited MnO_2 nanotube shell, showing a spin orbit splitting of 11.6 eV and binding energies of 653.8 eV and 642.2 eV for Mn $2p_{3/2}$ and Mn $2p_{1/2}$ orbitals, respectively.^[13]

5.1.3 Electrochemical performance

The electrochemical performance of the self-supported 3D $\text{SnO}_2/\text{MnO}_2$ core/shell nanotube array is analyzed in a three-electrode configuration. The measuring setup included a platinum foil as a CE, an Ag/AgCl RE and a water-based electrolyte containing 1.0 M Na_2SO_4 . Figure 5-12a displays the cyclic voltammetry (CV) curves obtained from an as-prepared o- $\text{SnO}_2/\text{MnO}_2$ nanotube array. All CV scans are performed in a potential range from 0 to 0.9 V vs. Ag/AgCl at scan rates of 2, 5, 10, 20, and 50 mV s^{-1} and show typical scaling behavior of the current with increasing scan rate. The shapes of the CV curves reassemble the expected shape for pseudocapacitive charge storage in MnO_2 and indicate good capacitance behavior of the synthesized material. Further, galvanostatic charge/discharge curves are recorded at different current densities to evaluate the specific capacitance and rate capability, as shown in Figure 5-12b. Thereby, the specific capacitance is derived from the gradient of the discharge curve according to the procedure described in Section 4.2.6.

Results and discussion

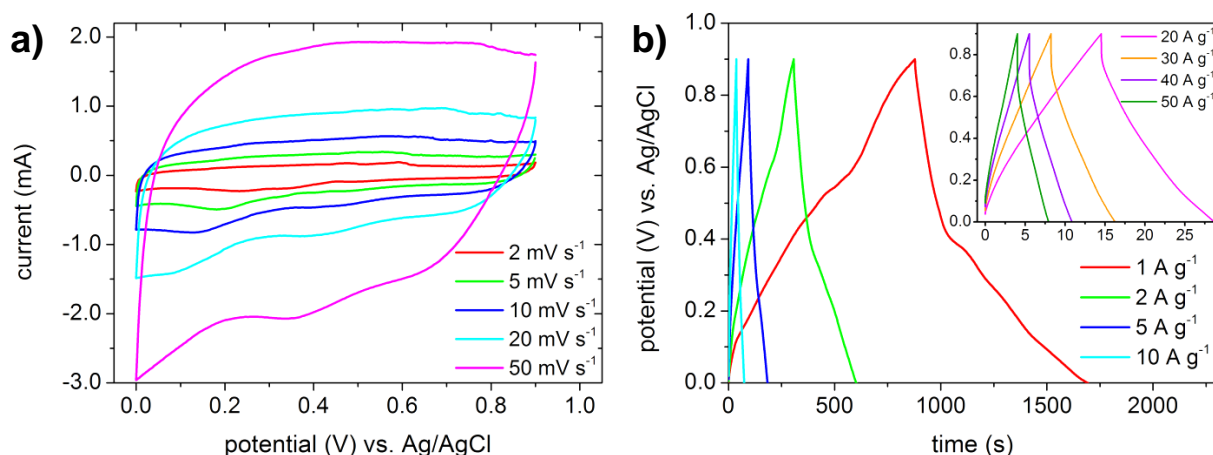


Figure 5-12 | Electrochemical performance of the o-SnO₂/MnO₂ core/shell nanotube array with a nanotube length of 1.8 μm . (a) CV curves at different current densities; (b) charge/discharge profiles at different current densities.^[13]

Figure 5-13a displays the calculated specific capacitance values derived for different current densities and compares the obtained results of o-SnO₂/MnO₂ and c-SnO₂/MnO₂ core/shell nanotube arrays with same length (1.8 μm) and same mass loading. The performance is based on the MnO₂ mass loading. A possible contribution of the SnO₂ core is taken into account by the presented error bars according to eq. 4-6, as discussed in Section 4.2.6. All values, including uncertainty values, are presented in

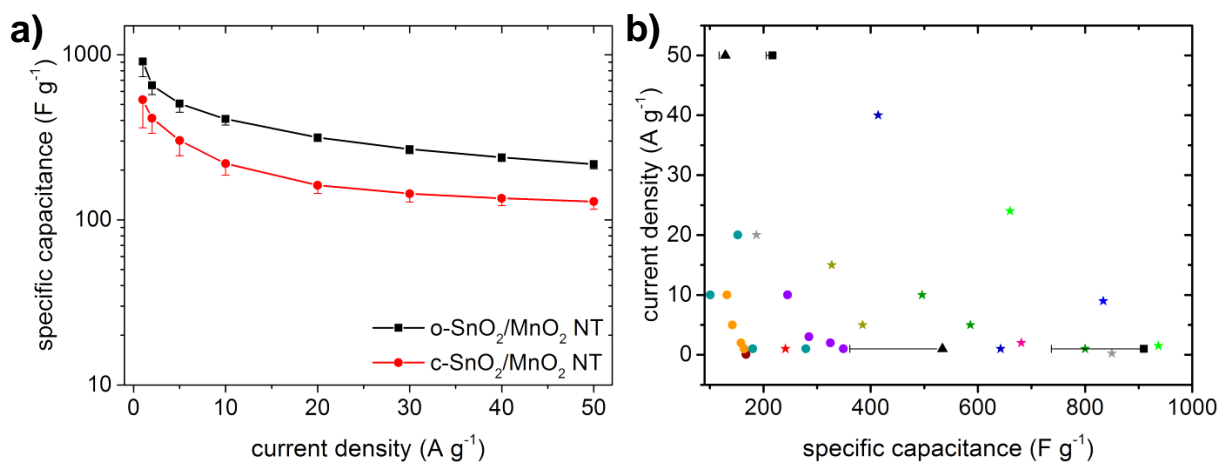


Figure 5-13 | Performance of the o-SnO₂/MnO₂ and c-SnO₂/MnO₂ nanotube arrays. (a) Rate capability and structure comparison; (b) Literature comparison of various MnO₂ based structures. Star-shape core/shell structures and circle bare MnO₂ structures.

o-SnO₂/MnO₂,
 c-SnO₂/MnO₂,
 MnO₂/Mn,^[117]
 MnO₂/TiN,^[118]
 MnO₂/TiN,^[119]
 MnO₂/SnO₂,^[120]
 MnO₂/Zn₂SnO₄,^[121]
 MnO₂/Au,^[122]
 MnO₂/Ni,^[123]
 MnO₂/aMEGO,^[124]
 MnO₂ NT,^[115]
 MnO₂ NW,^[24]
 MnO₂ NW,^[110]
 MnO₂/CNT^[130]

Results and discussion

Table A3. The diagram in Figure 5-13a shows that the o-SnO₂/MnO₂ nanotube array exhibits an excellent maximum specific capacitance of 910 F g⁻¹ at 1 A g⁻¹ and remains a high specific capacitance of 217 F g⁻¹ at 50 A g⁻¹. This result exceeds the performance of nanostructured electrodes that purely consist of MnO₂ and importantly, it is among the highest reported values of MnO₂ based core/shell nanostructures, as outlined in the literature comparison in Figure 5-13b and in Section 2.4. This statement is even true when considering a possible contribution of the SnO₂ core. Beyond that the prepared core/shell structure exhibits a high areal capacitance of up to 0.092 F cm⁻² at 1 A g⁻¹ and 0.022 F cm⁻² at 50 A g⁻¹, which is higher than reported values of other core/shell structures.^[118] In addition the reported structure obtains a high volumetric capacitance of 511 F cm⁻³ at 1 A g⁻¹ and 122 F cm⁻³ at 50 A g⁻¹. Interestingly, the electrochemical performance of the c-SnO₂/MnO₂ nanotube array remains behind the values of the o-SnO₂/MnO₂ nanotube array. The c-SnO₂/MnO₂ nanotube array exhibits a specific capacitance of 534 F g⁻¹ at 1 A g⁻¹ and remains 129 F g⁻¹ at 50 A g⁻¹. It is believed that the difference in performance can be attributed to the lower available surface area of c-SnO₂/MnO₂ electrodes compared to o-SnO₂/MnO₂ electrodes and a longer ion diffusion path length. These results outline that a highly porous open-end nanotube structure as a core material in supercapacitor electrodes is superior to core materials based on closed-end nanotubes and nanowires.

The long-time cycling stability is a crucial aspect in supercapacitor applications. Therefore, the electrochemical evolution of the o-SnO₂/MnO₂ nanotube array was investigated during 2000 consecutive charging and discharging cycles at 5 A g⁻¹, as

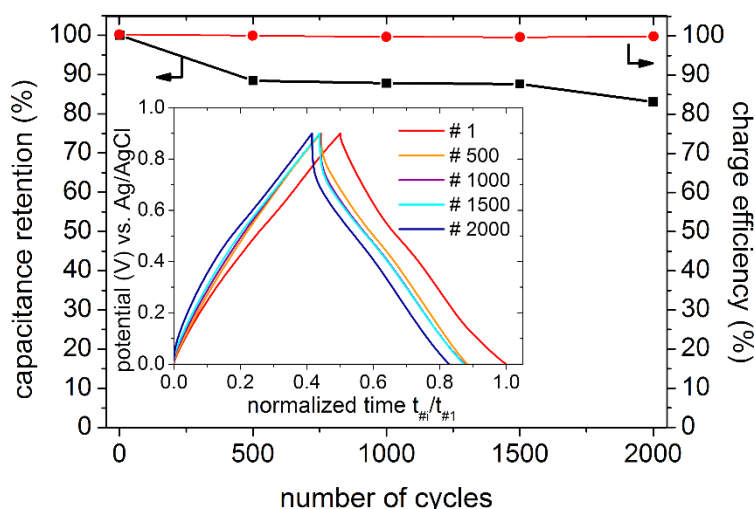


Figure 5-14 | Long-time cycling stability and charge efficiency of the o-SnO₂/MnO₂ core/shell nanotube array recorded at 5 A g⁻¹. The inset presents the respective charge/discharge curves.^[13]

Results and discussion

presented in Figure 5-14. The measurement reveals that the electrode remains around 82 % of its initial capacitance after 2000 cycles. The respective charge/discharge curves in the inset of Figure 5-14 confirm the results (potential plotted against normalized time $t_{\#i}/t_{\#1}$ with $i = [1; 500; 1000; 1500; 2000]$). Further, the o-SnO₂/MnO₂ nanotube array exhibits a high charge efficiency (defined as $t_{\text{dis}}/t_{\text{charge}}$) of about 99 % throughout the entire stability measurement. These results demonstrate that the o-SnO₂/MnO₂ nanotube array is capable of accomplishing large numbers of charge/discharge cycles and hence, are ideal candidates for applications that require long-time performance stability.

The electrochemical performance of the o-SnO₂/MnO₂ core/shell nanotube array is further investigated by electrochemical impedance spectroscopy (EIS). The Nyquist plot in Figure 5-15a presents the imaginary vs. real component of the total impedance at various frequencies for the measured data and fitted curves of the materials impedance. The impedance plot is composed of two areas, a steep line in the low-frequency region and a compressed semi-circle in the high-frequency region. The almost vertical line in the low-frequency region indicates the good capacitance behavior of the electrode material due to fast and reversible reactions occurring at or near the surface of the electrode.^[13] The semi-circle in the high-frequency region provides evidence for the electrodes equivalent series resistance (R_s) at the low x-axis interception and interfacial charge-transfer resistance (R_{CT}) at the interpolated interception at (R_s+R_{CT}).^[351] Thereby, the equivalent series resistance is influenced by the contact resistance between the electrode and current collector, intrinsic resistance of the electrode material, and ionic resistance of the electrolyte.^[54,352] Whereas the interfacial charge-transfer resistance

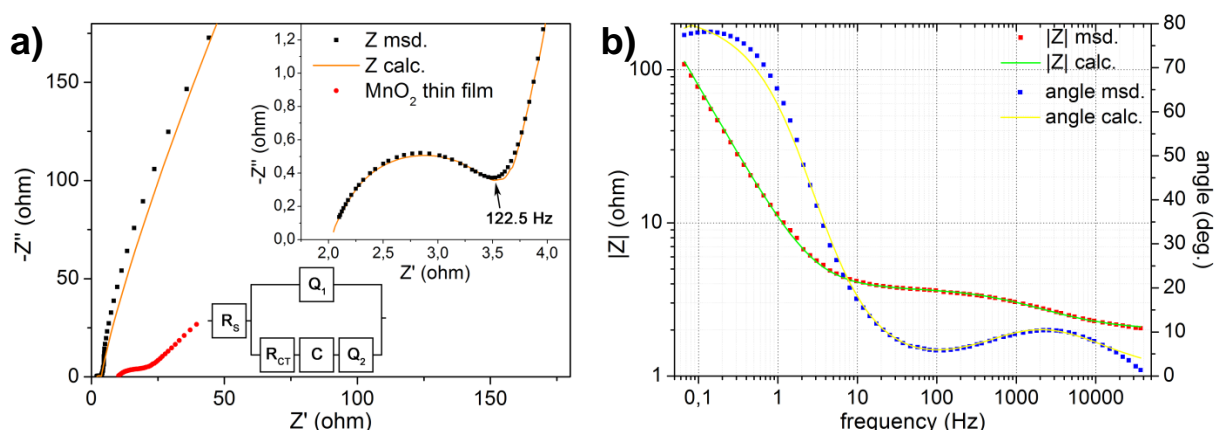


Figure 5-15 | Electrochemical impedance spectroscopy of the SnO₂/MnO₂ core/shell nanotube array. (a) Nyquist plot and (b) Bode plot displayed in a frequency range from 50 kHz to 50 mHz (dots: measured values; lines: fit according to displayed equivalent circuit model).^[13]

Results and discussion

arises from the Faradaic charge storage reaction that occurs in the pseudocapacitive material. The R_S and R_{CT} values are derived from fitting results of the presented equivalent circuit (Q: constant phase element, R: ohmic resistance, C: capacitance),^[353] which represents pseudocapacitive charge storage and are $R_S = (2.02 \pm 0.02) \Omega$ and $R_{CT} = (1.5 \pm 0.1) \Omega$. In this model, the double-layer capacitance and the Warburg impedance of a Randles circuit are replaced by two constant phase elements to account for the diffusion process of the ions at the electrolyte/electrode interface, porosity and nature of the electrode, which is in agreement with other reports.^[103,354] A comparison with reported literature values reveals that the measured values of the o-SnO₂/MnO₂ structure are lower or comparable to other core/shell structures.^[119,121,355] In contrast, pure MnO₂ based electrodes generally exhibit higher resistance values due to the high internal resistance of MnO₂ (e.g., 13.7 $\Omega \text{ cm}^{-2}$ for birnessite MnO₂^[356]).^[105,357] As an example, the electrochemical impedance spectrum obtained from a two-dimensional MnO₂ layer on a gold substrate with the same mass loading as the o-SnO₂/MnO₂ structure shows remarkably higher equivalent series resistance $R_S = (10.01 \pm 0.02) \Omega$ compared to the three-dimensional core/shell structure, see Figure 5-15a. The good electric and ionic conductivity of the core/shell structure is further reflected by the high knee-frequency, which divides the high- and low-frequency part of the impedance plot. It represents the critical frequency at which a supercapacitor begins to exhibit capacitive behavior and is an indication of the power capability of a supercapacitor.^[358] This value is determined from the Nyquist plot to be 122.5 Hz and assigns the supercapacitor electrode capacitive behavior up to high frequencies and thus a good power capability. The Bode plot in Figure 5-15b describes the frequency dependency of the phase angle and the absolute value of the impedance. The supercapacitor response frequency f_0 , defining the point where resistive and capacitive impedance are equal at a phase angle of 45°, is determined to be 2.4 Hz and the corresponding time constant $\tau_o = \frac{1}{f_0}$ is 417 ms (i.e., τ_o represents the minimum time needed to discharge all the energy from the device with an efficiency greater than 50 %^[359]). This rapid frequency response of the o-SnO₂/MnO₂ structure can be attributed to the unique three-dimensional nano-tubular electrode structure, which provides a high surface area and an enhanced charge carrier transport rate. The maximum phase angle of the supercapacitor electrode is 78° at a frequency of 0.12 Hz and is in the range of the theoretical value of 90° for an ideal capacitor (i.e., an ohmic resistance and capacitance in series^[360]). These results obtained from EIS indicate that the o-SnO₂/MnO₂ core/shell structure is a favorable

electrode structure to enhance the electrochemical performance of supercapacitors because of the fast electron transport through the electrodes matrix (*i.e.*, core material) and the short ion diffusion length in the thin shell, making three-dimensional engineered high aspect ratio nanostructures beneficial morphologies for supercapacitor applications.

5.2 Negative electrode: Three-dimensional core/shell SnO₂/PPy nanotube array

The fabrication of an asymmetric supercapacitor requires the integration of a positive and negative electrode with complementary active materials into one device. As shown in the previous section, the self-supported SnO₂/MnO₂ core/shell nanotube array exhibit strong electrochemical performance with respect to supercapacitor applications and represent a good positive electrode. As the choice of active materials for the negative electrode in combination with MnO₂ is to the present limited (see Section 2.5), new materials need to be developed and investigated. In the following section, the synthesis process and electrochemical performance of a self-supported SnO₂/PPy core/shell nanotube array is described for the tailored use as a negative electrode in combination with the synthesized MnO₂ based positive electrode.

5.2.1 Structural investigation

The PPy based negative electrode is fabricated by a procedure similar to the one utilized for the synthesis of the o-SnO₂/MnO₂ core/shell nanotube array, as described in Figure 5-1. The open-end SnO₂ nanotube array served as the fundamental substructure (see Section 5.1.1 for details) and is coated by potentiostatic electrochemical polymerization with PPy to form a core/shell structure. The polymerization on the surface of the SnO₂ nanotube array is performed at 0.8 V vs. Ag/AgCl from an aqueous solution containing 0.1 M pyrrole monomer (98 %) and 0.2 M oxalic acid. The morphology of the self-supported SnO₂/PPy core/shell nanotube array is investigated by SEM, STEM and EDX line scans. Figure 5-16a shows SEM images of the uncoated self-supported SnO₂ nanotube array in both top and cross-section view. The nanotube core material is well-aligned, of regular nature and exhibits a porous structure for the deposition of the PPy shell. The diameter and length of the SnO₂ nanotubes are 60 nm and 1.8 μm, respectively. The bare SnO₂ nanotubes are coated on the entire surface with PPy by electrochemical polymerization of Py monomer in a thin film and porous manner. The SEM images in Figure 5-16b and c and the STEM image in the inset of Figure 5-16c

Results and discussion

clearly show the conformal coating of PPy on the SnO₂ surface. It is noteworthy that the open-end nanotube structure is maintained after the coating process and thus ensures good electrode kinetics and efficient material utilization. The difference in morphology between the uncoated SnO₂ nanotube and the coated SnO₂/PPy nanotube can clearly be seen in Figure 5-16d. The bare SnO₂ nanotubes exhibit a smooth surface whereas in contrast the surface of the PPy coated nanotubes is rougher and the separation distance between two adjacent nanotubes has been reduced. In some cases the gap between two neighboring SnO₂ nanotubes is filled entirely by PPy. The formation of the core/shell structure and the material distribution is further verified by STEM and EDX line scans. Figure 5-16e and f show dark field STEM images of two parallel SnO₂/PPy nanotubes

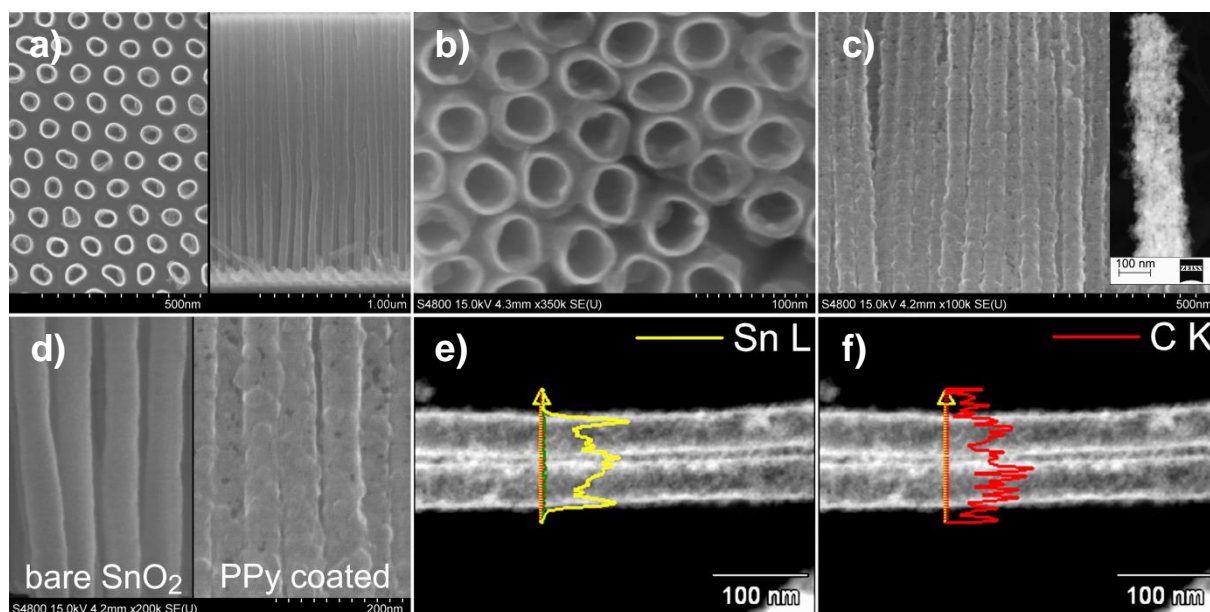


Figure 5-16 | Structural investigation of the self-supported 3D SnO₂/PPy nanotube array. a) Top view and cross-section view of bare SnO₂ nanotube array. b) Top view SEM image of a PPy covered SnO₂ nanotube array, showing the highly porous nature of the core/shell electrode. c) Cross-section SEM view of a PPy covered nanotube array and TEM image of a single SnO₂/PPy nanotube (inset), indicating the highly conformal coating. d) Cross-section SEM image of a bare SnO₂ nanotube array compared to a PPy coated nanotube array. e-f) TEM images of two parallel SnO₂/PPy nanotubes with EDX line scans, showing the material distribution across the tubular structure. e) Sn L line scan profile shows signal peaks located at the wall positions of the SnO₂ nanotubes, proving the nano-tubular nature of SnO₂. f) C K spectrum, indicating an increased carbon content across the nanotubes, which originates from the PPy shell.^[15]

Results and discussion

with EDX line scan profiles recorded across the tubular structures. The spectrum of the Sn L line exhibits signal peaks that are located at the wall positions of the SnO₂ nanotube core and the C K spectrum shows an increased carbon content across the nanotubes, which originates from the carbon in the organic PPy material. These results prove that the SnO₂/PPy nanotube is of hollow nature and indicate that the tubular structure is coated by PPy.

5.2.2 FTIR and Raman spectroscopy

The formation of PPy on the SnO₂ nanotube core by electrochemical polymerization is, in addition to EDX line scans, verified by FTIR and Raman spectroscopy. Figure 5-17a shows the recorded FTIR spectrum of the electrochemically polymerized PPy on the SnO₂ nanotube array with its characteristic features. The arising bands at 923, 1047, 1315, and 1567 cm⁻¹ can be assigned to C-H out of plane vibrations, C-H in plane vibrations, C-N stretching vibration, and C=C vibrations of PPy, respectively.^[361,362] The peak at 1688 cm⁻¹ can be assigned to C=O stretching that results from incorporated oxalic acid ions during the electrochemical polymerization process.^[363] The measured Raman spectrum in Figure 5-17b supports the FTIR measurements and verifies the formation of PPy on the three-dimensional SnO₂ nanotube array. The strong peak at 1560 cm⁻¹ arises from C=C stretching of PPy and the peaks at 1381 cm⁻¹ and 1330 cm⁻¹ are associated with the antisymmetric C-N stretching of PPy.^[364,365] The two peaks at 1051 cm⁻¹ and 967 cm⁻¹ arise from symmetrical C-H in plane bending of the polar

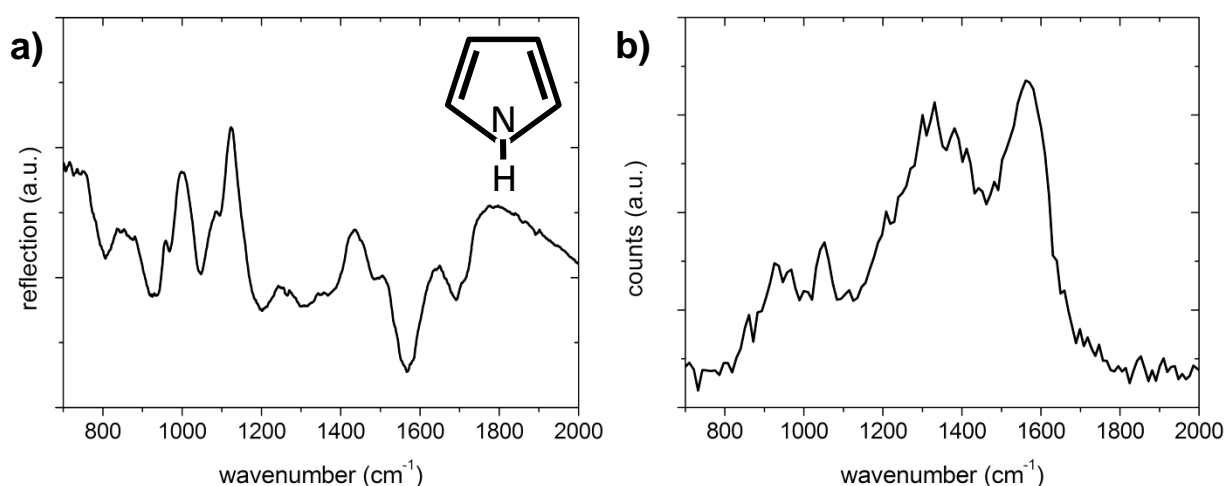


Figure 5-17 | FTIR spectrum (a) and Raman spectrum (b) of the electrochemically polymerized PPy on a SnO₂ nanotube array, showing the characteristic features of PPy. The schematic inset in (a) illustrates the molecular structure of a pyrrole monomer.

Results and discussion

structure of PPy whereas the peak at 929 cm^{-1} is assigned to C-H out of plane deformation of the bipolar structure of PPy.^[364-366] The shoulder around 1655 cm^{-1} is associated with the characteristic C=O stretching from the incorporated oxalic acid ions.^[367]

5.2.3 Electrochemical performance

The 3D SnO_2/PPy core/shell nanotube array is characterized electrochemically for the tailored use as a suitable negative electrode in asymmetric supercapacitor devices by CV and galvanostatic charge/discharge measurements. The performance was studied within a potential window ranging from -0.8 to 0 V vs. Ag/AgCl, which is a desired complementary voltage window to MnO_2 . The electrochemical performance is analyzed in a three-electrode configuration, using a platinum foil as a CE, an Ag/AgCl RE and a neutral water-based electrolyte containing $1.0\text{ M Na}_2\text{SO}_4$. Figure 5-18a displays the recorded CV curves of the SnO_2/PPy nanotube array at scan rates of $2, 5, 10, 20,$ and 50 mV s^{-1} . The shapes of the curves reassemble the desired shape for charge storage in pseudocapacitive materials to a great extent and show the expected scaling behavior of the current as the scan rate is increased, indicating good capacitance behavior of the synthesized material. The charge/discharge curves in Figure 5-18b are measured at various current densities between 1 and 50 A g^{-1} and show a nearly linear time-dependent change in potential at a constant current (*i.e.*, symmetric triangular shape of the galvanostatic charge/discharge profiles), as required for charge storage in supercapacitors.

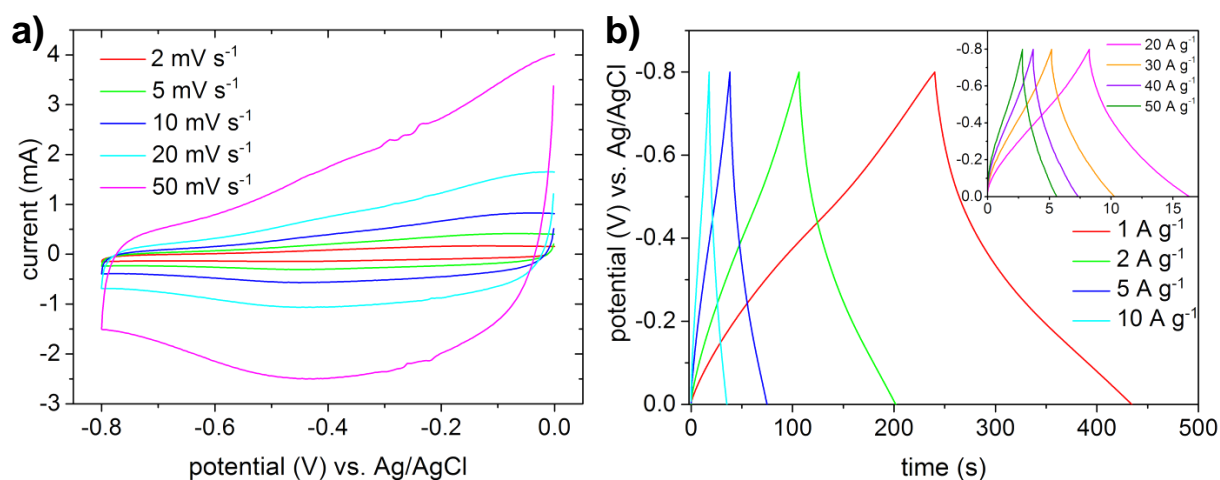


Figure 5-18 | Electrochemical performance of the SnO_2/PPy nanotube array. (a) CV curves at different scan rates; (b) Charge/discharge curves at various current densities.

Results and discussion

The specific capacitance of the PPy based electrode is calculated from the gradient of the discharge curve, as described in eq. 4-1, and the obtained values are displayed in Figure 5-19. The performance is based on the PPy mass loading. A possible contribution of the SnO₂ core is taken into account by the presented error bars according to eq. 4-6, as discussed in Section 4.2.6. All values are presented in Table A4. The electrode exhibits a maximum of 260 F g⁻¹ at 1 A g⁻¹ and remains remarkable 73 % of the initial capacitance at 50 A g⁻¹. This measure assigns the SnO₂/PPy core/shell structure an excellent rate capability, which could be attributed to the large surface area and the good electronic transport properties throughout the entire electrode. Importantly, the obtained performance is superior to carbon based materials which only exhibit up to approx. 120 F g⁻¹ in neutral electrolytes (see Section 2.5), making this material a promising candidate as a negative electrode in asymmetric MnO₂ based supercapacitors. Long-time cycling stability measurements show that the electrodes capacitance retention is about 79 % after 2000 consecutive charge/discharge cycles (Figure 5-19b). The respective charge/discharge curves in the inset confirm the results (potential plotted against normalized time $t_{\#i}/t_{\#1}$ with $i = [1; 500; 1000; 1500; 2000]$). Initially the electrode undergoes a decline in specific capacitance, which is in accordance with the moderate charge efficiency (defined as $t_{\text{dis}}/t_{\text{charge}}$). Thereafter, the capacitance retention curves flattens out and the charge efficiency improves to 98 %, as expected for supercapacitor charge storage. In summary, the SnO₂/PPy core/shell electrode shows reversible pseudocapacitive charge storage within the studied negative potential range. An excellent rate capability and good capacitance retention make this active material a promising complementary electrode to MnO₂ for asymmetric supercapacitor devices.

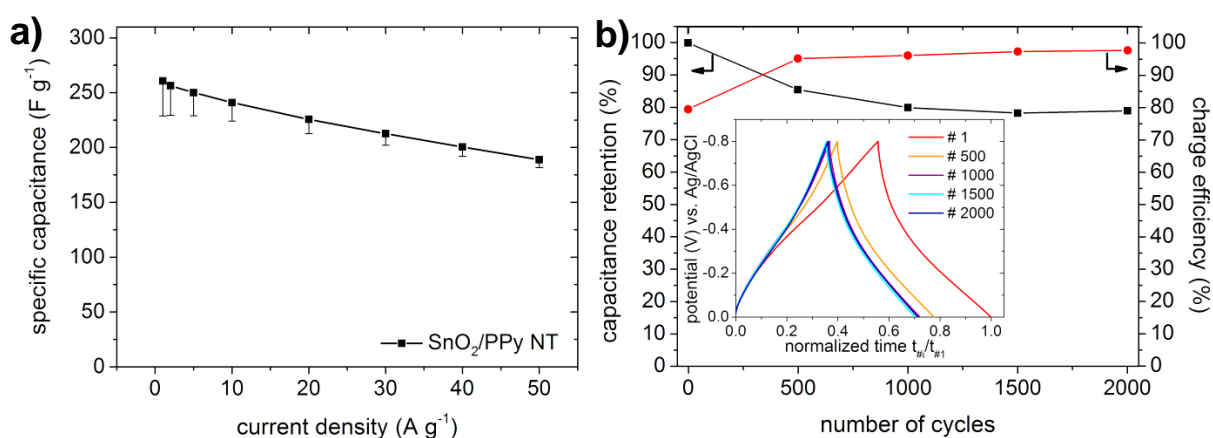


Figure 5-19 | Electrochemical performance of the SnO₂/PPy nanotube array. (a) Rate capability; (b) Long-time cycling stability and charge efficiency recorded at 5 A g⁻¹. The inset presents the respective charge/discharge curves.

Results and discussion

Electrochemical impedance spectroscopy is utilized to investigate the electrochemical performance of the SnO₂/PPy core/shell nanotube array further. Figure 5-20 presents the measured Nyquist and Bode plot. The impedance curve shows a compressed semi-circle in the high-frequency region and a steep line in the low-frequency region separated by the knee-frequency of 97.7 Hz. The equivalent series resistance and charge-transfer resistance are derived according to the procedure described in Section 5.1.3 and are $R_s = (1.40 \pm 0.01) \Omega$ and $R_{CT} = (1.8 \pm 0.1) \Omega$. The comparison with literature values reveals that the PPy based core/shell nanotube array shows a superior charge-transfer resistance compared to other PPy nanostructures, including nanobelts ($26.54 \Omega \text{ cm}^{-2}$), nanobricks ($20.35 \Omega \text{ cm}^{-2}$) and nanoneedels ($11.66 \Omega \text{ cm}^{-2}$).^[103] These results indicate that the high aspect ratio core/shell structure enables an efficient intercalation and deintercalation of charged species into the active electrode shell compared to other nanostructures. The solid capacitive behavior of the SnO₂/PPy electrode is reflected by both the steep line in the low-frequency part of the Nyquist plot and the large phase angle of 79.6° at 0.05 Hz, as observed in the Bode plot, suggesting that the performance is close to that of an ideal capacitor. The supercapacitor response frequency f_0 of 0.86 Hz at 45° and the corresponding time constant τ_0 of 1.16 s assign the electrode a good capacitive behavior even at high frequencies. The results obtained from EIS of the SnO₂/PPy structure are in agreement with the performance values reported for the o-SnO₂/MnO₂ structure in Section 5.1.3 and thus verify the beneficial electrochemical performance that originates from the core/shell structure with a short ion diffusion in the shell and a favorable electron transport through the core.

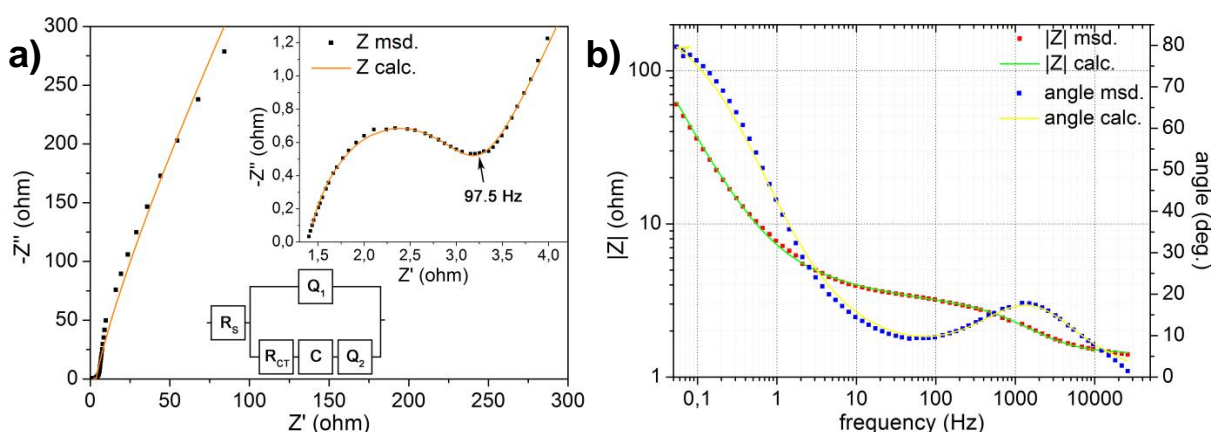


Figure 5-20 | Electrochemical impedance spectroscopy of the SnO₂/PPy core/shell nanotube array. (a) Nyquist plot and (b) Bode plot displayed in a frequency range from 50 kHz to 50 mHz (dots: measured values; lines: fit according to displayed equivalent circuit model).

5.3 Asymmetric PPy//MnO₂ supercapacitor

An asymmetric PPy//MnO₂ supercapacitor device is assembled based on the individual SnO₂/MnO₂ (Section 5.1) and SnO₂/PPy (Section 5.2) electrodes. Both three-dimensional core/shell electrodes are fabricated on the basis of the synthesized open-end SnO₂ nanotube arrays and are integrated into an asymmetric supercapacitor, as illustrated in Figure 5-21. Thereby, the negative and positive electrodes are disjoint from one another by an electrical isolating but ionically conducting separator. In the following section, the device is characterized with respect to its electrochemical performance for supercapacitor applications and the results are set into perspective with other reported symmetric and asymmetric supercapacitor configurations.

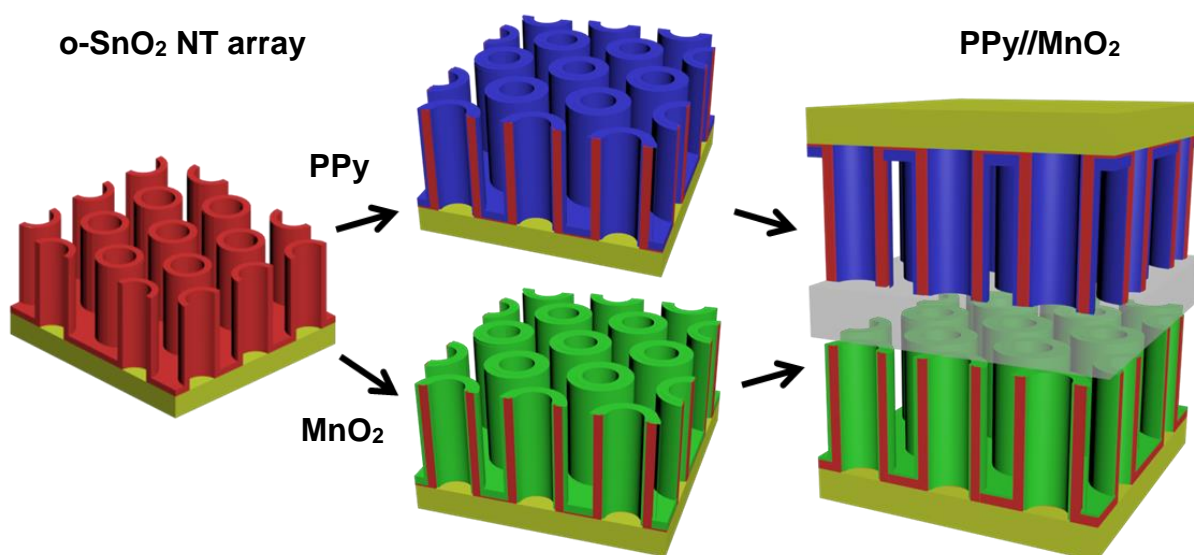


Figure 5-21 | Schematic diagram, illustrating the fabrication and assembling process of the asymmetric three-dimensionally nanostructured supercapacitor device. Self-supported o-SnO₂ nanotube arrays serve as a fundamental substructure to fabricate either SnO₂/PPy or SnO₂/MnO₂ core/shell nanotube arrays. The 3D nano-engineered negative (SnO₂/PPy) and positive (SnO₂/MnO₂) electrodes are separated from each other by a thin separator and are integrated into one single asymmetric aqueous based supercapacitor device (PPy//MnO₂).^[15]

5.3.1 The device operating potential window: Synergetic effect from the asymmetric configuration

The increase of the operating potential window is a highly promising strategy for supercapacitor devices to realize high specific energy. The large potential for a performance improvement is based on the fact that the stored energy in supercapacitors

Results and discussion

is proportional to the operating potential window squared, as outlined in eq. 2-1. Hence, a double in operating voltage window will lead to a four times increase in stored energy. An innovative approach to accomplish this aim in aqueous supercapacitor devices is based on an asymmetric device configuration that consists of complementary active electrode materials, see Section 2.5 for details. As the individual electrode performance of the negative PPy and positive MnO₂ based electrodes have been investigated within their respective voltage windows in the previous sections, it is natural to combine both electrodes into one device. The favorable combination of both materials becomes obvious when comparing individual CV studies of both materials, which are recorded in a three-electrode configuration, as displayed in Figure 5-22a. The diagram shows CV curves of the single SnO₂/PPy and SnO₂/MnO₂ core-shell nanotube arrays measured at 20 mV s⁻¹. Both materials exhibit pseudocapacitive behavior in complementary voltage windows, which suggests an accessible operating potential window of up to 1.7 V for a PPy//MnO₂ device. This prediction is verified by two-electrode CV measurements of the asymmetric PPy//MnO₂ device within varying operating potential windows, as shown in Figure 5-22b. The diagram displays the observed CV response at different operating potential windows from 0.9 to 1.7 V. All presented CV curves up to 1.7 V exhibit a highly reversible mirror-image current response on voltage reversal and show no current peaks related to dissociation of water, which could be expected at potentials higher than 1.23 V.

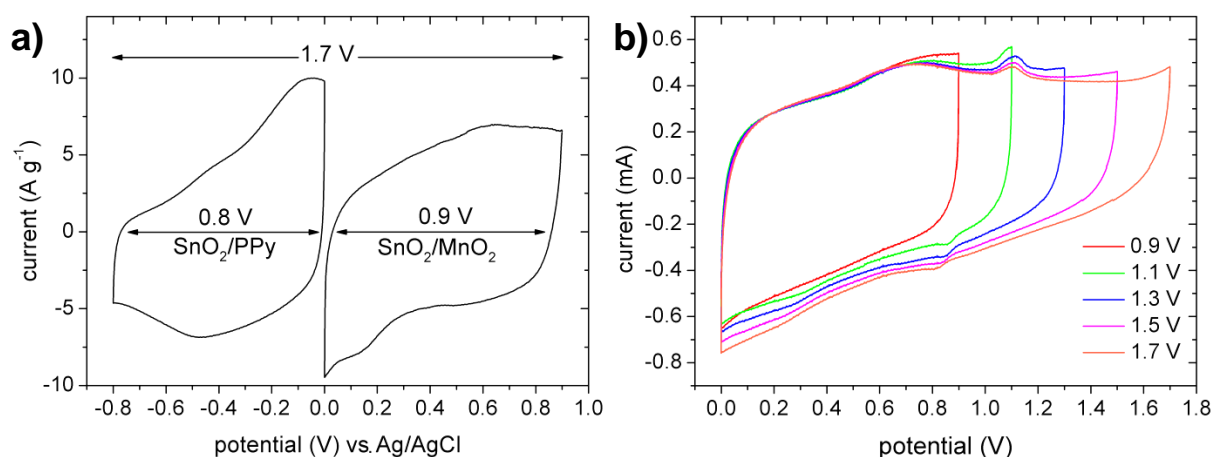


Figure 5-22 | Investigation of the operating potential window for the 3D asymmetric PPy//MnO₂ supercapacitor. a) CV curves of single SnO₂/PPy and SnO₂/MnO₂ core-shell nanotube arrays measured at 20 mV s⁻¹ in a three-electrode cell, showing the complementary voltage windows of both materials. b) CV curves of the asymmetric PPy//MnO₂ supercapacitor measured at different potential windows from 0.9 to 1.7 V in a two-electrode cell configuration at 20 mV s⁻¹, exhibiting a mirror-image current response on voltage reversal up to 1.7 V.^[15]

Results and discussion

Thereby, high over-potentials for hydrogen and oxygen evolution at the negative and positive electrodes extend the operating voltage window beyond the thermodynamic limit and enable reversible operation at potentials of up to 1.7 V. At higher operating potential windows, irreversible reactions evolve that most likely can be attributed to the dissociation of water.

5.3.2 Electrochemical performance of the asymmetric PPy//MnO₂ device

The electrochemical performance of the asymmetric PPy//MnO₂ device is analyzed in a two-electrode configuration with a 1 M Na₂SO₄ electrolyte in a potential window of 1.7 V. Figure 5-23a displays the CV curves of the device recorded at different potential scan rates. The diagram outlines that the electrochemical charge storage characteristics of the individual PPy and MnO₂ based electrodes are successfully implemented into an asymmetric device. The linear change in potential results in a nearly constant current response and hence, a fairly rectangular shape of the recorded CV curves. The rectangular shape is maintained even at high scan rates over the entire potential window of 1.7 V, indicating the good capacitive behavior of this device. The linear time-dependent change in potential at a constant applied current (*i.e.*, symmetric triangular shape of the galvanostatic charge/discharge profiles) supports this result, as shown in Figure 5-23b. Thereby, the asymmetric supercapacitor device exhibits a good long-time cycling stability with a capacitance retention of about 80 % after 2000 consecutive charge/discharge cycles (Figure 5-24a), which is in agreement with stability measurements of the individual PPy (Figure 5-19b) and MnO₂ (Figure 5-13b) based

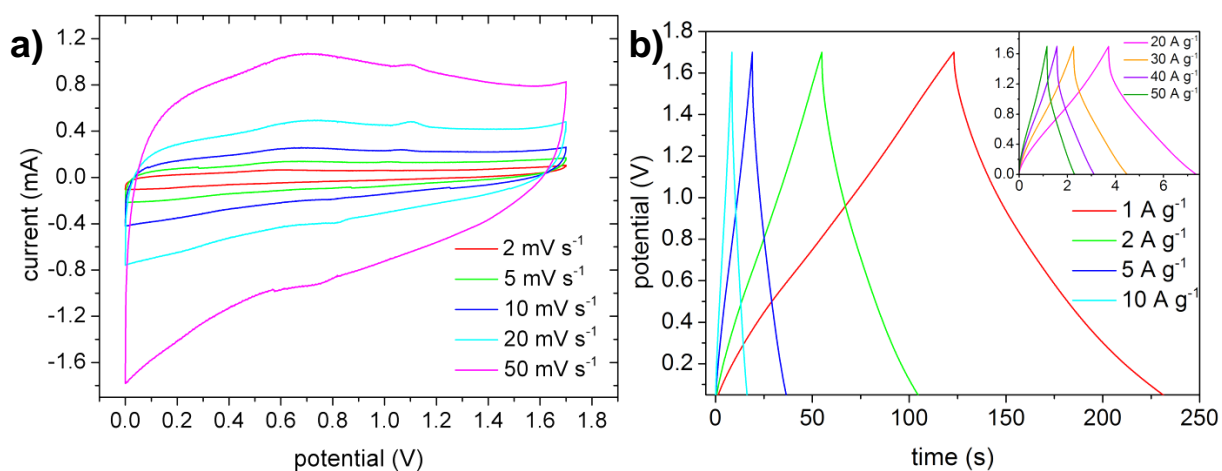


Figure 5-23 | Electrochemical performance of the 3D PPy//MnO₂ supercapacitor investigated in a two-electrode setup in a potential window of 1.7 V. a) CV curves recorded at different scan rates. b) Galvanostatic charge/discharge curves measured at various current densities.^[15]

Results and discussion

electrodes within their respective voltage windows. Throughout the entire long-time cycling stability analysis the asymmetric device shows high charge efficiency (> 96 %) and thus fulfills all the requirements set for supercapacitor charge storage, as defined in Section 2.1. Undoping and the formation of an isolating state at the PPy electrode under negative potentials, as one may expect, is unlike in symmetric PPy//PPy configurations, where the maximum cell voltage is imposed during the galvanostatic cycling, not an issue in an asymmetric device configuration together with a MnO₂ positive electrode. It has been proven by Béguin et al. that for an optimal usage of the electrical conducting polymer, the potential range of the negative electrode must be strictly controlled in order to prevent the PPy from reaching its insulating state.^[200] In a symmetric supercapacitor this might occur only when the cell voltage is very low, making such symmetric systems of poor interest in terms of energy storage.^[200] An asymmetric configuration in contrast, with two electrodes of different nature, is an excellent way to overcome the problems mentioned above (*i.e.*, with electrodes of different nature for positive and negative polarization). The main target, designing these systems, is to optimize the potential range of each electrode in order to allow them to operate in an optimal potential window, taking into account the need to obtain a high cell voltage. Hence, the careful balancing of the system, according to eq. 4-5, and the consideration of the requirements emphasized by Béguin et al.^[200] have led to a PPy//MnO₂ device that operates in the desired potential range at good stability.

The specific energy of the device is calculated from the gradient of the constant current discharge curve in Figure 5-23b according to eq. 4-3, while the specific power is derived by dividing the specific energy through the discharge time according to eq. 4-4. The performance is based on the PPy and MnO₂ mass loading. A possible contribution of the SnO₂ core is taken into account by the presented error bars according to eq. 4-6, as discussed in Section 4.2.6. All values are presented in Table A5. The asymmetric MnO₂//PPy supercapacitor exhibits a maximum specific energy of 27.2 Wh kg⁻¹ at 0.85 kW kg⁻¹ and maintains 7.8 Wh kg⁻¹ at 24.8 kW kg⁻¹, as outlined in the Ragone plot in Figure 5-24b (areal and volumetric device performance are shown in Figure A3). These values assign the device a high performance characteristic with excellent specific power, fulfilling the power target requirement of the Partnership for a New Generation of Vehicles (15 kW kg⁻¹ based on the active electrode mass).^[120,205] This performance exceeds the reported values of other asymmetric supercapacitor devices (see Figure 5-24b and Table A2), including Fe₂O₃//MnO₂^[190,193] and PEDOT//MnO₂^[203] and

Results and discussion

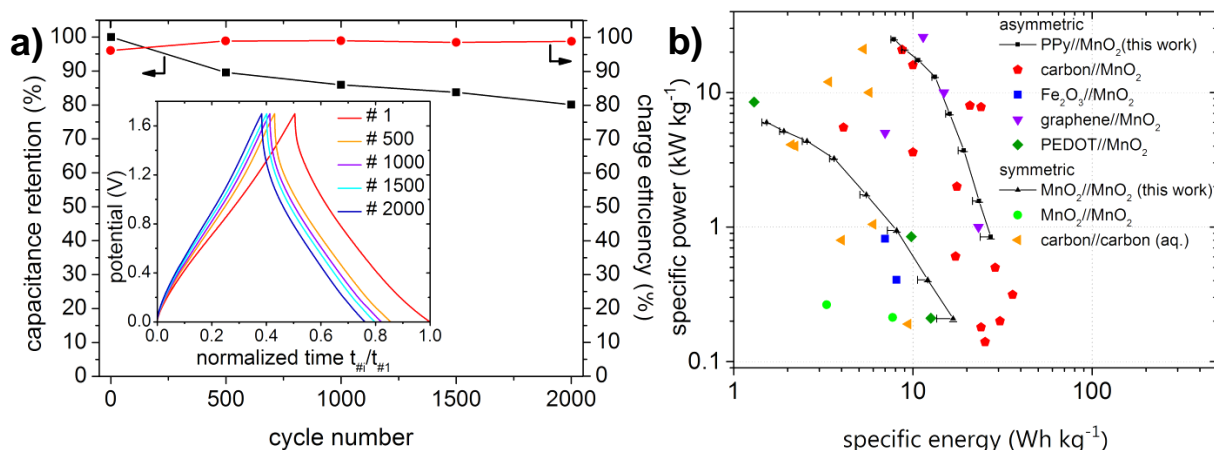


Figure 5-24 | Electrochemical performance of the 3D PPy//MnO₂ supercapacitor investigated in a two-electrode setup in a potential window of 1.7 V. (a) Long-time cycling stability and charge efficiency of the PPy//MnO₂ device (inset: charge/discharge curves). (b) Ragone plot, showing reported specific energy (E) and specific power (P_{real}) values of symmetric (MnO₂//MnO₂,^[190,203] carbon//carbon^[204-206]) and asymmetric supercapacitors (carbon//MnO₂,^[32,188-190,207-212] Fe₂O₃//MnO₂,^[190,193] graphene//MnO₂,^[33,213,214] PEDOT//MnO₂,^[203] and PPy//MnO₂).

competes with the highest reported values of carbon//MnO₂^[32,188-190,207-212] and graphene//MnO₂^[33,213,214] asymmetric devices. Moreover, the asymmetric PPy//MnO₂ supercapacitor strongly exceeds the electrochemical performance of aqueous supercapacitor devices based on symmetric electrode configurations, like MnO₂//MnO₂^[190,355] and carbon//carbon.^[204-206] As a reference, the performance of a symmetric device based on two self-supported 3D SnO₂/MnO₂ electrodes that operated at 0.9 V was investigated (data reported in Table A6). The symmetric device exhibited remarkably lower specific energy and specific power values compared to the asymmetric PPy//MnO₂ device, as shown in the performance comparison in Figure 5-24b. This result highlights that an asymmetric device configuration is highly desirable for supercapacitor applications and that the PPy//MnO₂ configuration can efficiently improve the specific energy without sacrificing specific power. As a proof of concept, the asymmetric supercapacitor can light up a red LED, as shown in Figure A4.

These results demonstrate that the merging of the self-supported 3D PPy and MnO₂ based core/shell nanotube arrays into one single device offers a new path to enhance the electrochemical performance of supercapacitors. The unique device configuration implements the advantages that arise from a 3D functional nanostructured electrode design, as emphasized in Section 3.1, and the asymmetric electrode configuration into one device. The 3D functional nanostructure array increases the surface area of the

Results and discussion

electrodes drastically and hence, increases the number of active sides for charge storage at the surface. The asymmetric electrode design enlarges the operating potential window. Both lead to an increase in specific energy. Thereby, the core/shell design ensures a rapid charge carrier transport throughout the entire electrode matrix and provides an efficient utilization of the active electrode material, which is a key criterion to obtain high specific power, as supported by recent results.^[368]

Leakage current is a serious concern in supercapacitor applications. The development of the leakage current of the PPy//MnO₂ device is recorded over time at a potential hold of 1.7 V, as shown in Figure 5-25a, and is determined to be 57 μ A after 30 minutes. The reported value is in the range of a published CNT/PANI supercapacitor.^[369] Unfortunately, very few publications report the leakage current of their device and detailed studies about leakage current in nanostructured pseudocapacitive electrode materials are not available for comparison at the moment. Beside the leakage current the evolution of the open circuit potential after initial charging is a relevant measure for the final device performance. Therefore, the asymmetric supercapacitor device was charged to 1.7 V and the decay of the open circuit potential over time was recorded, as presented in Figure 5-25b. The PPy//MnO₂ device remained about 0.9 V after 30 minutes. Unfortunately, measures of the evolution of the open circuit potential with progressing time are rare in literature and a meaningful comparison to other self-supported nanostructured supercapacitor devices cannot be given. Hence, the in this study reported values of leakage current and open circuit potential vs. time can serve as a measure for upcoming publications.

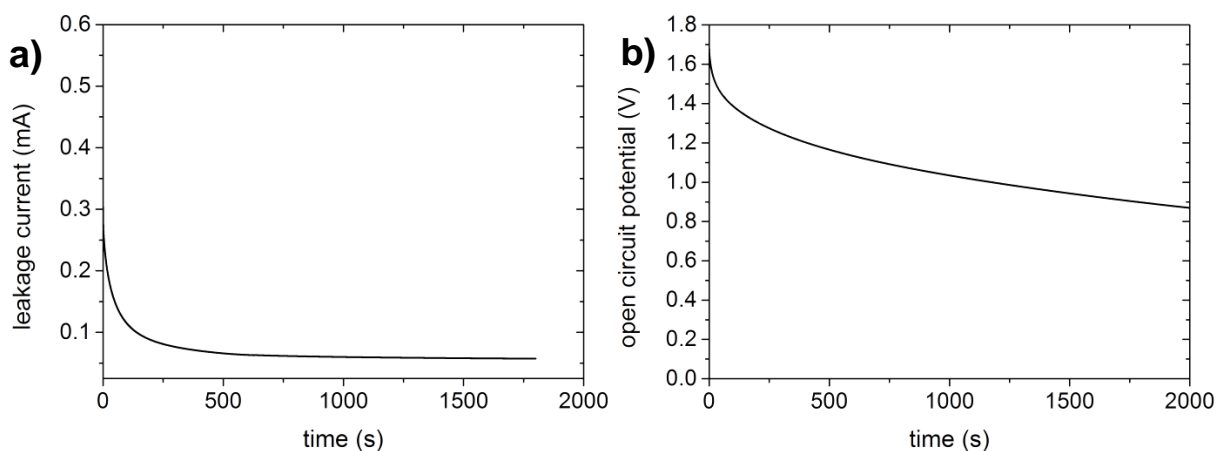


Figure 5-25 | Investigation of the leakage current and open circuit potential. a) Leakage current vs. time profile of the reported device at a potential hold of 1.7 V. b) Open circuit potential vs. time profile after charging the asymmetric supercapacitor to 1.7 V.^[15]

Results and discussion

The electrochemical performance of the PPy//MnO₂ asymmetric device is further characterized by EIS. Figure 5-26 presents the measured Nyquist and Bode plot. The impedance curve in Figure 5-26a exhibits a compressed semi-circle in the high-frequency region and a steep line in the low-frequency region which are separated by the knee-frequency of 219 Hz. The equivalent series resistance and charge-transfer resistance are derived according to the procedure described in Section 5.1.3 and are $R_S = (2.00 \pm 0.02) \Omega$ and $R_{CT} = (12.3 \pm 0.1) \Omega$. The equivalent series resistance is in agreement with the values obtained for the individual electrode characterization and assigns the device a good power capability, which has been demonstrated by galvanostatic charge/discharge measurements. Thereby, the solid capacitive behavior of the asymmetric supercapacitor is reflected by both the steep line in the low-frequency part of the Nyquist plot and the phase angle of 71.6° at 0.01 Hz as observed in the Bode plot in Figure 5-26b. The good capacitive behavior, even at high frequencies, is supported by the fast response frequency f_0 of 0.21 Hz at 45° and the corresponding time constant τ_0 of 4.8 s. For comparison, conventional activated carbon supercapacitors exhibit time constants at the order of 10 s.^[370] It is believed that this rapid frequency response of the PPy//MnO₂ device is based on the unique 3D nano-tubular electrode structure, which provides a high surface area and an enhanced charge carrier transport rate with short ion diffusion in the shell and a favorable electron transport through the core. Hence, this self-supported electrode architecture leads to an efficient intercalation and deintercalation of charged species into the active electrode shell compared to other structures and enables fast charging and discharging rates.

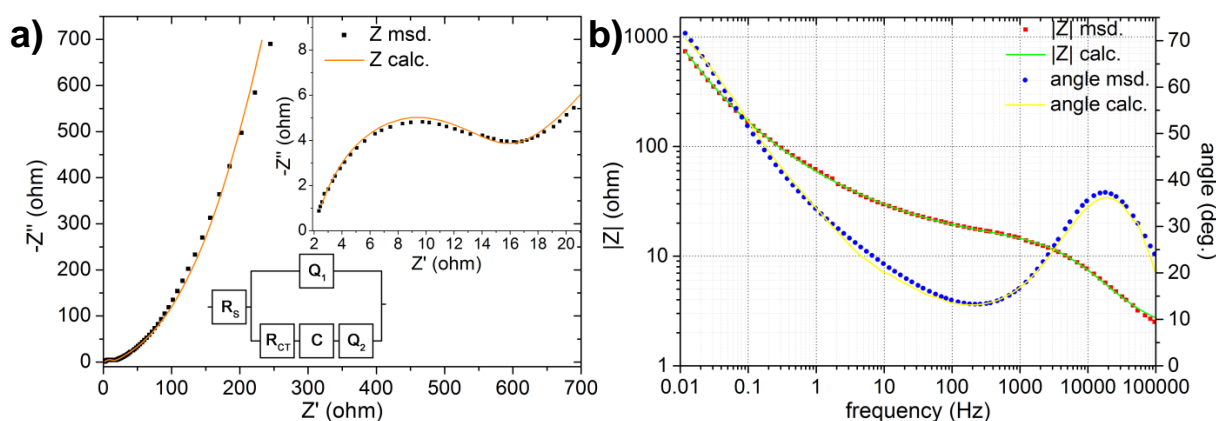


Figure 5-26 | Electrochemical impedance spectroscopy of the asymmetric PPy//MnO₂ supercapacitor. (a) Nyquist plot and (b) Bode plot displayed in a frequency range from 100 kHz to 10 mHz (dots: measured values; lines: fit according to displayed equivalent circuit model).

5.4 Three-dimensional C-TiN and TiN nanotube arrays: Improving the cycling stability of metal nitrides in aqueous supercapacitors

Three-dimensional nanostructures and carbon coatings on functional nanomaterials can both efficiently improve the performance of energy related applications (see Section 3.5). However, conventional carbon coating techniques are not capable of synthesizing thin and homogeneous carbon films on three-dimensional dense nanostructure arrays. Therefore, new methods need to be developed that can circumvent this limitation. It would be highly desirable if three-dimensional nanostructures prepared by well-established AAO technology could be coated with carbon. In this section, an innovative approach is presented that prepares a conformal functional carbon film inside an AAO template prior to the active material deposition and thus provides a versatile strategy to synthesize carbon coatings on three-dimensional nanostructured active materials. The utilized fabrication process is based on the self-assembly of polymeric nano-micelles on the AAO template and a subsequent deposition of the active material by ALD. As a proof of concept, carbon coated TiN and TiN nanotube arrays are synthesized and it is shown that the carbon coated array exhibits superior long-time cycling stability.

5.4.1 Structural investigation

The synthesis of self-supported 3D carbon coated TiN (C-TiN) and bare TiN nanotube arrays is realized by a template assisted fabrication process according to Figure 5-27. The TiN (route A) and C-TiN (route B) nanotubes are synthesized selectively in the pores of nano-porous AAO templates. Via route A: The bare TiN nanotube array is fabricated directly in the pores of the AAO template by the use of an ALD process from TiCl_4 and NH_3 at 400 °C (step i' \rightarrow step ii'). After the deposition process the TiN nanotube array is liberated by etching the template (step iii') and a self-supported TiN nanotube array is gained. In contrast, the formation of a conformal 3D carbon coating on the surface of the TiN nanotube array requires the implementation of an innovative carbon coating technique. Therefore an intermediate step before the ALD deposition of TiN is introduced into the synthesis process (step i) in order to form the required conformal carbon film. Importantly, the carbon coating is synthesized first and then the TiN material is deposited inside, enabling a highly conformal coating on a dense three-dimensional nanostructure array.

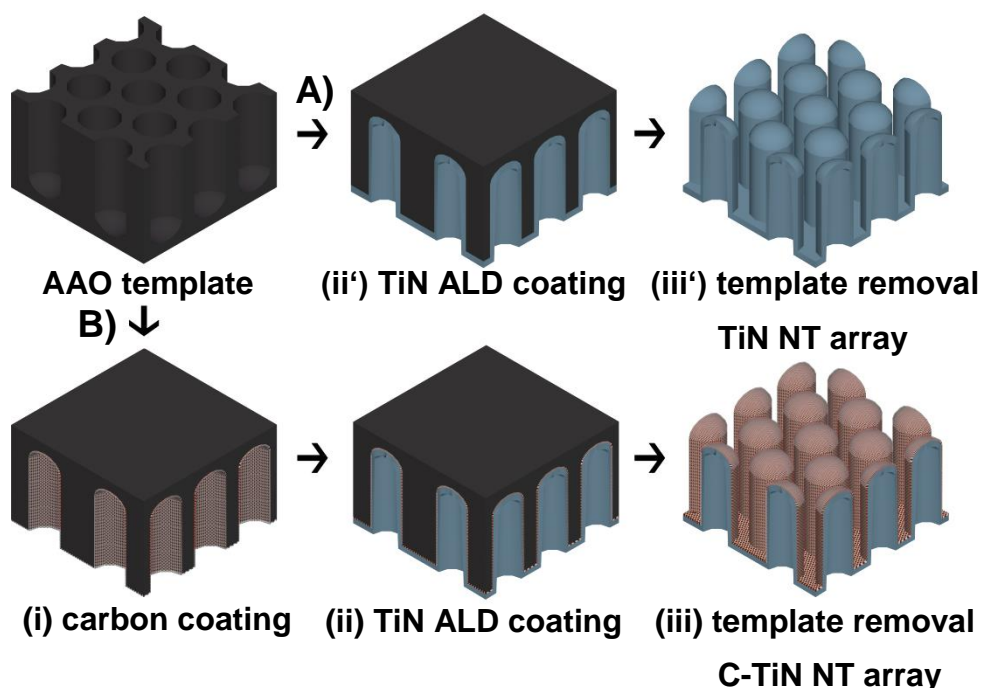


Figure 5-27 | Schematic diagram, illustrating the template-assisted fabrication process of self-supported TiN (route A) and C-TiN (route B) nanotube arrays. Route A: TiN is directly deposited into an AAO template by ALD and the entire template is etched; Route B: First, a carbon layer is synthesized on the surface of the AAO template from self-assembled PNMs and a subsequent annealing process. Then, TiN is deposited into the carbon coated AAO template by ALD and the template is etched.^[17]

The carbon coating of the nano-porous AAO template in step i is based on the self-assembly of polymeric nano-micelles (PNMs) on the surface of the AAO. The PNMs are buildup of amphiphilic molecules and are synthesized from Pluronic F-127 block copolymer (consists of poly(propylene oxide) and poly(ethylene oxide)) and a phenol/formaldehyde resol.^[333] Thereby, PNMs assemble spontaneously in aqueous media because of the aggregation of the amphiphilic molecules in which the hydrophilic ends form an outer shell and the hydrophobic ends arrange in the micellar core.^[371] The PNMs are synthesized according to Section 4.1.5 and serve as a fundamental substructure and carbon source. The immersion of a bare AAO template (Figure 5-28a) inside the PNM solution leads to a self-assembly of PNMs on the pore walls of the AAO template, which is believed to be driven by electrostatic interaction between the AAO pore walls and the micelles. In the following, the assembled PNMs are cross-linked by a hydrothermal treatment at 130 °C to form a 3D conformal Bakelite resin polymer (yellow in color, Figure 5-28b). Finally, the as-coated AAO template is annealed at 550 °C in nitrogen atmosphere and the polymer coating is carbonized into a continuous film (black

Results and discussion

in color, Figure 5-28c). This carbon film is coated homogeneously on the entire surface of the AAO template. This is verified by top-view SEM analysis as shown in Figure 5-28d-f. Figure 5-28d and e show a low and high magnification image of the carbon coated AAO template. The images outline that the nano-porous hexagonal morphology is maintained after the carbon coating process and no overgrowth or pore closing is present. For comparison, Figure 5-28f displays a top-view SEM image of an uncoated AAO template. The homogeneous 3D conformal coating of the AAO template by carbon (each AAO pore of ca. 10^{10} pores cm^{-2} is coated) is further verified by SEM after the AAO template is etched away and the 3D carbon structure (*i.e.*, self-supported carbon nanotube array) is liberalized. Figure 5-28g-i present the liberalized carbon film that forms continuous carbon nanotubes. The nanotubes have inherited the diameter and length from the initial AAO template geometry. It is worth mentioning that AAO templates with a wide range of pore diameters and pore lengths can be coated by this technique.

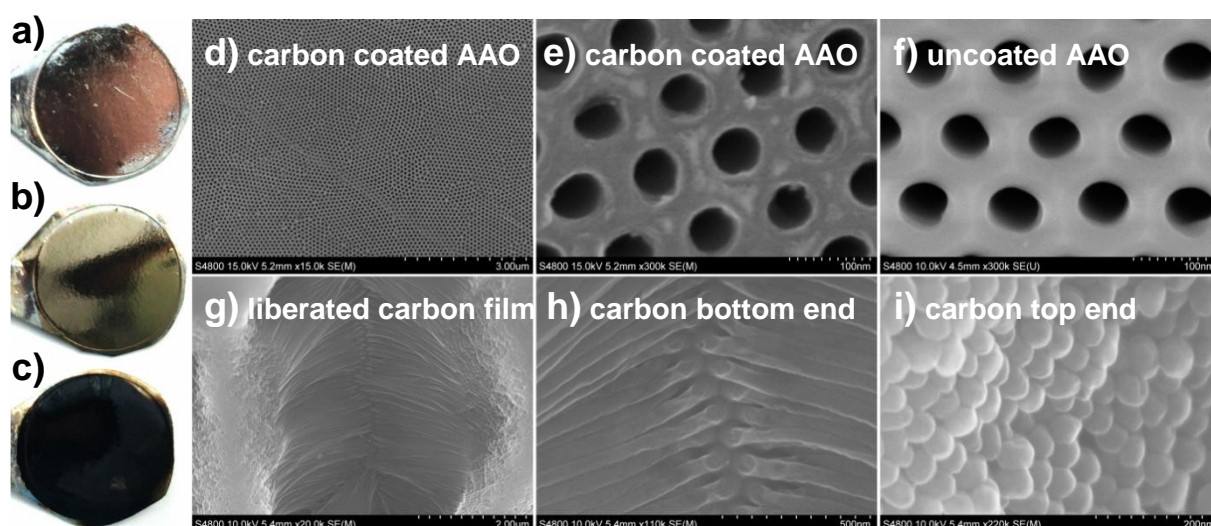


Figure 5-28 | Structural investigation of the synthesized carbon. (a-c) Pictures of a bare, polymer coated and carbon coated AAO template, respectively. The coating footprint area is approximately 1.26 cm^2 large; (d, e) Overview and high magnification top-view SEM images of a carbon coated AAO template, showing the well-preserved nano-porous AAO morphology after coating. (f) Bare AAO template for comparison. (g) Top-view low magnification SEM image of liberated carbon nanotubes after AAO template removal. (h) High magnification image of the carbon nanotube bottom end. (i) High magnification image of the closed top-ends of the carbon nanotubes (originating from the AAO barrier layer), proving the formation of a continuous carbon layer on the AAO template by the developed fabrication technique.^[17]

Results and discussion

Figure 5-29a presents a TEM image of a single carbon nanotube (no TiN is deposited inside) which was synthesized by the developed PNM approach inside an AAO pore. The carbon nanotube structure exhibits a diameter of ca. 60 nm, is continuous and of amorphous nature, as indicated by the SAED pattern in the inset of Figure 5-29a. Figure 5-29b and c show a large magnification and a cross-section SEM image of the self-supported 3D C-TiN nanotube array (Figure 5-27 step iii'). The C-TiN nanotubes exhibit a diameter of ca. 60 nm and a length ca. 1.2 μm . The images prove that adjacent nanotubes are vertically aligned, possess self-supporting capacity and exhibit a curved close-end nanotube nature, which originates from the AAO barrier layer. Hence, the closed-end TiN nanotube is encapsulated entirely by the carbon film, which defines the carbon coated TiN morphology.

The successful formation of C-TiN nanotubes is further verified by TEM and EDX line scans. Figure 5-30a outlines that the fabricated carbon shell on the TiN nanotube is in the range of ca. 2 to 3 nm thick and further highlights that the carbon film forms a continuous layer on the TiN nanotube. The thickness of the TiN nanotube is (10 ± 1) nm after 500 ALD cycles. The material distribution across a single C-TiN nanotube is characterized by EDX line scans on the basis of the Ti K_{α} , N K_{α} and C K_{α} spectra, as shown in Figure 5-30b (here: 1000 ALD cycles TiN for better EDX signal). The spectra show enhanced signal peaks of Ti K_{α} and N K_{α} located at the wall positions of the TiN nanotube, proving the hollow nano-tubular nature of the TiN structure.^[17] The C K_{α}

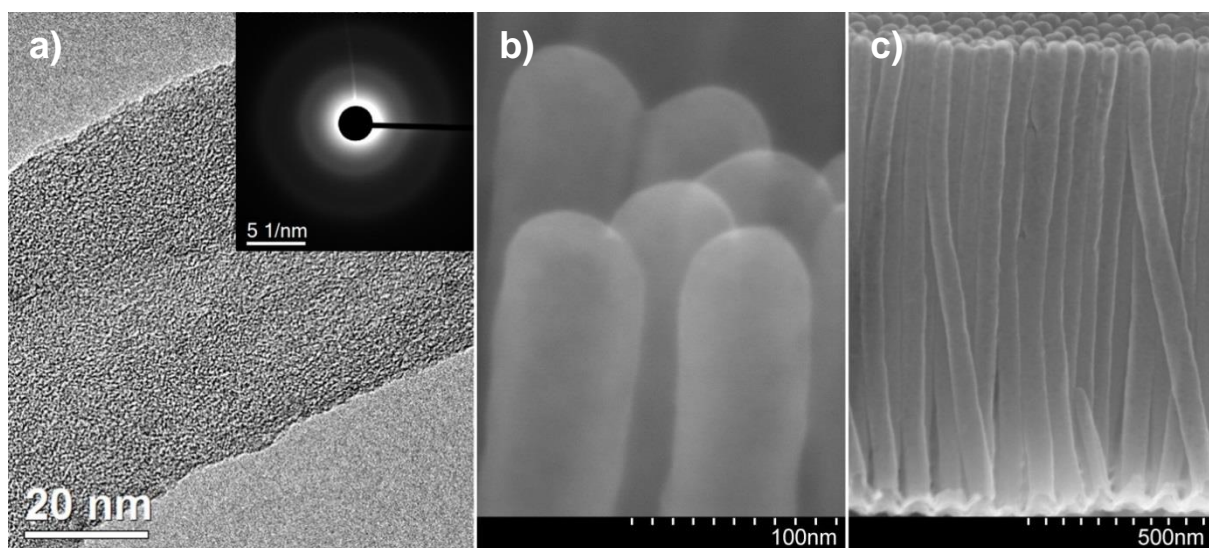


Figure 5-29 | Structural analysis of the synthesized carbon and C-TiN. (a) TEM image of a single carbon nanotube with a diameter of ca. 60 nm; Inset: SAED pattern. (b, c) large magnification of the closed nanotube top-end and cross-section SEM images of a C-TiN nanotube array.^[17]

Results and discussion

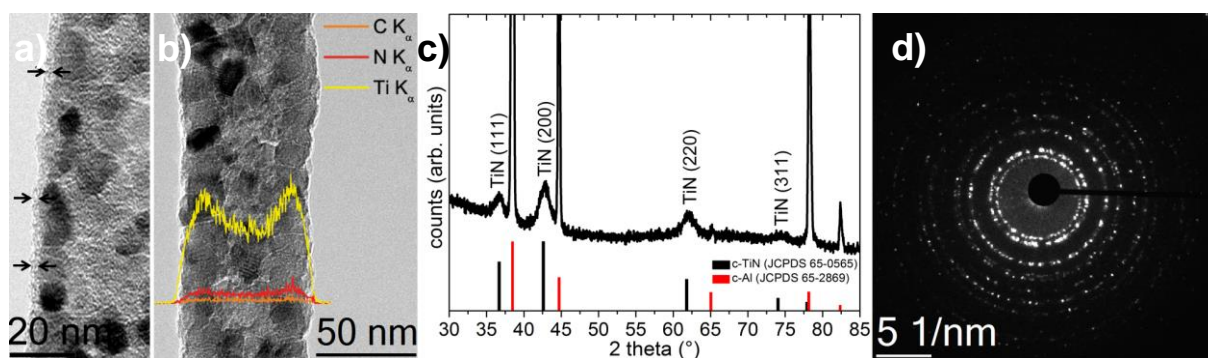


Figure 5-30 | TEM investigation of a single C-TiN nanotube and crystal structure of the TiN. (a) TEM image of the C-TiN nanotube wall, indicating a carbon layer thickness of ca. 2 to 3 nm. (b) TEM and EDX line scan of a single C-TiN nanotube. (c) XRD measurement of the C-TiN nanotube array, showing the formation of polycrystalline cubic TiN (Reference: JCPDS 65-0565). The signal of cubic Al (JCPDS 65-2869) originates from the sample substrate.^[17] (d) SAED pattern recorded on a single TiN nanotube, verifying the polycrystalline nature of the ALD prepared TiN.

spectrum exhibits a slightly increased signal across the nanotube, which originates from the carbon shell. The crystal structure of the ALD prepared TiN nanotube is characterized by X-ray diffraction measurements and SAED and could be attributed to polycrystalline cubic TiN on the basis of the (111), (200), (220), and (311) crystal planes, as shown in Figure 5-30c. The result is verified by a SAED measurement on a single TiN nanotube. The image in Figure 5-30d shows the typical pattern of a polycrystalline material and exhibits the characteristic d-spacings of $d_{(111)} = (0.26 \pm 0.02)$ nm, $d_{(200)} = (0.22 \pm 0.02)$ nm, $d_{(220)} = (0.16 \pm 0.02)$ nm, and $d_{(311)} = (0.13 \pm 0.02)$ nm for cubic TiN. All results from XRD and SAED analysis are in agreement with the reference data for cubic TiN (JCPDS 65-0565).

In contrast to the as-developed coating process, a conformal carbon coating on a self-supported 3D TiN nanotube array could not be realized by first synthesizing the TiN nanotube array inside an AAO template via route A and the subsequent coating of carbon. This inversed process (compared to route B) leads to an overgrowth and results in the formation of a thick carbon layer on top of the dense nanotube array, as shown in Figure 5-31a and b. The reason for the non-conformal coating is based on the fact that excessive amounts of the hydrothermally formed polymer on top and in-between the TiN nanotubes cannot be removed without destroying the three-dimensionally nanostructured array. Hence, the polymer will transform during the carbonization step into a carbon layer that is of non-conformal manner.^[17] In contrast excessive amounts of formed polymer can

Results and discussion

easily be wiped of the AAO surface, leaving a slightly yellow shimmered template, as shown in Figure 5-28b. This result indicates that commonly used carbon coating techniques, which were initially developed for powder samples, cannot directly be applied to dense arrays of self-supported nanostructures. The successful development of a conformal carbon coating technique that is capable of first fabricating the functional carbon shell and then depositing the active material inside is therefore a breakthrough in synthesizing highly conformal functional coatings on dense nanostructure arrays. This process can contribute to other material systems and applications because of the versatility of the approach (many materials can be deposited by ALD, see Figure A2).

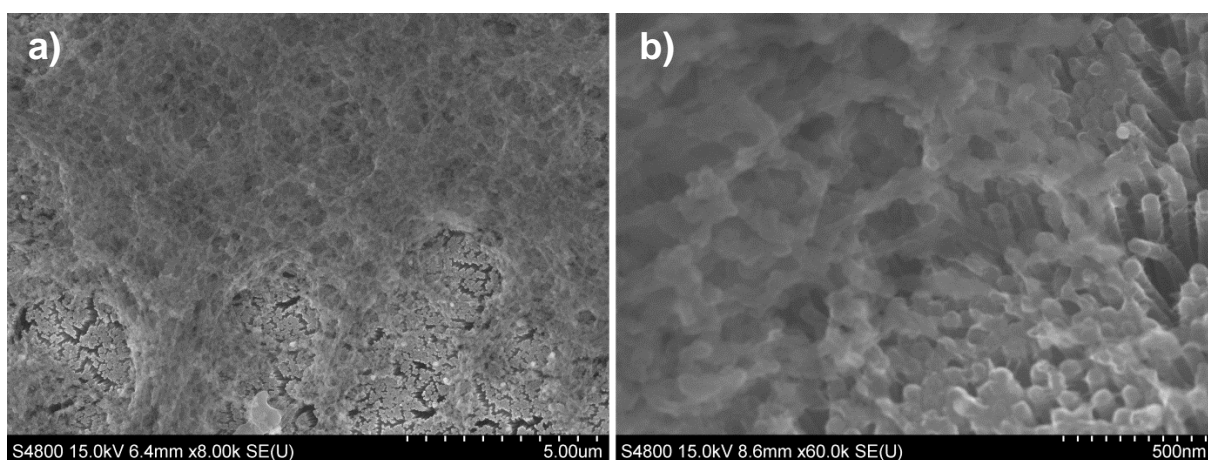


Figure 5-31 | (a) Overview and (b) high resolution SEM images of a TiN nanotube array fabricated via route A and the subsequent coating of carbon by the described PNM approach. The images clearly show that the TiN nanotube array is not coated in a conformal manner, as achieved by route B. Moreover, a thick carbon film covers the nanotube array to great extent.^[17]

5.4.2 Electrochemical performance

The as-synthesized self-supported 3D C-TiN and TiN nanotube arrays are both tested as negative electrode materials for aqueous based supercapacitor. The electrochemical performance is analyzed by CV and galvanostatic charge/discharge measurements in a standard three-electrode configuration. The utilized potential window is ranging from -1 V to 0 V vs. a Ag/AgCl RE and a 1 M KOH solution served as the electrolyte. Figure 5-32a shows the CV curves of a C-TiN electrode as displayed in Figure 5-29c (nanotube diameter ca. 60 nm, length ca. 1.2 μm) at scan rates ranging from 2 to 100 mV s⁻¹. The C-TiN exhibits a quasi-rectangular CV shape, which is maintained at high scan rates. This behavior indicates that the C-TiN electrode undergoes good reversible electrochemical charge storage and assigns the electrode a reliable capacitive behavior.

Results and discussion

In comparison, an electrode based on bare TiN with the same structural parameters as the C-TiN electrode shows some distortion from the ideal rectangular shape at high scan rates, as shown in Figure A5a, suggesting an inferior charge storage capability of the TiN electrode compared to the C-TiN electrode. This result is supported by galvanostatic charge/discharge measurements of the C-TiN (Figure 5-32b) and TiN electrode (Figure A5b), which are performed at current densities ranging from 1 to 50 A g⁻¹. The C-TiN electrode exhibits a more pronounced equilateral triangular shape of the consecutive charging and discharging processes, which is required for electrochemical charge storage in supercapacitors. Whereas the slope of the charging process of the bare TiN electrode is elongated compared to the discharging process, resulting in inferior charge/discharge efficiency. The specific capacitance and the rate capability of both electrodes are calculated based on the respective constant current discharge curves,

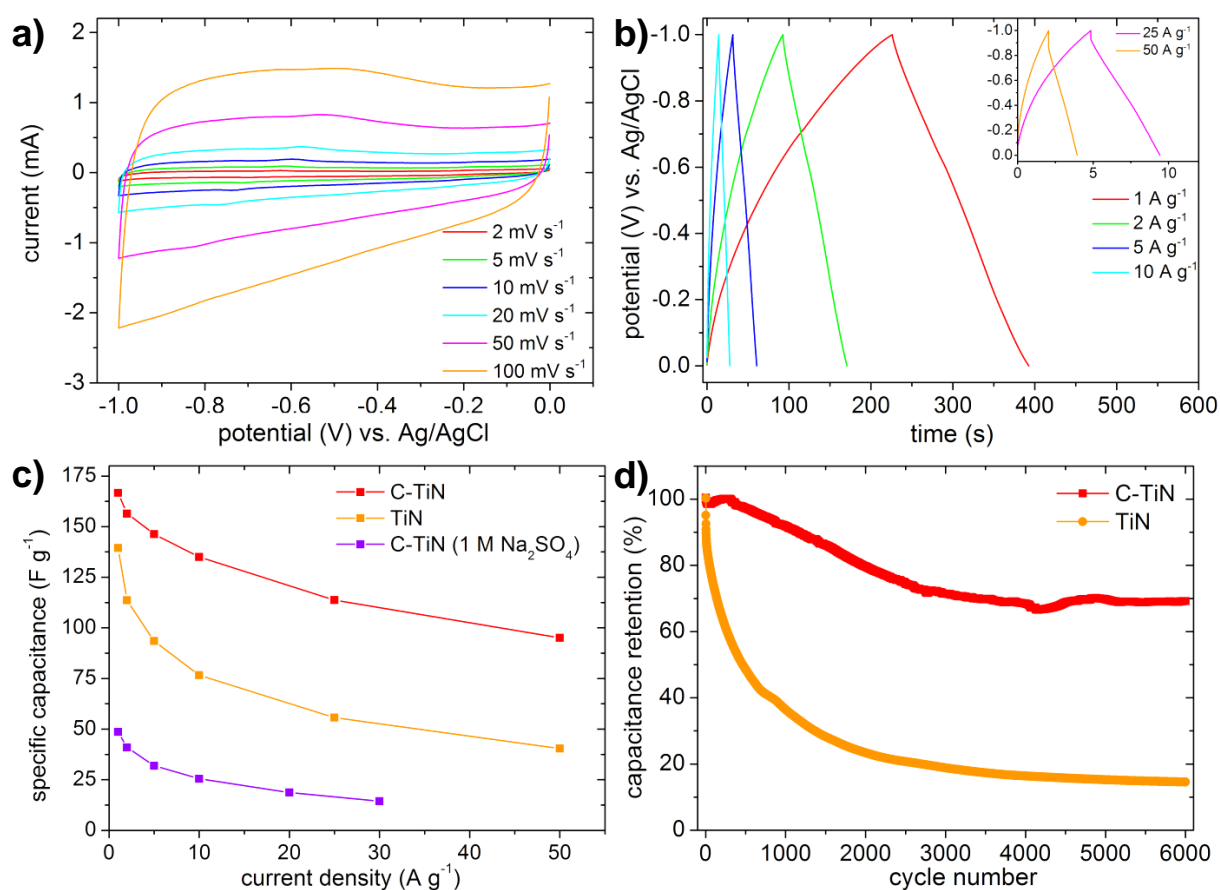


Figure 5-32 | Electrochemical investigation of the C-TiN and TiN nanotube arrays measured in a three-electrode configuration. (a, b) CV and charge/discharge profiles of the C-TiN nanotube array; (c) Rate performance of the C-TiN (in 1 M KOH and 1 M Na₂SO₄ electrolyte) and bare TiN (1 M KOH); (d) Long-time cycling ability of the C-TiN and TiN nanotube arrays.^[17]

Results and discussion

according to eq. 4-1. The results are displayed in Figure 5-32c. The C-TiN electrode possesses a specific capacitance of 167 F g^{-1} at 1 A g^{-1} and remains 95 F g^{-1} at 50 A g^{-1} . In contrast, the TiN electrode exhibits 140 F g^{-1} at 1 A g^{-1} and remains 61 F g^{-1} at 50 A g^{-1} . The performance enhancement of the C-TiN compared to the TiN nanotube array at low current densities can most likely be attributed to the active carbon shell, which itself contributes about 9.5 % to the specific capacitance of C-TiN, as shown in Figure A6. Whereas the pronounced decrease of the specific capacitance at high scan rates most likely originates from the poor cycling stability of the bare TiN electrode (prolonged cell history at high scan rates).^[17] The achieved specific capacitance values are in the range of previously reported values for TiN, as present in Figure 2-4. The electrochemical performance of the C-TiN nanotube array is further investigated in a neutral $1 \text{ M Na}_2\text{SO}_4$ electrolyte. The analysis has shown that the specific capacitance decreased strongly in the neutral electrolyte and could only remain about 30 % of the performance achieved in the alkaline electrolyte. When keeping in mind that aqueous based asymmetric supercapacitors are highly desirable to enhance the device energy storage capability (Section 2.5), then it is obvious that the synthesized C-TiN based material is a less suitable negative electrode candidate in systems that operate best in neutral electrolytes, like MnO_2 . Moreover, TiN should be considered as a negative electrode material in combination with complementary positive electrode materials that work best in alkaline electrolytes. This includes, but is not limited to, carbon based materials (up to ca. 250 F g^{-1} in alkaline electrolytes)^[18] and materials that show phase transformation like metal hydroxides (e.g., $\text{Co}(\text{OH})$,^[372] $\text{Ni}(\text{OH})_2$ ^[373]) and metal oxides (e.g., $\text{Ni}_{0.3}\text{Co}_{2.7}\text{O}_4$,^[374] NiCo_2O_4 ,^[375] NiO ^[198]).

The long-time cycling stability of metal nitride materials in supercapacitor applications remains one of the most crucial aspects. Therefore, the capacitance retention of the C-TiN and TiN nanotube arrays was analyzed during 6000 charge/discharge cycles at a current density of 10 A g^{-1} . The obtained results are shown in Figure 5-32d. As similarly reported by others,^[145,148,184,185] the bare TiN nanotube array suffered from severe capacitance fading and could only retain about 15 % of the initial capacitance. In contrast, the C-TiN nanotube array exhibited a strongly improved long-time cycling stability and could retain about 70 % of the initial capacitance, which is more than 4.5 times the performance of the bare TiN electrode. Thus, the 3D conformal carbon shell can efficiently stabilize the TiN nanotube array during long-time cycling. It is believed that the carbon shell primarily acts as a cage for TiN and prevents a structural breakdown and pulverization of the active material during charging and discharging. This assumption

Results and discussion

is verified by post cycling SEM investigations as shown in Figure 5-33a-c. The images clearly outline that the C-TiN nanotube arrays can maintain the initial nano-tubular structure even after 6000 consecutive charge/discharge cycles (Figure 5-33b), whereas the uncoated TiN nanotube array undergoes a strong change in morphology and devolves into a film like structure (Figure 5-33c).

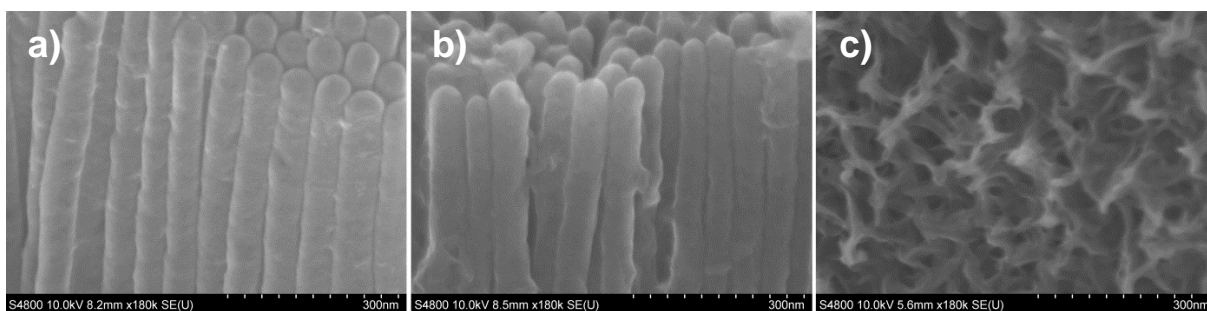


Figure 5-33 | Morphology investigation of the C-TiN and TiN electrode before and after long-time cycling. (a) C-TiN nanotube array before cycling; (b) Preserved C-TiN nanotube structure after 6000 charge/discharge cycles; (c) Initial TiN nanotube array has devolved into a film like structure after 6000 charge/discharge cycles.^[17]

6 Summary and outlook

In summary, throughout this thesis it has been shown that the electrochemical charge storage in supercapacitors can be enhanced by (i) utilizing pseudocapacitive materials, (ii) improving the EKMU by providing a three-dimensionally nanostructured electrode design and (iii) introducing an asymmetric supercapacitor configuration in order to operate a device at high potentials. Therefore a novel and versatile fabrication process was developed which is capable of synthesizing dense three-dimensional nanotube arrays of different pseudocapacitive materials (*e.g.*, core/shell nanotube arrays of SnO₂/MnO₂, SnO₂/PPy and C-TiN). Nano-porous AAO served as a template during the synthesis process and the active materials were fabricated by ALD and electrochemical deposition. It has been demonstrated that the developed process allows a precise control of the structural parameters within the nanometer regime, including length, spacing, diameter, wall thickness, coating, and the selection of open-end and closed-end nanotubes. The realization of the self-supported nanoscale design of the electrodes in combination with pseudocapacitive materials and an asymmetric electrode configuration (PPy//MnO₂) led to a supercapacitor device that experiences large specific energy while maintaining high specific power. Thereby, it has been found that one of the essential parameters to design high performance electrodes for supercapacitors is to optimize the utilization of the pseudocapacitive active electrode material by keeping its thin film morphology on a three-dimensionally nanostructured and electrical conductive matrix. Further, the successful development of an innovative carbon coating technique that can efficiently synthesize thin functional carbon films on three-dimensional nanotube arrays led to a drastic enhancement of the cycling stability of metal nitride based supercapacitors, as demonstrated for three-dimensional C-TiN nanotube arrays.

The work within this thesis has outlined, that in order to realize a new generation of electrochemical energy storage devices with high performance it requires breakthroughs in materials, not incremental changes to existing technology.^[9] It is believed that nano-engineered multifunctional three-dimensional nanoarchitectures, as the ones that are developed in this work, will be indispensable for the successful realization of high performance devices. Thereby, three-dimensional nanostructures will not only improve the performance of supercapacitors. Ultimately, they will rather serve as the basis for microscale batteries, fuel-cell architectures and advanced photovoltaic cells, all of which will exhibit significant performance advantages over current state-of-the-art technologies

Summary and outlook

in their respective fields.^[28] The obtained results within this work on three-dimensional nanostructuring and the device integration should provide a strong basis to achieve this aim and develop more advanced three-dimensional nanoarchitectures of different materials and their composition, as to target a broad range of applications.

7 Bibliography

- [1] S. Sorrell, J. Speirs, R. Bentley, A. Brandt & R. Miller. Global Oil Depletion: An Assessment of the Evidence for a Near-Term Peak in Global Oil Production. *UK Energy Research Center* 2009, 1-198.
- [2] N. A. Sciences & T. R. Society. Climate Change: Evidence and Causes. *National Academies Press*, 2014.
- [3] AG Energiebilanzen. Stromerzeugung nach Energieträgern 1990 - 2014 Stand 27.02.2015.
- [4] Amsterdam Roundtable Foundation and McKinsey & Company. Electric Vehicles in Europe: Gearing up for a New Phase? 2014, Ch. 1.
- [5] B. E. Conway. Electrochemical Supercapacitors: Scientific Fundamentals and Technological Applications. *Springer*, 1999.
- [6] P. Simon & Y. Gogotsi. Materials for Electrochemical Capacitors. *Nature Materials* 2008, 7, 845-854.
- [7] Fraunhofer Institute for Systems and Innovation Research ISI. Nanotechnology in the Sectors of Solar Energy and Energy Storage. *International Electrotechnical Commission*, 2013, Ch. 3.
- [8] E. Musk, I'd Bet On Capacitors Over Batteries, *Cleantech Forum in San Francisco 2011*, gigaom.com/2011/03/16/tesla-ceo-id-bet-on-capacitors-over-batteries, 06 Mai 2015.
- [9] A. S. Arico, P. Bruce, B. Scrosati, J.-M. Tarascon & W. van Schalkwijk. Nanostructured Materials for Advanced Energy Conversion and Storage Devices. *Nature Materials* 2005, 4, 366-377.
- [10] S. Chabi, C. Peng, D. Hu & Y. Zhu. Ideal Three-Dimensional Electrode Structures for Electrochemical Energy Storage. *Advanced Materials* 2013, 26, 2440-2445.
- [11] B. E. Conway & W. G. Pell. Double-Layer and Pseudocapacitance Types of Electrochemical Capacitors and Their Applications to the Development of Hybrid Devices. *Journal of Solid State Electrochemistry* 2003, 7, 637-644.
- [12] C.-C. Hu, K.-H. Chang, M.-C. Lin & Y.-T. Wu. Design and Tailoring of the Nanotubular Arrayed Architecture of Hydrous RuO₂ for Next Generation Supercapacitors. *Nano Letters* 2006, 6, 2690-2695.
- [13] F. Grote, L. Wen & Y. Lei. Nano-Engineering of Three-Dimensional Core/Shell Nanotube Arrays for High Performance Supercapacitors. *Journal of Power Sources* 2014, 256, 37-42.
- [14] D. Vonlanthen, P. Lazarev, K. A. See, F. Wudl & A. J. Heeger. A Stable Polyaniline-Benzoquinone-Hydroquinone Supercapacitor. *Advanced Materials* 2014, 26, 5095-5100.
- [15] F. Grote & Y. Lei. A Complete Three-Dimensionally Nanostructured Asymmetric Supercapacitor with High Operating Voltage Window based on PPy and MnO₂. *Nano Energy* 2014, 10, 63-70.
- [16] D. Choi, G. E. Blomgren & P. N. Kumta. Fast and Reversible Surface Redox Reaction in Nanocrystalline Vanadium Nitride Supercapacitors. *Advanced Materials* 2006, 18, 1178-1182.
- [17] F. Grote, H. Zhao & Y. Lei. Self-Supported Carbon Coated TiN Nanotube Arrays: Innovative Carbon Coating Leads to an Improved Cycling Ability for Supercapacitor Applications. *Journal of Materials Chemistry A* 2015, 3, 3465-3470.

Bibliography

- [18] J. W. Long, D. Bélanger, T. Brousse, W. Sugimoto, M. B. Sassin & O. Crosnier. Asymmetric Electrochemical Capacitors—Stretching the Limits of Aqueous Electrolytes. *MRS Bulletin* 2011, 36, 513-522.
- [19] A. Balducci, R. Dugas, P. L. Taberna, P. Simon, D. Plée, M. Mastragostino & S. Passerini. High Temperature Carbon–Carbon Supercapacitor using Ionic Liquid as Electrolyte. *Journal of Power Sources* 2007, 165, 922-927.
- [20] S. Pohlmann, T. Olyschläger, P. Goodrich, J. A. Vicente, J. Jacquemin & A. Balducci. Mixtures of Azepanium Based Ionic Liquids and Propylene Carbonate as High Voltage Electrolytes for Supercapacitors. *Electrochimica Acta* 2015, 153, 426-432.
- [21] J. B. Goodenough, H. D. Abruna & M. V. Buchanan. Basic Research Needs for Electrical Energy Storage. Report of the Basic Energy Sciences Workshop on Electrical Energy Storage. *Office of Basic Energy Sciences* 2007, 48-49.
- [22] Y. Gogotsi. What Nano Can Do for Energy Storage. *ACS Nano* 2014, 8, 5369-5371.
- [23] K. H. An, W. S. Kim, Y. S. Park, J. M. Moon, D. J. Bae, S. C. Lim, Y. S. Lee & Y. H. Lee. Electrochemical Properties of High-Power Supercapacitors Using Single-Walled Carbon Nanotube Electrodes. *Advanced Functional Materials* 2001, 11, 387-392.
- [24] H. Jiang, T. Zhao, J. Ma, C. Yan & C. Li. Ultrafine Manganese Dioxide Nanowire Network for High-Performance Supercapacitors. *Chemical Communications* 2011, 47, 1264-1266.
- [25] H. Wang, Z. Xu, A. Kohandehghan, Z. Li, K. Cui, X. Tan, T. J. Stephenson, C. K. King'andu, C. M. B. Holt, B. C. Olsen, J. K. Tak, D. Harfield, A. O. Anyia & D. Mitlin. Interconnected Carbon Nanosheets Derived from Hemp for Ultrafast Supercapacitors with High Energy. *ACS Nano* 2013, 7, 5131-5141.
- [26] J. W. Long, B. Dunn, D. R. Rolison & H. S. White. Three-Dimensional Battery Architectures. *Chemical Reviews* 2004, 104, 4463-4492.
- [27] T. S. Arthur, D. J. Bates, N. Cirigliano, D. C. Johnson, P. Malati, J. M. Mosby, E. Perre, M. T. Rawls, A. L. Prieto & B. Dunn. Three-Dimensional Electrodes and Battery Architectures. *MRS Bulletin* 2011, 36, 523-531.
- [28] D. R. Rolison, J. W. Long, J. C. Lytle, A. E. Fischer, C. P. Rhodes, T. M. McEvoy, M. E. Bourg & A. M. Lubers. Multifunctional 3D Nanoarchitectures for Energy Storage and Conversion. *Chemical Society Review*. 2009, 38, 226-252.
- [29] A. Kargar, K. Sun, Y. Jing, C. Choi, H. Jeong, G. Y. Jung, S. Jin & D. Wang. 3D Branched Nanowire Photoelectrochemical Electrodes for Efficient Solar Water Splitting. *ACS Nano* 2013, 7, 9407-9415.
- [30] Y. J. Hwang, A. Boukai & P. Yang. High Density n-Si/n-TiO₂ Core/Shell Nanowire Arrays with Enhanced Photoactivity. *Nano Letters* 2008, 9, 410-415.
- [31] V. Khomenko, E. Raymundo-Piñero & F. Béguin. Optimisation of an Asymmetric Manganese Oxide/Activated Carbon Capacitor Working at 2 V in Aqueous Medium. *Journal of Power Sources* 2006, 153, 183-190.
- [32] Q. T. Qu, L. Li, S. Tian, W. L. Guo, Y. P. Wu & R. Holze. A Cheap Asymmetric Supercapacitor with High Energy at High Power: Activated Carbon//K_{0.27}MnO₂·0.6H₂O. *Journal of Power Sources* 2010, 195, 2789-2794.
- [33] H. Gao, F. Xiao, C. B. Ching & H. Duan. High-Performance Asymmetric Supercapacitor Based on Graphene Hydrogel and Nanostructured MnO₂. *ACS Applied Materials & Interfaces* 2012, 4, 2801-2810.

Bibliography

- [34] L. Demarconnay, E. Raymundo-Pinero & F. Beguin. Adjustment of Electrodes Potential Window in an Asymmetric Carbon/MnO₂ Supercapacitor. *Journal of Power Sources* 2011, 196, 580-586.
- [35] L.-F. Chen, Z.-H. Huang, H.-W. Liang, Q.-F. Guan & S.-H. Yu. Supercapacitors: Bacterial-Cellulose-Derived Carbon Nanofiber@MnO₂ and Nitrogen-Doped Carbon Nanofiber Electrode Materials: An Asymmetric Supercapacitor with High Energy and Power Density. *Advanced Materials* 2013, 25, 4816-4816.
- [36] F. Grote, R.-S. Kühnel, A. Balducci & Y. Lei. Template Assisted Fabrication of Free-Standing MnO₂ Nanotube and Nanowire Arrays and Their Application in Supercapacitors. *Applied Physics Letters* 2014, 104, 053904
- [37] R. L. Porto, R. Frappier, J. B. Ducros, C. Aucher, H. Mosqueda, S. Chenu, B. Chavillon, F. Tessier, F. Cheviré & T. Brousse. Titanium and Vanadium Oxynitride Powders as Pseudo-Capacitive Materials for Electrochemical Capacitors. *Electrochimica Acta* 2012, 82, 257-262.
- [38] V. Augustyn, P. Simon & B. Dunn. Pseudocapacitive Oxide Materials for High-Rate Electrochemical Energy Storage. *Energy & Environmental Science* 2014, 7, 1597-1614.
- [39] Siemens, Energy Storage Module for Mobile and Stationary Applications, w3.siemens.com/smartgrid/global/en/products-systems-solutions/rail-electrification, 06 Mai 2015.
- [40] J. R. Miller & A. F. Burke. Electrochemical Capacitors: Challenges and Opportunities for Real-World Applications. *Electrochemical Society Interface* 2008, 17, 53-57.
- [41] M. Conte. Supercapacitors Technical Requirements for New Applications. *Fuel Cells* 2010, 10, 806-818.
- [42] Maxwell, Cold Cranking Solution, www.maxwell.com/esm/, 06 Mai 2015.
- [43] Continental, Start-Stop Systems, www.continental-corporation.com/www/pressportal_com_en/general/e_mobility, 06 Mai 2015.
- [44] A. Burke. Ultracapacitor Technologies and Application in Hybrid and Electric Vehicles. *International Journal of Energy Research* 2010, 34, 133-151.
- [45] P. Simon, Y. Gogotsi & B. Dunn. Where Do Batteries End and Supercapacitors Begin? *Science* 2014, 343, 1210-1211.
- [46] A. Boisset, L. Athouël, J. Jacquemin, P. Porion, T. Brousse & M. Anouti. Comparative Performances of Birnessite and Cryptomelane MnO₂ as Electrode Material in Neutral Aqueous Lithium Salt for Supercapacitor Application. *The Journal of Physical Chemistry C* 2013, 117, 7408-7422.
- [47] W. Shimizu, S. Makino, K. Takahashi, N. Imanishi & W. Sugimoto. Development of a 4.2 V Aqueous Hybrid Electrochemical Capacitor Based on MnO₂ Positive and Protected Li Negative Electrodes. *Journal of Power Sources* 2013, 241, 572-577.
- [48] M. Okubo, E. Hosono, J. Kim, M. Enomoto, N. Kojima, T. Kudo, H. Zhou & I. Honma. Nanosize Effect on High-Rate Li-Ion Intercalation in LiCoO₂ Electrode. *Journal of the American Chemical Society* 2007, 129, 7444-7452.
- [49] H. E. Becker. U.S. patent 2 800 616 1957.
- [50] D. I. Boos. U.S. patent 3 536 963 1970.
- [51] Maxwell, www.maxwell.com, 06 Mai 2015.
- [52] Nesscap, www.nesscap.com, 06 Mai 2015.
- [53] A. Balakrishnan & K. R. V. Subramanian. Nanostructured Ceramic Oxides for Supercapacitor Applications. *Taylor & Francis*, 2014, Vol. 1, Ch. 1.1.

Bibliography

- [54] E. Frackowiak & F. Béguin. Carbon Materials for the Electrochemical Storage of Energy in Capacitors. *Carbon* 2001, 39, 937-950.
- [55] E. Frackowiak. Carbon Materials for Supercapacitor Application. *Physical Chemistry Chemical Physics* 2007, 9, 1774-1785.
- [56] J. Biener, M. Stadermann, M. Suss, M. A. Worsley, M. M. Biener, K. A. Rose & T. F. Baumann. Advanced Carbon Aerogels for Energy Applications. *Energy & Environmental Science* 2011, 4, 656-667.
- [57] H. Zhang, G. P. Cao & Y. S. Yang. Carbon Nanotube Arrays and Their Composites for Electrochemical Capacitors and Lithium-Ion Batteries. *Energy & Environmental Science* 2009, 2, 932-943.
- [58] C. Vix-Guterl, E. Frackowiak, K. Jurewicz, M. Friebe, J. Parmentier & F. Béguin. Electrochemical Energy Storage in Ordered Porous Carbon Materials. *Carbon* 2005, 43, 1293-1302.
- [59] M. D. Stoller, S. Park, Y. Zhu, J. An & R. S. Ruoff. Graphene-Based Ultracapacitors. *Nano Letters* 2008, 8, 3498-3502.
- [60] J. R. Miller, R. A. Outlaw & B. C. Holloway. Graphene Double-Layer Capacitor with AC Line-Filtering Performance. *Science* 2010, 329, 1637-1639.
- [61] B. E. Conway, V. Birss & J. Wojtowicz. The Role and Utilization of Pseudocapacitance for Energy Storage by Supercapacitors. *Journal of Power Sources* 1997, 66, 1-14.
- [62] S. Trasatti & G. Buzzanca. Ruthenium Dioxide: A New Interesting Electrode Material. Solid State Structure and Electrochemical Behaviour. *Journal of Electroanalytical Chemistry and Interfacial Electrochemistry* 1971, 29, A1-A5.
- [63] M. Toupin, T. Brousse & D. Belanger. Charge Storage Mechanism of MnO₂ Electrode Used in Aqueous Electrochemical Capacitor. *Chemistry of Materials* 2004, 16, 3184-3190.
- [64] D. Beacutelanger, T. Brousse & J. W. Long. Manganese Oxides: Battery Materials Make the Leap to Electrochemical Capacitors. *Electrochemical Society Interface* 2008, 17, 49-52.
- [65] Y. C. Hsieh, K. T. Lee, Y. P. Lin, N. L. Wu & S. W. Donne. Investigation on Capacity Fading of Aqueous MnO₂ Center Dot nH₂O Electrochemical Capacitor. *Journal of Power Sources* 2008, 177, 660-664.
- [66] F. Ataherian, K.-T. Lee & N.-L. Wu. Long-Term Electrochemical Behaviors of Manganese Oxide Aqueous Electrochemical Capacitor Under Reducing Potentials. *Electrochimica Acta* 2010, 55, 7429-7435.
- [67] A. Alonso, V. Ruiz, C. Blanco, R. Santamaría, M. Granda, R. Menéndez & S. G. E. de Jager. Activated Carbon Produced from Sasol-Lurgi Gasifier Pitch and Its Application as Electrodes in Supercapacitors. *Carbon* 2006, 44, 441-446.
- [68] C. O. Ania, V. Khomenko, E. Raymundo-Piñero, J. B. Parra & F. Béguin. The Large Electrochemical Capacitance of Microporous Doped Carbon Obtained by Using a Zeolite Template. *Advanced Functional Materials* 2007, 17, 1828-1836.
- [69] E. Frackowiak & F. Béguin. Electrochemical Storage of Energy in Carbon Nanotubes and Nanostructured Carbons. *Carbon* 2002, 40, 1775-1787.
- [70] M. Kaempgen, C. K. Chan, J. Ma, Y. Cui & G. Gruner. Printable Thin Film Supercapacitors Using Single-Walled Carbon Nanotubes. *Nano Letters* 2009, 9, 1872-1876.
- [71] C. G. Liu, H. T. Fang, D. W. Wang, F. Li, M. Liu & H. M. Cheng. The Electrochemical Capacitance Characteristics of Activated Carbon Electrode

Bibliography

- Material with a Multi-Walled Carbon Nanotube Additive. *New Carbon Materials* 2005, 20, 205-210.
- [72] D. Lozano-Castelló, D. Cazorla-Amorós, A. Linares-Solano, S. Shiraishi, H. Kurihara & A. Oya. Influence of Pore Structure and Surface Chemistry on Electric Double Layer Capacitance in Non-Aqueous Electrolyte. *Carbon* 2003, 41, 1765-1775.
- [73] D. Qu & H. Shi. Studies of Activated Carbons Used in Double-Layer Capacitors. *Journal of Power Sources* 1998, 74, 99-107.
- [74] E. Raymundo-Piñero, K. Kierzek, J. Machnikowski & F. Béguin. Relationship Between the Nanoporous Texture of Activated Carbons and Their Capacitance Properties in Different Electrolytes. *Carbon* 2006, 44, 2498-2507.
- [75] K. S. Xia, Q. M. Gao, J. H. Jiang & J. Hu. Hierarchical Porous Carbons with Controlled Micropores and Mesopores for Supercapacitor Electrode Materials. *Carbon* 2008, 46, 1718-1726.
- [76] H. Yamada, H. Nakamura, F. Nakahara, I. Moriguchi & T. Kudo. Electrochemical Study of High Electrochemical Double Layer Capacitance of Ordered Porous Carbons with Both Meso/Macropores and Micropores. *The Journal of Physical Chemistry C* 2006, 111, 227-233.
- [77] X. H. An, T. J. Simmons, R. Shah, C. Wolfe, K. M. Lewis, M. Washington, S. K. Nayak, S. Talapatra & S. Kar. Stable Aqueous Dispersions of Noncovalently Functionalized Graphene from Graphite and their Multifunctional High-Performance Applications. *Nano Letters* 2010, 10, 4295-4301.
- [78] Y. Chen, X. Zhang, D. Zhang, P. Yu & Y. Ma. High Performance Supercapacitors Based on Reduced Graphene Oxide in Aqueous and Ionic Liquid Electrolytes. *Carbon* 2011, 49, 573-580.
- [79] J. Han, L. L. Zhang, S. Lee, J. Oh, K.-S. Lee, J. R. Potts, J. Ji, X. Zhao, R. S. Ruoff & S. Park. Generation of B-Doped Graphene Nanoplatelets Using a Solution Process and Their Supercapacitor Applications. *ACS Nano* 2012, 7, 19-26.
- [80] M. M. Hantel, T. Kaspar, R. Nesper, A. Wokaun & R. Koetz. Partially Reduced Graphite Oxide for Supercapacitor Electrodes: Effect of Graphene Layer Spacing and Huge Specific Capacitance. *Electrochemistry Communications* 2011, 13, 90-92.
- [81] Z. Lin, Y. Liu, Y. Yao, O. J. Hildreth, Z. Li, K. Moon & C.-p. Wong. Superior Capacitance of Functionalized Graphene. *Journal of Physical Chemistry C* 2011, 115, 7120-7125.
- [82] X. Lu, H. Dou, B. Gao, C. Yuan, S. Yang, L. Hao, L. Shen & X. Zhang. A Flexible Graphene/Multiwalled Carbon Nanotube Film as a High Performance Electrode Material for Supercapacitors. *Electrochimica Acta* 2011, 56, 5115-5121.
- [83] W. Lv, D.-M. Tang, Y.-B. He, C.-H. You, Z.-Q. Shi, X.-C. Chen, C.-M. Chen, P.-X. Hou, C. Liu & Q.-H. Yang. Low-Temperature Exfoliated Graphenes: Vacuum-Promoted Exfoliation and Electrochemical Energy Storage. *ACS Nano* 2009, 3, 3730-3736.
- [84] S. Stankovich, D. A. Dikin, R. D. Piner, K. A. Kohlhaas, A. Kleinhammes, Y. Jia, Y. Wu, S. T. Nguyen & R. S. Ruoff. Synthesis of Graphene-Based Nanosheets via Chemical Reduction of Exfoliated Graphite Oxide. *Carbon* 2007, 45, 1558-1565.
- [85] Y. Xu, K. Sheng, C. Li & G. Shi. Self-Assembled Graphene Hydrogel via a One-Step Hydrothermal Process. *ACS Nano* 2010, 4, 4324-4330.

Bibliography

- [86] X. Yang, J. Zhu, L. Qiu & D. Li. Bioinspired Effective Prevention of Restacking in Multilayered Graphene Films: Towards the Next Generation of High-Performance Supercapacitors. *Advanced Materials* 2011, 23, 2833-2838.
- [87] Y. Zhu, S. Murali, M. D. Stoller, K. J. Ganesh, W. Cai, P. J. Ferreira, A. Pirkle, R. M. Wallace, K. A. Cyhosh, M. Thommes, D. Su, E. A. Stach & R. S. Ruoff. Carbon-Based Supercapacitors Produced by Activation of Graphene. *Science* 2011, 332, 1537-1541.
- [88] Y. Zhu, S. Murali, M. D. Stoller, A. Velamakanni, R. D. Piner & R. S. Ruoff. Microwave Assisted Exfoliation and Reduction of Graphite Oxide for Ultracapacitors. *Carbon* 2010, 48, 2118-2122.
- [89] Y. W. Zhu, M. D. Stoller, W. W. Cai, A. Velamakanni, R. D. Piner, D. Chen & R. S. Ruoff. Exfoliation of Graphite Oxide in Propylene Carbonate and Thermal Reduction of the Resulting Graphene Oxide Platelets. *ACS Nano* 2010, 4, 1227-1233.
- [90] H. F. An, Y. Wang, X. Y. Wang, L. P. Zheng, L. H. Yi, L. Bai & X. Y. Zhang. Polypyrrole/Carbon Aerogel Composite Materials for Supercapacitor. *Journal of Power Sources* 2010, 195, 6964-6969.
- [91] V. Khomenko, E. Frackowiak & F. Béguin. Determination of the Specific Capacitance of Conducting Polymer/Nanotubes Composite Electrodes Using Different Cell Configurations. *Electrochimica Acta* 2005, 50, 2499-2506.
- [92] J. H. Kim, Y. S. Lee, A. K. Sharma & C. G. Liu. Polypyrrole/Carbon Composite Electrode for High-Power Electrochemical Capacitors. *Electrochimica Acta* 2006, 52, 1727-1732.
- [93] H. Li, J. Wang, Q. Chu, Z. Wang, F. Zhang & S. Wang. Theoretical and Experimental Specific Capacitance of Polyaniline in Sulfuric Acid. *Journal of Power Sources* 2009, 190, 578-586.
- [94] W. Li, J. Chen, J. Zhao, J. Zhang & J. Zhu. Application of Ultrasonic Irradiation in Preparing Conducting Polymer as Active Materials for Supercapacitor. *Materials Letters* 2005, 59, 800-803.
- [95] Q. Liu, M. H. Nayfeh & S.-T. Yau. Supercapacitor Electrodes Based on Polyaniline–Silicon Nanoparticle Composite. *Journal of Power Sources* 2010, 195, 3956-3959.
- [96] S. H. Mujawar, S. B. Ambade, T. Battumur, R. B. Ambade & S. H. Lee. Electropolymerization of Polyaniline on Titanium Oxide Nanotubes for Supercapacitor Application. *Electrochimica Acta* 2011, 56, 4462-4466.
- [97] G. A. Snook, P. Kao & A. S. Best. Conducting-Polymer-Based Supercapacitor Devices and Electrodes. *Journal of Power Sources* 2011, 196, 1-12.
- [98] S. K. Tripathi, A. Kumar & S. A. Hashmi. Electrochemical Redox Supercapacitors Using PVdF-HFP Based Gel Electrolytes and Polypyrrole as Conducting Polymer Electrode. *Solid State Ionics* 2006, 177, 2979-2985.
- [99] J. Wang, Y. L. Xu, X. Chen & X. F. Du. Electrochemical Supercapacitor Electrode Material Based on Poly(3,4-Ethylenedioxythiophene)/Polypyrrole Composite. *Journal of Power Sources* 2007, 163, 1120-1125.
- [100] C. Yang & P. Liu. Polypyrrole/Conductive Mica Composites: Preparation, Characterization, and Application in Supercapacitor. *Synthetic Metals* 2010, 160, 768-773.
- [101] K. Zhang, L. L. Zhang, X. S. Zhao & J. Wu. Graphene/Polyaniline Nanofiber Composites as Supercapacitor Electrodes. *Chemistry of Materials* 2010, 22, 1392-1401.

Bibliography

- [102] J.-Y. Kim, K. H. Kim & K. B. Kim. Fabrication and Electrochemical Properties of Carbon Nanotube/Polypyrrole Composite Film Electrodes with Controlled Pore Size. *Journal of Power Sources* 2008, 176, 396-402.
- [103] D. P. Dubal, S. H. Lee, J. G. Kim, W. B. Kim & C. D. Lokhande. Porous Polypyrrole Clusters Prepared by Electropolymerization for a High Performance Supercapacitor. *Journal of Materials Chemistry* 2012, 22, 3044-3052.
- [104] V. Subramanian, H. Zhu, R. Vajtai, P. M. Ajayan & B. Wei. Hydrothermal Synthesis and Pseudocapacitance Properties of MnO₂ Nanostructures. *The Journal of Physical Chemistry B* 2005, 109, 20207-20214.
- [105] M. Xu, L. Kong, W. Zhou & H. Li. Hydrothermal Synthesis and Pseudocapacitance Properties of α -MnO₂ Hollow Spheres and Hollow Urchins. *Journal of Physical Chemistry C Nanometer Interfaces* 2007, 111, 19141-19147.
- [106] P. Yu, X. Zhang, D. Wang, L. Wang & Y. Ma. Shape-Controlled Synthesis of 3D Hierarchical MnO₂ Nanostructures for Electrochemical Supercapacitors. *Crystal Growth & Design* 2009, 9, 528-533.
- [107] K. Kuratani, K. Tatsumi & N. Kuriyama. Manganese Oxide Nanorod with 2 × 4 Tunnel Structure: Synthesis and Electrochemical Properties. *Crystal Growth & Design* 2007, 7, 1375-1377.
- [108] X. Tang, H. Li, Z.-H. Liu, Z. Yang & Z. Wang. Preparation and Capacitive Property of Manganese Oxide Nanobelt Bundles with Birnessite-Type Structure. *Journal of Power Sources* 2011, 196, 855-859.
- [109] S. Chen, J. Zhu, Q. Han, Z. Zheng, Y. Yang & X. Wang. Shape-Controlled Synthesis of One-Dimensional MnO₂ via a Facile Quick-Precipitation Procedure and Its Electrochemical Properties. *Crystal Growth & Design* 2009, 9, 4356.
- [110] S.-L. Chou, J.-Z. Wang, S.-Y. Chew, H.-K. Liu & S.-X. Dou. Electrodeposition of MnO₂ Nanowires on Carbon Nanotube Paper as Free-Standing, Flexible Electrode for Supercapacitors. *Electrochemistry Communications* 2008, 10, 1724-1727.
- [111] C.-L. Xu, S.-J. Bao, L.-B. Kong, H. Li & H.-L. Li. Highly Ordered MnO₂ Nanowire Array Thin Films on Ti/Si Substrate as an Electrode for Electrochemical Capacitor. *Journal of Solid State Chemistry* 2006, 179, 1351-1355.
- [112] W. Xiao, H. Xia, J. Y. H. Fuh & L. Lu. Growth of Single-Crystal α -MnO₂ Nanotubes Prepared by a Hydrothermal Route and Their Electrochemical Properties. *Journal of Power Sources* 2009, 193, 935-938.
- [113] J. Luo, H. T. Zhu, H. M. Fan, J. K. Liang, H. L. Shi, G. H. Rao, J. B. Li, Z. M. Du & Z. X. Shen. Synthesis of Single-Crystal Tetragonal α -MnO₂ Nanotubes. *The Journal of Physical Chemistry C* 2008, 112, 12594-12598.
- [114] Y. Zeng, W. Zhang, C. Xu, N. Xiao, Y. Huang, D. Y. W. Yu, H. H. Hng & Q. Yan. One-Step Solvothermal Synthesis of Single-Crystalline TiOF₂ Nanotubes with High Lithium-Ion Battery Performance. *Chemistry – A European Journal* 2012, 18, 4026-4030.
- [115] H. Xia, J. Feng, H. Wang, M. O. Lai & L. Lu. MnO₂ Nanotube and Nanowire Arrays by Electrochemical Deposition for Supercapacitors. *Journal of Power Sources* 2010, 195, 4410-4413.
- [116] M.-S. Wu, J.-T. Lee, Y.-Y. Wang & C.-C. Wan. Field Emission from Manganese Oxide Nanotubes Synthesized by Cyclic Voltammetric Electrodeposition. *The Journal of Physical Chemistry B* 2004, 108, 16331-16333.
- [117] Q. Li, Z.-L. Wang, G.-R. Li, R. Guo, L.-X. Ding & Y.-X. Tong. Design and Synthesis of MnO₂/Mn/MnO₂ Sandwich-Structured Nanotube Arrays with High

Bibliography

- Supercapacitive Performance for Electrochemical Energy Storage. *Nano Letters* 2012, 12, 3803–3807.
- [118] S. A. Sherrill, J. Duay, Z. Gui, P. Banerjee, G. W. Rubloff & S. B. Lee. MnO₂/TiN Heterogeneous Nanostructure Design for Electrochemical Energy Storage. *Physical Chemistry Chemical Physics* 2011, 13, 15221-15226.
- [119] S. Dong, X. Chen, L. Gu, X. Zhou, L. Li, Z. Liu, P. Han, H. Xu, J. Yao, H. Wang, X. Zhang, C. Shang, G. Cui & L. Chen. One Dimensional MnO₂/Titanium Nitride Nanotube Coaxial Arrays for High Performance Electrochemical Capacitive Energy Storage. *Energy & Environmental Science* 2011, 4, 3502-3508.
- [120] J. Yan, E. Khoo, A. Sumboja & P. S. Lee. Facile Coating of Manganese Oxide on Tin Oxide Nanowires with High-Performance Capacitive Behavior. *ACS Nano* 2010, 4, 4247-4255.
- [121] L. Bao, J. Zang & X. Li. Flexible Zn₂SnO₄/MnO₂ Core/Shell Nanocable–Carbon Microfiber Hybrid Composites for High-Performance Supercapacitor Electrodes. *Nano Letters* 2011, 11, 1215-1220.
- [122] L. G. Xue, H. Hao, Z. Wei, T. Huang & A. S. Yu. A Hierarchical Porous MnO₂-based Electrode for Electrochemical Capacitor. *Journal of Solid State Electrochemistry* 2011, 15, 485-491.
- [123] D. L. Yan, Z. L. Guo, G. S. Zhu, Z. Z. Yu, H. R. Xu & A. B. Yu. MnO₂ Film with Three-Dimensional Structure Prepared by Hydrothermal Process for Supercapacitor. *Journal of Power Sources* 2012, 199, 409-412.
- [124] X. Zhao, L. Zhang, S. Murali, M. D. Stoller, Q. Zhang, Y. Zhu & R. S. Ruoff. Incorporation of Manganese Dioxide within Ultraporous Activated Graphene for High-Performance Electrochemical Capacitors. *ACS Nano* 2012, 6, 5404-5412.
- [125] M. Kim, Y. Hwang & J. Kim. Graphene/MnO₂-Based Composites Reduced via Different Chemical Agents for Supercapacitors. *Journal of Power Sources* 2013, 239, 225-233.
- [126] K.-W. Nam, C.-W. Lee, X.-Q. Yang, B. W. Cho, W.-S. Yoon & K.-B. Kim. Electrodeposited Manganese Oxides on Three-Dimensional Carbon Nanotube Substrate: Supercapacitive Behaviour in Aqueous and Organic Electrolytes. *Journal of Power Sources* 2009, 188, 323-331.
- [127] Y. Zhao, P. Jiang & S.-S. Xie. ZnO-Template-Mediated Synthesis of Three-Dimensional Coral-Like MnO₂ Nanostructure for Supercapacitors. *Journal of Power Sources* 2013, 239, 393-398.
- [128] J. Liu, J. Essner & J. Li. Hybrid Supercapacitor Based on Coaxially Coated Manganese Oxide on Vertically Aligned Carbon Nanofiber Arrays. *Chemistry of Materials* 2010, 22, 5022-5030.
- [129] Z. Yu, B. Duong, D. Abbitt & J. Thomas. Highly Ordered MnO₂ Nanopillars for Enhanced Supercapacitor Performance. *Advanced Materials* 2013, 25, 3302-3306.
- [130] X. Wei, X. Hui, Y. H. F. Jerry & L. Li. Electrophoretic Deposited CNT/MnO₂ Composites for High-Power Electrochemical Energy Storage/Conversion Applications. *Physica Scripta* 2010, 2010, 014008.
- [131] H. Zhao, C. Wang, R. Vellacheri, M. Zhou, Y. Xu, Q. Fu, M. Wu, F. Grote & Y. Lei. Self-Supported Metallic Nanopore Arrays with Highly Oriented Nanoporous Structures as Ideally Nanostructured Electrodes for Supercapacitor Applications. *Advanced Materials* 2014, 26, 7654-7659.

Bibliography

- [132] C. Lin, J. A. Ritter & B. N. Popov. Development of Carbon-Metal Oxide Supercapacitors from Sol-Gel Derived Carbon-Ruthenium Xerogels. *Journal of The Electrochemical Society* 1999, 146, 3155-3160.
- [133] J. W. Long, K. E. Swider, C. I. Merzbacher & D. R. Rolison. Voltammetric Characterization of Ruthenium Oxide-Based Aerogels and other RuO₂ Solids: The Nature of Capacitance in Nanostructured Materials. *Langmuir* 1999, 15, 780-785.
- [134] V. D. Patake, C. D. Lokhande & O. S. Joo. Electrodeposited Ruthenium Oxide Thin Films for Supercapacitor: Effect of Surface Treatments. *Applied Surface Science* 2009, 255, 4192-4196.
- [135] M. Ramani, B. S. Haran, R. E. White, B. N. Popov & L. Arsov. Studies on Activated Carbon Capacitor Materials Loaded with Different Amounts of Ruthenium Oxide. *Journal of Power Sources* 2001, 93, 209-214.
- [136] Z.-S. Wu, D.-W. Wang, W. Ren, J. Zhao, G. Zhou, F. Li & H.-M. Cheng. Anchoring Hydrous RuO₂ on Graphene Sheets for High-Performance Electrochemical Capacitors. *Advanced Functional Materials* 2010, 20, 3595-3602.
- [137] G. Y. Yu, W. X. Chen, Y. F. Zheng, J. Zhao, X. Li & Z. D. Xu. Synthesis of Ru/Carbon Nanocomposites by Polyol Process for Electrochemical Supercapacitor Electrodes. *Materials Letters* 2006, 60, 2453-2456.
- [138] J. R. Zhang, D. C. Jiang, B. Chen, J. J. Zhu, L. P. Jiang & H. Q. Fang. Preparation and Electrochemistry of Hydrous Ruthenium Oxide/Active Carbon Electrode Materials for Supercapacitor. *Journal of The Electrochemical Society* 2001, 148, A1362-A1367.
- [139] J. P. Zheng. Ruthenium Oxide-Carbon Composite Electrodes for Electrochemical Capacitors. *Electrochemical and Solid State Letters* 1999, 2, 359-361.
- [140] J. P. Zheng, P. J. Cygan & T. R. Jow. Hydrous Ruthenium Oxide as an Electrode Material for Electrochemical Capacitors. *Journal of The Electrochemical Society* 1995, 142, 2699-2703.
- [141] J. P. Zheng & T. R. Jow. A New Charge Storage Mechanism for Electrochemical Capacitors. *Journal of The Electrochemical Society* 1995, 142, L6-L8.
- [142] Y. Z. Zheng, H. Y. Ding & M. L. Zhang. Hydrous-Ruthenium-Oxide Thin Film Electrodes Prepared by Cathodic Electrodeposition for Supercapacitors. *Thin Solid Films* 2008, 516, 7381-7385.
- [143] H. Kim & B. N. Popov. Characterization of Hydrous Ruthenium Oxide/Carbon Nanocomposite Supercapacitors Prepared by a Colloidal Method. *Journal of Power Sources* 2002, 104, 52-61.
- [144] Q. Li, X.-F. Lu, H. Xu, Y.-X. Tong & G.-R. Li. Carbon/MnO₂ Double-Walled Nanotube Arrays with Fast Ion and Electron Transmission for High-Performance Supercapacitors. *ACS Applied Materials & Interfaces* 2014, 6, 2726-2733.
- [145] D. Choi & P. N. Kumta. Nanocrystalline TiN Derived by a Two-Step Halide Approach for Electrochemical Capacitors. *Journal of The Electrochemical Society* 2006, 153, A2298-A2303.
- [146] X. Lu, M. Yu, T. Zhai, G. Wang, S. Xie, T. Liu, C. Liang, Y. Tong & Y. Li. High Energy Density Asymmetric Quasi-Solid-State Supercapacitor Based on Porous Vanadium Nitride Nanowire Anode. *Nano Letters* 2013, 13, 2628-2633.
- [147] A. M. Glushenkov, D. Hulicova-Jurcakova, D. Llewellyn, G. Q. Lu & Y. Chen. Structure and Capacitive Properties of Porous Nanocrystalline VN Prepared by Temperature-Programmed Ammonia Reduction of V₂O₅. *Chemistry of Materials* 2010, 22, 914-921.

Bibliography

- [148] S. Dong, X. Chen, L. Gu, X. Zhou, H. Wang, Z. Liu, P. Han, J. Yao, L. Wang, G. Cui & L. Chen. TiN/VN Composites with Core/Shell Structure for Supercapacitors. *Materials Research Bulletin* 2011, 46, 835-839.
- [149] C. M. Ghimbeu, E. Raymundo-Pinero, P. Fioux, F. Beguin & C. Vix-Guterl. Vanadium Nitride/Carbon Nanotube Nanocomposites as Electrodes for Supercapacitors. *Journal of Materials Chemistry* 2011, 21, 13268-13275.
- [150] Y. Yue, P. Han, S. Dong, K. Zhang, C. Zhang, C. Shang & G. Cui. Nanostructured Transition Metal Nitride Composites as Energy Storage Material. *Chinese Science Bulletin* 2012, 57, 4111-4118.
- [151] L. Zhang, C. M. B. Holt, E. J. Luber, B. C. Olsen, H. T. Wang, M. Danaie, X. W. Cui, X. H. Tan, V. W. Lui, W. P. Kalisvaart & D. Mitlin. High Rate Electrochemical Capacitors from Three-Dimensional Arrays of Vanadium Nitride Functionalized Carbon Nanotubes. *Journal of Physical Chemistry C* 2011, 115, 24381-24393.
- [152] Y. Wang, K. Takahashi, K. H. Lee & G. Z. Cao. Nanostructured Vanadium Oxide Electrodes for Enhanced Lithium-Ion Intercalation. *Advanced Functional Materials* 2006, 16, 1133-1144.
- [153] X. Zhou, C. Shang, L. Gu, S. Dong, X. Chen, P. Han, L. Li, J. Yao, Z. Liu, H. Xu, Y. Zhu & G. Cui. Mesoporous Coaxial Titanium Nitride-Vanadium Nitride Fibers of Core-shell Structures for High-Performance Supercapacitors. *ACS Applied Materials & Interfaces* 2011, 3, 3058-3063.
- [154] C. Arbizzani, M. Mastragostino & F. Soavi. New Trends in Electrochemical Supercapacitors. *Journal of Power Sources* 2001, 100, 164-170.
- [155] D. Qu & H. Shi. Studies of Activated Carbons Used in Double-Layer Capacitors. *Journal of Power Sources* 1998, 74, 99-107.
- [156] J. Gamby, P. L. Taberna, P. Simon, J. F. Fauvarque & M. Chesneau. Studies and Characterisations of Various Activated Carbons Used for Carbon/Carbon Supercapacitors. *Journal of Power Sources* 2001, 101, 109-116.
- [157] H. Shi. Activated Carbons and Double Layer Capacitance. *Electrochimica Acta* 1996, 41, 1633-1639.
- [158] G. Salitra, A. Soffer, L. Eliad, Y. Cohen & D. Aurbach. Carbon Electrodes for Double-Layer Capacitors I. Relations Between Ion and Pore Dimensions. *Journal of The Electrochemical Society* 2000, 147, 2486-2493.
- [159] C. Largeot, C. Portet, J. Chmiola, P. L. Taberna, Y. Gogotsi & P. Simon. Relation Between the Ion Size and Pore Size for an Electric Double-Layer Capacitor. *Journal of the American Chemical Society* 2008, 130, 2730-2731.
- [160] A. K. Geim & K. S. Novoselov. The Rise of Graphene. *Nature Materials* 2007, 6, 183-191.
- [161] V. Georgakilas, M. Otyepka, A. B. Bourlinos, V. Chandra, N. Kim, K. C. Kemp, P. Hobza, R. Zboril & K. S. Kim. Functionalization of Graphene: Covalent and Non-Covalent Approaches, Derivatives and Applications. *Chemical Reviews* 2012, 112, 6156-6214.
- [162] Nobelprize.org, The Nobel Prize in Physics 2010, www.nobelprize.org/nobel_prizes/physics/laureates/2010/, 06 Mai 2015.
- [163] Y. Huang, J. Liang & Y. Chen. An Overview of the Applications of Graphene-Based Materials in Supercapacitors. *Small* 2012, 8, 1805-1834.
- [164] A. Davies & A. Yu. Material Advancements in Supercapacitors: From Activated Carbon to Carbon Nanotube and Graphene. *The Canadian Journal of Chemical Engineering* 2011, 89, 1342-1357.

Bibliography

- [165] R. Vellacheri, A. Al-Haddad, H. Zhao, W. Wang, C. Wang & Y. Lei. High Performance Supercapacitor for Efficient Energy Storage Under Extreme Environmental Temperatures. *Nano Energy* 2014, 8, 231-237.
- [166] K. Sheng, Y. Sun, C. Li, W. Yuan & G. Shi. Ultrahigh-Rate Supercapacitors based on Electrochemically Reduced Graphene Oxide for AC Line-Filtering. *Scientific Report* 2012, 2, 247.
- [167] Y. Si & E. T. Samulski. Exfoliated Graphene Separated by Platinum Nanoparticles. *Chemistry of Materials* 2008, 20, 6792-6797.
- [168] L. Weinstein & R. Dash. Supercapacitor Carbons. *Materials Today* 2013, 16, 356-357.
- [169] R. Kötz & M. Carlen. Principles and Applications of Electrochemical Capacitors. *Electrochimica Acta* 2000, 45, 2483-2498.
- [170] L. Nyholm, G. Nyström, A. Mihranyan & M. Strømme. Toward Flexible Polymer and Paper-Based Energy Storage Devices. *Advanced Materials* 2011, 23, 3751-3769.
- [171] K. Naoi & P. Simon. New Materials and New Configurations for Advanced Electrochemical Capacitors. *Electrochemical Society Interface* 2008, 17, 34-37.
- [172] J. H. Park, J. M. Ko & O. O. Park. Carbon Nanotube/RuO₂ Nanocomposite Electrodes for Supercapacitors. *Journal of The Electrochemical Society* 2003, 150, A864-A867.
- [173] H. Y. Lee & J. B. Goodenough. Supercapacitor Behavior with KCl Electrolyte. *Journal of Solid State Chemistry* 1999, 144, 220-223.
- [174] S. Devaraj & N. Munichandraiah. Effect of Crystallographic Structure of MnO₂ on Its Electrochemical Capacitance Properties. *The Journal of Physical Chemistry C* 2008, 112, 4406-4417.
- [175] K. Chen, Y. Dong Noh, K. Li, S. Komarneni & D. Xue. Microwave-Hydrothermal Crystallization of Polymorphic MnO₂ for Electrochemical Energy Storage. *The Journal of Physical Chemistry C* 2013, 117, 10770-10779.
- [176] L. Peng, X. Peng, B. Liu, C. Wu, Y. Xie & G. Yu. Ultrathin Two-Dimensional MnO₂/Graphene Hybrid Nanostructures for High-Performance, Flexible Planar Supercapacitors. *Nano Letters* 2013, 13, 2151-2157.
- [177] J.-K. Chang & W.-T. Tsai. Material Characterization and Electrochemical Performance of Hydrous Manganese Oxide Electrodes for Use in Electrochemical Pseudocapacitors. *Journal of The Electrochemical Society* 2003, 150, A1333-A1338.
- [178] X. Lang, A. Hirata, T. Fujita & M. Chen. Nanoporous Metal/Oxide Hybrid Electrodes for Electrochemical Supercapacitors. *Nature Nanotechnology* 2011, 6, 232-236.
- [179] X. Lu, G. Wang, T. Zhai, M. Yu, J. Gan, Y. Tong & Y. Li. Hydrogenated TiO₂ Nanotube Arrays for Supercapacitors. *Nano Letters* 2012, 12, 1690-1696.
- [180] X. Lu, M. Yu, G. Wang, T. Zhai, S. Xie, Y. Ling, Y. Tong & Y. Li. H-TiO₂@MnO₂/H-TiO₂@C Core-Shell Nanowires for High Performance and Flexible Asymmetric Supercapacitors. *Advanced Materials* 2012, 25, 267-272.
- [181] H. Xia, D. Zhu, Z. Luo, Y. Yu, X. Shi, G. Yuan & J. Xie. Hierarchically Structured Co₃O₄@Pt@MnO₂ Nanowire Arrays for High-Performance Supercapacitors. *Scientific Reports* 2013, 3, 2978.
- [182] T. C. Liu, W. G. Pell, B. E. Conway & S. L. Roberson. Behavior of Molybdenum Nitrides as Materials for Electrochemical Capacitors - Comparison with Ruthenium Oxide. *Journal of The Electrochemical Society* 1998, 145, 1882-1888.

Bibliography

- [183] Y. H. Yue, P. X. Han, S. M. Dong, K. J. Zhang, C. J. Zhang, C. Q. Shang & G. L. Cui. Nanostructured Transition Metal Nitride Composites as Energy Storage Material. *Chinese Science Bulletin* 2012, 57, 4111-4118.
- [184] X. H. Zhou, C. Q. Shang, L. Gu, S. M. Dong, X. Chen, P. X. Han, L. F. Li, J. H. Yao, Z. H. Liu, H. X. Xu, Y. W. Zhu & G. L. Cui. Mesoporous Coaxial Titanium Nitride-Vanadium Nitride Fibers of Core-Shell Structures for High-Performance Supercapacitors. *ACS Applied Materials & Interfaces* 2011, 3, 3058-3063.
- [185] X. Lu, G. Wang, T. Zhai, M. Yu, S. Xie, Y. Ling, C. Liang, Y. Tong & Y. Li. Stabilized TiN Nanowire Arrays for High-Performance and Flexible Supercapacitors. *Nano Letters* 2012, 12, 5376-5381.
- [186] X. Lu, T. Liu, T. Zhai, G. Wang, M. Yu, S. Xie, Y. Ling, C. Liang, Y. Tong & Y. Li. Improving the Cycling Stability of Metal-Nitride Supercapacitor Electrodes with a Thin Carbon Shell. *Advanced Energy Materials* 2014, 4, 1300994.
- [187] S. Sopčić, R. Peter, M. Petravić & Z. Mandić. New Insights Into the Mechanism of Pseudocapacitance Deterioration in Electrodeposited MnO₂ Under Negative Potentials. *Journal of Power Sources* 2013, 240, 252-257.
- [188] T. Brousse, M. Toupin & D. Belanger. A Hybrid Activated Carbon-Manganese Dioxide Capacitor Using a Mild Aqueous Electrolyte. *Journal of The Electrochemical Society* 2004, 151, A614-A622.
- [189] M. S. Hong, S. H. Lee & S. W. Kim. Use of KCl Aqueous Electrolyte for 2 V Manganese Oxide/Activated Carbon Hybrid Capacitor *Electrochemical and Solid State Letters* 2002, 5, A227-A230
- [190] T. Cottineau, M. Toupin, T. Delahaye, T. Brousse & D. Belanger. Nanostructured Transition Metal Oxides for Aqueous Hybrid Electrochemical Supercapacitors. *Applied Physics a-Materials Science & Processing* 2006, 82, 599-606.
- [191] K. H. Reiman, K. M. Brace, T. J. Gordon-Smith, I. Nandhakumar, G. S. Attard & J. R. Owen. Lithium Insertion into TiO₂ from Aqueous Solution - Facilitated by Nanostructure. *Electrochemistry Communications* 2006, 8, 517-522.
- [192] L. H. Lu, Y. D. Zhu, F. J. Li, W. Zhuang, K. Y. Chan & X. H. Lu. Carbon Titania Mesoporous Composite Whisker as Stable Supercapacitor Electrode Material. *Journal of Materials Chemistry* 2010, 20, 7645-7651.
- [193] T. Brousse & D. Belanger. A Hybrid Fe₃O₄-MnO₂ Capacitor in Mild Aqueous Electrolyte. *Electrochemical and Solid State Letters* 2003, 6, A244-A248.
- [194] M. B. Sassin, A. N. Mansour, K. A. Pettigrew, D. R. Rolison & J. W. Long. Electroless Deposition of Conformal Nanoscale Iron Oxide on Carbon Nanoarchitectures for Electrochemical Charge Storage. *ACS Nano* 2010, 4, 4505-4514.
- [195] C. Guan, J. Liu, Y. Wang, L. Mao, Z. Fan, Z. Shen, H. Zhang & J. Wang. Iron Oxide-Decorated Carbon for Supercapacitor Anodes with Ultrahigh Energy Density and Outstanding Cycling Stability. *ACS Nano* 2015, 9, 5198-5207.
- [196] J. Chang, M. Jin, F. Yao, T. H. Kim, V. T. Le, H. Yue, F. Gunes, B. Li, A. Ghosh, S. Xie & Y. H. Lee. Asymmetric Supercapacitors Based on Graphene/MnO₂ Nanospheres and Graphene/MoO₃ Nanosheets with High Energy Density. *Advanced Functional Materials* 2013, 23, 5074-5083.
- [197] Y. P. Wu, Y. Liu, B. Zhang, Y. Yang, Z. Chang & Z. W. Zhubiao Wen. Polypyrrole-Coated α -MoO₃ Nanobelts with Good Electrochemical Performance as Anode Material for Aqueous Supercapacitor. *Journal of Materials Chemistry A* 2013, 1, 13582-13587.

Bibliography

- [198] E. Eustache, R. Frappier, R. L. Porto, S. Bouhtiyya, J.-F. Pierson & T. Brousse. Asymmetric Electrochemical Capacitor Microdevice Designed with Vanadium Nitride and Nickel Oxide Thin Film Electrodes. *Electrochemistry Communications* 2013, 28, 104-106.
- [199] K. Naoi & M. Morita. Advanced Polymers as Active Materials and Electrolytes for Electrochemical Capacitors and Hybrid Capacitor Systems. *Electrochemical Society Interface* 2008, 17, 44-48.
- [200] V. Khomenko, E. Raymundo-Pinero, E. Frackowiak & F. Beguin. High-Voltage Asymmetric Supercapacitors Operating in Aqueous Electrolyte. *Applied Physics a-Materials Science & Processing* 2006, 82, 567-573.
- [201] H. A. Andreas & B. E. Conway. Examination of the Double-Layer Capacitance of an High Specific-Area C-Cloth Electrode as Titrated from Acidic to Alkaline pHs. *Electrochimica Acta* 2006, 51, 6510-6520.
- [202] F. Wang, S. Xiao, Y. Hou, C. Hu, L. Liu & Y. Wu. Electrode Materials for Aqueous Asymmetric Supercapacitors. *RSC Advances* 2013, 3, 13059-13084.
- [203] J. Duay, E. Gillette, R. Liu & S. B. Lee. Highly Flexible Pseudocapacitor Based on Freestanding Heterogeneous MnO₂/Conductive Polymer Nanowire Arrays. *Physical Chemistry Chemical Physics* 2012, 14, 3329-3337.
- [204] W. Xing, S. Z. Qiao, R. G. Ding, F. Li, G. Q. Lu, Z. F. Yan & H. M. Cheng. Superior Electric Double Layer Capacitors Using Ordered Mesoporous Carbons. *Carbon* 2006, 44, 216-224.
- [205] D.-W. Wang, F. Li, M. Liu, G. Q. Lu & H.-M. Cheng. 3D Aperiodic Hierarchical Porous Graphitic Carbon Material for High-Rate Electrochemical Capacitive Energy Storage. *Angewandte Chemie International Edition* 2008, 47, 373-376.
- [206] E. Raymundo-Piñero, F. Leroux & F. Béguin. A High-Performance Carbon for Supercapacitors Obtained by Carbonization of a Seaweed Biopolymer. *Advanced Materials* 2006, 18, 1877-1882.
- [207] T. Brousse, P.-L. Taberna, O. Crosnier, R. Dugas, P. Guillemet, Y. Scudeller, Y. Zhou, F. Favier, D. Bélanger & P. Simon. Long-term Cycling Behavior of Asymmetric Activated Carbon/MnO₂ Aqueous Electrochemical Supercapacitor. *Journal of Power Sources* 2007, 173, 633-641.
- [208] A. Malak, K. Fic, G. Lota, C. Vix-Guterl & E. Frackowiak. Hybrid Materials for Supercapacitor Application. *Journal of Solid State Electrochemistry* 2010, 14, 811-816.
- [209] Y. Xue, Y. Chen, M. L. Zhang & Y. D. Yan. A New Asymmetric Supercapacitor Based on Lambda-MnO₂ and Activated Carbon Electrodes. *Materials Letters* 2008, 62, 3884-3886.
- [210] Z. Lei, J. Zhang & X. S. Zhao. Ultrathin MnO₂ Nanofibers Grown on Graphitic Carbon Spheres as High-Performance Asymmetric Supercapacitor Electrodes. *Journal of Materials Chemistry* 2012, 22, 153-160.
- [211] Y. Cheng, H. Zhang, S. Lu, C. V. Varanasi & J. Liu. Flexible Asymmetric Supercapacitors with High Energy and High Power Density in Aqueous Electrolytes. *Nanoscale* 2013, 5, 1067-1073.
- [212] J.-G. Wang, Y. Yang, Z.-H. Huang & F. Kang. A High-Performance Asymmetric Supercapacitor Based on Carbon and Carbon-MnO₂ Nanofiber Electrodes. *Carbon* 2013, 61, 190-199.
- [213] Z.-S. Wu, W. Ren, D.-W. Wang, F. Li, B. Liu & H.-M. Cheng. High-Energy MnO₂ Nanowire/Graphene and Graphene Asymmetric Electrochemical Capacitors. *ACS Nano* 2010, 4, 5835-5842.

Bibliography

- [214] Q. Cheng, J. Tang, J. Ma, H. Zhang, N. Shinya & L.-C. Qin. Graphene and Nanostructured MnO₂ Composite Electrodes for Supercapacitors. *Carbon* 2011, 49, 2917-2925.
- [215] A. Burke & M. Miller. The Power Capability of Ultracapacitors and Lithium Batteries for Electric and Hybrid Vehicle Applications. *Journal of Power Sources* 2011, 196, 514-522.
- [216] Z. Gan, Y. Cao, R. A. Evans & M. Gu. Three-Dimensional Deep Sub-Diffraction Optical Beam Lithography with 9 nm Feature Size. *Nature Communication* 2013, 4, 2061.
- [217] S. Jeon, V. Malyarchuk, J. A. Rogers & G. P. Wiederrecht. Fabricating Three-Dimensional Nanostructures Using Two Photon Lithography in a Single Exposure Step. *Optics Express* 2006, 14, 2300-2308.
- [218] Nanoscribe, 3D Laser Lithography, www.nanoscribe.de, 06 Mai 2015.
- [219] D. Jang, L. R. Meza, F. Greer & J. R. Greer. Fabrication and Deformation of Three-Dimensional Hollow Ceramic Nanostructures. *Nature Materials* 2013, 12, 893–898.
- [220] S.-H. Kim, S. Y. Lee, S.-M. Yang & G.-R. Yi. Self-Assembled Colloidal Structures for Photonics. *NPG Asia Mater* 2011, 3, 25-33.
- [221] Y. Ke, L. L. Ong, W. M. Shih & P. Yin. Three-Dimensional Structures Self-Assembled from DNA Bricks. *Science* 2012, 338, 1177-1183.
- [222] J. J. Cole, E.-C. Lin, C. R. Barry & H. O. Jacobs. Continuous Nanoparticle Generation and Assembly by Atmospheric Pressure Arc Discharge. *Applied Physics Letters* 2009, 95, 113101.
- [223] H. O. Jacobs, S. A. Campbell & M. G. Steward. Approaching Nanoxerography: The Use of Electrostatic Forces to Position Nanoparticles with 100 nm Scale Resolution. *Advanced Materials* 2002, 14, 1553-1557.
- [224] Y. Lei, W. Cai & G. Wilde. Highly Ordered Nanostructures with Tunable Size, Shape and Properties: A New Way to Surface Nano-Patterning Using Ultra-Thin Alumina Masks. *Progress in Materials Science* 2007, 52, 465-539.
- [225] Y. Lei, S. Yang, M. Wu & G. Wilde. Surface Patterning Using Templates: Concept, Properties and Device Applications. *Chemical Society Reviews* 2011, 40, 1247-1258.
- [226] G. Subramanian, V. N. Manoharan, J. D. Thorne & D. J. Pine. Ordered Macroporous Materials by Colloidal Assembly: A Possible Route to Photonic Bandgap Materials. *Advanced Materials* 1999, 11, 1261-1265.
- [227] M. Zhou, J. Bao, Y. Xu, J. Zhang, J. Xie, M. Guan, C. Wang, L. Wen, Y. Lei & Y. Xie. Photoelectrodes Based upon Mo:BiVO₄ Inverse Opals for Photoelectrochemical Water Splitting. *ACS Nano* 2014, 8, 7088-7098.
- [228] G. Recio-Sánchez, V. Torres-Costa, M. Manso-Silván & R. J. Martín-Palma. Nanostructured Porous Silicon Photonic Crystal for Applications in the Infrared. *Journal of Nanotechnology* 2012, 1-6.
- [229] W. Zhou & Z. L. Wang. Three-Dimensional Nanoarchitectures: Designing Next-Generation Devices. *Springer*, 2011.
- [230] Y. Tachibana, L. Vayssieres & J. R. Durrant. Artificial Photosynthesis for Solar Water-Splitting. *Nature Photonics* 2012, 6, 511-518.
- [231] Z. Fan, H. Razavi, J.-w. Do, A. Moriwaki, O. Ergen, Y.-L. Chueh, P. W. Leu, J. C. Ho, T. Takahashi, L. A. Reichertz, S. Neale, K. Yu, M. Wu, J. W. Ager & A. Javey. Three-Dimensional Nanopillar-Array Photovoltaics on Low-Cost and Flexible Substrates. *Nature Materials* 2009, 8, 648-653.

Bibliography

- [232] D. Golodnitsky, V. Yufit, M. Nathan, I. Shechtman, T. Ripenbein, E. Strauss, S. Menkin & E. Peled. Advanced Materials for the 3D Microbattery. *Journal of Power Sources* 2006, 153, 281 - 287.
- [233] S. C. Pang, M. A. Anderson & T. W. Chapman. Novel Electrode Materials for Thin-Film Ultracapacitors: Comparison of Electrochemical Properties of Sol-Gel-Derived and Electrodeposited Manganese Dioxide. *Journal of The Electrochemical Society* 2000, 147, 444-450.
- [234] Z.-L. Wang, R. Guo, L.-X. Ding, Y.-X. Tong & G.-R. Li. Controllable Template-Assisted Electrodeposition of Single- and Multi-Walled Nanotube Arrays for Electrochemical Energy Storage. *Science Reports* 2013, 3.
- [235] J. Liu, J. Jiang, M. Bosman & H. J. Fan. Three-Dimensional Tubular Arrays of MnO₂-NiO Nanoflakes with High Areal Pseudocapacitance. *Journal of Materials Chemistry* 2012, 22, 2419-2426.
- [236] L. L. Zhang, S. Li, J. Zhang, P. Guo, J. Zheng & X. S. Zhao. Enhancement of Electrochemical Performance of Macroporous Carbon by Surface Coating of Polyaniline. *Chemistry of Materials* 2009, 22, 1195-1202.
- [237] J. Duay, E. Gillette, J. Hu & S. B. Lee. Controlled Electrochemical Deposition and Transformation of Hetero-Nanoarchitected Electrodes for Energy Storage. *Physical Chemistry Chemical Physics* 2013, 15, 7976-7993.
- [238] G. Yu, L. Hu, M. Vosgueritchian, H. Wang, X. Xie, J. R. McDonough, X. Cui, Y. Cui & Z. Bao. Solution-Processed Graphene/MnO₂ Nanostructured Textiles for High-Performance Electrochemical Capacitors. *Nano Letters* 2011, 11, 2905-2911.
- [239] T. Suntola & J. Antson. U.S. patent 4058430 1977.
- [240] T. Suntola, A. Pakkala & S. Lindfors. U.S. patent 438997 1983.
- [241] M. Knez, K. Niesch & L. Niinisto. Synthesis and Surface Engineering of Complex Nanostructures by Atomic Layer Deposition. *Advanced Materials* 2007, 19, 3425-3438.
- [242] P. Banerjee, I. Perez, L. Henn-Lecordier, S. B. Lee & G. W. Rubloff. Nanotubular Metal-Insulator-Metal Capacitor Arrays for Energy Storage. *Nature Nanotechnology* 2009, 4, 292-296.
- [243] L. C. Haspert, S. B. Lee & G. W. Rubloff. Nanoengineering Strategies for Metal-Insulator-Metal Electrostatic Nanocapacitors. *ACS Nano* 2012, 6, 3528-3536.
- [244] L. Wen, Y. Mi, C. Wang, Y. Fang, F. Grote, H. Zhao, M. Zhou & Y. Lei. Cost-effective Atomic Layer Deposition Synthesis of Pt Nanotube Arrays: Application for High Performance Supercapacitor. *Small* 2014, 10, 3162-3168.
- [245] J. Hämäläinen, M. Ritala & M. Leskelä. Atomic Layer Deposition of Noble Metals and Their Oxides. *Chemistry of Materials* 2013, 26, 786-801.
- [246] T. Aaltonen, M. Ritala, T. Sajavaara, J. Keinonen & M. Leskela. Atomic Layer Deposition of Platinum Thin Films. *Chemistry of Materials* 2003, 15, 1924-1928.
- [247] B. S. Lim, A. Rahtu & R. G. Gordon. Atomic Layer Deposition of Transition Metals. *Nature Materials* 2003, 2, 749-754.
- [248] T. Aaltonen, M. Ritala, V. Sammelselg & M. Leskela. Atomic Layer Deposition of Iridium Thin Films. *Journal of The Electrochemical Society* 2004, 151, 489-492.
- [249] T. Aaltonen, P. Alen, M. Ritala & M. Leskela. Ruthenium Thin Films Grown by Atomic Layer Deposition. *Chemical Vapor Deposition* 2003, 9, 45-49.
- [250] L. Niinistö, M. Nieminen, J. Päiväsari, J. Niinistö & M. Putkonen. Advanced Electronic and Optoelectronic Materials by Atomic Layer Deposition: An Overview

Bibliography

- With Special Emphasis on Recent Progress in Processing of High-K Dielectrics and Other Oxide Materials. *physica status solidi (a)* 2004, 201, 1443-1452.
- [251] X. Meng, Y. Zhang, S. Sun, R. Li & X. Sun. Three Growth Modes and Mechanisms for Highly Structure-Tunable SnO₂ Nanotube Arrays of Template-Directed Atomic Layer Deposition. *Journal of Materials Chemistry* 2011, 21, 12321-12330.
- [252] A. Rosental, A. Tarre, A. Gerst, T. Uustare & V. Sammelselg. Atomic-Layer Chemical Vapor Deposition of SnO₂ for Gas-Sensing Applications. *Sensors and Actuators B: Chemical* 2001, 77, 297-300.
- [253] R. L. Puurunen. Surface Chemistry of Atomic Layer Deposition: A Case Study for the Trimethylaluminum/Water Process. *Journal of Applied Physics* 2005, 97, 121301-121301-121352.
- [254] M. Leskelä & M. Ritala. Atomic Layer Deposition Chemistry: Recent Developments and Future Challenges. *Angewandte Chemie International Edition* 2003, 42, 5548-5554.
- [255] Y. S. Kim & S. J. Yun. Studies on Polycrystalline ZnS Thin Films Grown by Atomic Layer Deposition for Electroluminescent Applications. *Applied Surface Science* 2004, 229, 105-111.
- [256] L. Reijnen, B. Meester, A. Goossens & J. Schoonman. Atomic Layer Deposition of Cu_xS for Solar Energy Conversion. *Chemical Vapor Deposition* 2003, 9, 15-20.
- [257] X. Meng, J. A. Libera, T. T. Fister, H. Zhou, J. K. Hedlund, P. Fenter & J. W. Elam. Atomic Layer Deposition of Gallium Sulfide Films Using Hexakis(dimethylamido)digallium and Hydrogen Sulfide. *Chemistry of Materials* 2014, 26, 1029-1039.
- [258] J. Musschoot, Q. Xie, D. Deduytsche, S. Van den Berghe, R. L. Van Meirhaeghe & C. Detavernier. Atomic Layer Deposition of Titanium Nitride from TDMAT Precursor. *Microelectronic Engineering* 2009, 86, 72-77.
- [259] J. S. Park, H. S. Park & S. W. Kang. Plasma-Enhanced Atomic Layer Deposition of Ta-N Thin Films. *Journal of The Electrochemical Society* 2002, 149, C28-C32.
- [260] A. Rugge, J. S. Becker, R. G. Gordon & S. H. Tolbert. Tungsten Nitride Inverse Opals by Atomic Layer Deposition. *Nano Letters* 2003, 3, 1293-1297.
- [261] C. H. Ahn, S. G. Cho, H. J. Lee, K. H. Park & S. H. Jeong. Characteristics of TiN Thin Films Grown by ALD Using TiCl₄ and NH₃. *Metals and Materials International* 2001, 7, 621-625.
- [262] M. Ritala, M. Leskelä, E. Rauhala & P. Haussalo. Atomic Layer Epitaxy Growth of TiN Thin Films. *Journal of The Electrochemical Society* 1995, 142, 2731-2737.
- [263] H. Kim, H. B. R. Lee & W. J. Maeng. Applications of Atomic Layer Deposition to Nanofabrication and Emerging Nanodevices. *Thin Solid Films* 2009, 517, 2563-2580.
- [264] T. Suntola. Handbook of Crystal Growth 3 Thin Films and Epitaxy, Part B: Growth Mechanisms and Dynamics. *Elsevier Science Publishers*, 1994, Vol. 3, Ch. 14.
- [265] M. Ylilammi. Monolayer Thickness in Atomic Layer Deposition. *Thin Solid Films* 1996, 279, 124-130.
- [266] R. L. Puurunen. Growth per Cycle in Atomic Layer Deposition: A Theoretical Model. *Chemical Vapor Deposition* 2003, 9, 249-257.
- [267] F. Keller, M. S. Hunter & D. L. Robinson. Structural Features of Oxide Coatings on Aluminum. *Journal of The Electrochemical Society* 1953, 100, 411-419.
- [268] Z. Su & W. Zhou. Formation Mechanism of Porous Anodic Aluminium and Titanium Oxides. *Advanced Materials* 2008, 20, 3663-3667.

Bibliography

- [269] K. Nielsch, J. Choi, K. Schwirn, R. B. Wehrspohn & U. Gösele. Self-Ordering Regimes of Porous Alumina: The 10 % Porosity Rule. *Nano Letters* 2002, 2, 677-680.
- [270] Z. Su, G. Hahner & W. Zhou. Investigation of the Pore Formation in Anodic Aluminium Oxide. *Journal of Materials Chemistry* 2008, 18, 5787-5795.
- [271] O. Jessensky, F. Müller & U. Gösele. Self-Organized Formation of Hexagonal Pore Arrays in Anodic Alumina. *Applied Physics Letters* 1998, 72, 1173-1175.
- [272] A. Li, F. Müller, A. Birner, K. Nielsch & U. Gösele. Hexagonal Pore Arrays with a 50-420 nm Interpore Distance Formed by Self-Organization in Anodic Alumina. *Journal of Applied Physics* 1998, 84, 6023-6026.
- [273] W. Lee, R. Ji, U. Gösele & K. Nielsch. Fast Fabrication of Long-Range Ordered Porous Alumina Membranes by Hard Anodization. *Nature Materials* 2006, 5, 741-747.
- [274] Eftekhari. Nanostructured Materials in Electrochemistry. *John Wiley & Sons*, 2008.
- [275] J. P. O'Sullivan & G. C. Wood. The Morphology and Mechanism of Formation of Porous Anodic Films on Aluminium. *Proceedings of the Royal Society of London. Series A, Mathematical and Physical Sciences* 1970, 317, 511-543.
- [276] H. Asoh, K. Nishio, M. Nakao, T. Tamamura & H. Masuda. Conditions for Fabrication of Ideally Ordered Anodic Porous Alumina Using Pretextured Al. *Journal of The Electrochemical Society* 2001, 148, B152-B156.
- [277] J. W. Diggle, T. C. Downie & C. W. Goulding. Anodic Oxide Films on Aluminum. *Chemical Reviews* 1969, 69, 365-405.
- [278] H. Masuda & K. Fukuda. Ordered Metal Nanohole Arrays Made By A 2-Step Replication of Honeycomb Structures of Anodic Alumina. *Science* 1995, 268, 1466-1468.
- [279] H. Masuda & M. Satoh. Fabrication of Gold Nanodot Array Using Anodic Porous Alumina as an Evaporation Mask. *Japanese Journal of Applied Physics* 1996, 35, L126.
- [280] H. Masuda, F. Hasegawa & S. Ono. Self-Ordering of Cell Arrangement of Anodic Porous Alumina Formed in Sulfuric Acid Solution. *Journal of The Electrochemical Society* 1997, 144, L127-L130.
- [281] Y. Lei, Z. Jiao, M. Wu & G. Wilde. Ordered Arrays of Nanostructures and Applications in High-Efficient Nano-Generators. *Advanced Engineering Materials* 2007, 9, 343-348.
- [282] S. Mátéfi-Tempfli, M. Mátéfi-Tempfli & L. Piraux. Characterization of Nanopores Ordering in Anodic Alumina. *Thin Solid Films* 2008, 516, 3735-3740.
- [283] M. Wu, L. Wen, Y. Lei, S. Ostendorp, K. Chen & G. Wilde. Ultrathin Alumina Membranes for Surface Nanopatterning in Fabricating Quantum-Sized Nanodots. *Small* 2010, 6, 695-699.
- [284] Y. Lei, C. H. Liang, Y. C. Wu, L. D. Zhang & Y. Q. Mao. Preparation of Highly Ordered Nanoporous Co Membranes Assembled by Small Quantum-Sized Co Particles. *Journal of Vacuum Science & Technology B* 2001, 19, 1109-1114.
- [285] W. Lee & S.-J. Park. Porous Anodic Aluminum Oxide: Anodization and Templated Synthesis of Functional Nanostructures. *Chemical Reviews* 2014, 114, 7487-7556.
- [286] W. Lee, K. Schwirn, M. Steinhart, E. Pippel, R. Scholz & U. Gosele. Structural Engineering of Nanoporous Anodic Aluminium Oxide by Pulse Anodization of Aluminium. *Nature Nanotechnology* 2008, 3, 234-239.

Bibliography

- [287] H. Masuda, H. Asoh, M. Watanabe, K. Nishio, M. Nakao & T. Tamamura. Square and Triangular Nanohole Array Architectures in Anodic Alumina. *Advanced Materials* 2001, 13, 189-192.
- [288] J. Bradbury. Nature's Nanotechnologists: Unveiling the Secrets of Diatoms. *PLoS Biology* 2004, 2, 1512.
- [289] J. Zi, X. Yu, Y. Li, X. Hu, C. Xu, X. Wang, X. Liu & R. Fu. Coloration Strategies in Peacock Feathers. *Proceedings of the National Academy of Sciences* 2003, 100, 12576-12578.
- [290] T. Ozel, G. R. Bourret & C. A. Mirkin. Coaxial Lithography. *Nature Nanotechnology* 2015, 10, 319-324.
- [291] N. Winkler, J. Leuthold, Y. Lei & G. Wilde. Large-Scale Highly Ordered Arrays of Freestanding Magnetic Nanowires. *Journal of Materials Chemistry* 2012, 22, 16627-16632.
- [292] K. Nielsch, F. Müller, A. P. Li & U. Gösele. Uniform Nickel Deposition into Ordered Alumina Pores by Pulsed Electrodeposition. *Advanced Materials* 2000, 12, 582-586.
- [293] C. Mu, Y. X. Yu, R. M. Wang, K. Wu, D. S. Xu & G. L. Guo. Uniform Metal Nanotube Arrays by Multistep Template Replication and Electrodeposition. *Advanced Materials* 2004, 16, 1550-1553.
- [294] G. Meng, Y. J. Jung, A. Cao, R. Vajtai & P. M. Ajayan. Controlled Fabrication of Hierarchically Branched Nanopores, Nanotubes, and Nanowires. *Proceedings of the National Academy of Sciences of the United States of America* 2005, 102, 7074-7078.
- [295] H. Q. Cao, Z. Xu, H. Sang, D. Sheng & C. Y. Tie. Template Synthesis and Magnetic Behavior of an Array of Cobalt Nanowires Encapsulated in Polyaniline Nanotubules. *Advanced Materials* 2001, 13, 121-123.
- [296] Z. Zhan & Y. Lei. Sub-100-nm Nanoparticle Arrays with Perfect Ordering and Tunable and Uniform Dimensions Fabricated by Combining Nanoimprinting with Ultrathin Alumina Membrane Technique. *ACS Nano* 2014, 8, 3862-3868.
- [297] D. Routkevitch, T. Bigioni, M. Moskovits & J. M. Xu. Electrochemical Fabrication of CdS Nanowire Arrays in Porous Anodic Aluminum Oxide Templates. *The Journal of Physical Chemistry* 1996, 100, 14037-14047.
- [298] Y. Lei, L. D. Zhang, G. W. Meng, G. H. Li, X. Y. Zhang, C. H. Liang, W. Chen & S. X. Wang. Preparation and Photoluminescence of Highly Ordered TiO₂ Nanowire Arrays. *Applied Physics Letters* 2001, 78, 1125-1127.
- [299] Y. Lei, L. D. Zhang & J. C. Fan. Fabrication, Characterization and Raman Study of TiO₂ Nanowire Arrays Prepared by Anodic Oxidative Hydrolysis of TiCl₃. *Chemical Physics Letters* 2001, 338, 231-236.
- [300] Q. Lu, F. Gao, S. Komarneni & T. E. Mallouk. Ordered SBA-15 Nanorod Arrays Inside a Porous Alumina Membrane. *Journal of the American Chemical Society* 2004, 126, 8650-8651.
- [301] M. G. Hahm, A. Leela Mohana Reddy, D. P. Cole, M. Rivera, J. A. Vento, J. Nam, H. Y. Jung, Y. L. Kim, N. T. Narayanan, D. P. Hashim, C. Galande, Y. J. Jung, M. Bundy, S. Karna, P. M. Ajayan & R. Vajtai. Carbon Nanotube–Nanocup Hybrid Structures for High Power Supercapacitor Applications. *Nano Letters* 2012, 12, 5616–5621.
- [302] Y. Lei, K.-S. Yeong, J. T. L. Thong & W.-K. Chim. Large-Scale Ordered Carbon Nanotube Arrays Initiated from Highly Ordered Catalyst Arrays on Silicon Substrates. *Chemistry of Materials* 2004, 16, 2757-2761.

Bibliography

- [303] Y. B. Mao & S. S. Wong. General, Room-Temperature Method for the Synthesis of Isolated as well as Arrays of Single-Crystalline ABO₄-type Nanorods. *Journal of the American Chemical Society* 2004, 126, 15245-15252.
- [304] R. Artzi-Gerlitz, K. D. Benkstein, D. L. Lahr, J. L. Hertz, C. B. Montgomery, J. E. Bonevich, S. Semancik & M. J. Tarlov. Fabrication and Gas Sensing Performance of Parallel Assemblies of Metal Oxide Nanotubes Supported by Porous Aluminum Oxide Membranes. *Sensors and Actuators B: Chemical* 2009, 136, 257-264.
- [305] S. G. Ansari, Z. A. Ansari, R. Wahab, Y.-S. Kim, G. Khang & H.-S. Shin. Glucose Sensor Based on Nano-Baskets of Tin Oxide Templated in Porous Alumina by Plasma Enhanced CVD. *Biosensors and Bioelectronics* 2008, 23, 1838-1842.
- [306] S. Simovic, D. Losic & K. Vasilev. Controlled Drug Release from Porous Materials by Plasma Polymer Deposition. *Chemical Communications* 2010, 46, 1317-1319.
- [307] E. E. Leary Swan, K. C. Popat & T. A. Desai. Peptide-Immobilized Nanoporous Alumina Membranes for Enhanced osteoblast Adhesion. *Biomaterials* 2005, 26, 1969-1976.
- [308] J. Fu, P. Mao & J. Han. Artificial Molecular Sieves and Filters: A New Paradigm for Biomolecule Separation. *Trends in Biotechnology* 2008, 26, 311-320.
- [309] D. M. Dotzauer, J. Dai, L. Sun & M. L. Bruening. Catalytic Membranes Prepared Using Layer-by-Layer Adsorption of Polyelectrolyte/Metal Nanoparticle Films in Porous Supports. *Nano Letters* 2006, 6, 2268-2272.
- [310] Y. Lei, W. K. Chim, Z. P. Zhang, T. J. Zhou, L. D. Zhang, G. W. Meng & F. Phillipp. Ordered Nanoporous Nickel Films and Their Magnetic Properties. *Chemical Physics Letters* 2003, 380, 313-318.
- [311] X. D. Dang, W. Plieth, S. Richter, M. Plötner & W. J. Fischer. Aluminum Oxide Film as Gate Dielectric for Organic FETs: Anodization and Characterization. *physica status solidi (a)* 2008, 205, 626-632.
- [312] C. Liu, E. I. Gillette, X. Chen, A. J. Pearse, A. C. Kozen, M. A. Schroeder, K. E. Gregorczyk, S. B. Lee & G. W. Rubloff. An All-In-One Nanopore Battery Array. *Nature Nanotechnology* 2014, 9, 1031-1039.
- [313] W. Yong, W. Minghong, J. Zheng & L. Jim Yang. One-Dimensional SnO₂ Nanostructures: Facile Morphology Tuning and Lithium Storage Properties. *Nanotechnology* 2009, 20, 345704.
- [314] N. Kwon, K. Kim, J. Heo & I. Chung. Fabrication of Ordered Anodic Aluminum Oxide with Matrix Arrays of Pores Using Nanoimprint. *Journal of Vacuum Science & Technology A* 2009, 27, 803-807.
- [315] T. P. Hoar & J. Yahalom. The Initiation of Pores in Anodic Oxide Films Formed on Aluminum in Acid Solutions. *Journal of The Electrochemical Society* 1963, 110, 614-621.
- [316] K. R. Hebert, H. Wu, T. Gessmann & K. Lynn. Positron Annihilation Spectroscopy Study of Interfacial Defects Formed by Dissolution of Aluminum in Aqueous Sodium Hydroxide. *Journal of The Electrochemical Society* 2001, 148, B92-B100.
- [317] T. Martin & K. R. Hebert. Atomic Force Microscopy Study of Anodic Etching of Aluminum: Etching Morphology Development and Caustic Pretreatment *Journal of The Electrochemical Society* 2001, 148, B101-B109.
- [318] F. Li, L. Zhang & R. M. Metzger. On the Growth of Highly Ordered Pores in Anodized Aluminum Oxide. *Chemistry of Materials* 1998, 10, 2470-2480.
- [319] M. Paunovic & M. Schlesinger. Fundamentals of Electrochemical Deposition. *Wiley-Interscience*, 2006.

Bibliography

- [320] S. Nijjer, J. Thonstad & G. M. Haarberg. Oxidation of Manganese(II) and Reduction of Manganese Dioxide in Sulphuric Acid. *Electrochimica Acta* 2000, 46, 395-399.
- [321] M. Lu, F. Beguin & E. Frackowiak. Supercapacitors: Materials, Systems and Applications. *Wiley*, 2013.
- [322] T. A. Skotheim. Handbook of Conducting Polymers. *M. Dekker*, 1986.
- [323] R. Xiao. Controlled Electrochemical Synthesis of Conductive Polymer Nanostructures and Electrochromism Property Study *Ph.D Thesis*, University of Maryland, 2007.
- [324] J. Deng, X. Lv, J. Gao, A. Pu, M. Li, X. Sun & J. Zhong. Facile Synthesis of Carbon-Coated Hematite Nanostructures for Solar Water Splitting. *Energy & Environmental Science* 2013, 6, 1965-1970.
- [325] H. Li & H. Zhou. Enhancing the Performances of Li-Ion Batteries by Carbon-Coating: Present and Future. *Chemical Communications* 2012, 48, 1201-1217.
- [326] F. Cheng, J. Liang, Z. Tao & J. Chen. Functional Materials for Rechargeable Batteries. *Advanced Materials* 2011, 23, 1695-1715.
- [327] J. Wang & X. Sun. Understanding and Recent Development of Carbon Coating on LiFePO₄ Cathode Materials for Lithium-Ion Batteries. *Energy & Environmental Science* 2012, 5, 5163-5185.
- [328] A. Brandt & A. Balducci. Ferrocene as Precursor for Carbon-Coated α -Fe₂O₃ Nano-Particles for Rechargeable Lithium Batteries. *Journal of Power Sources* 2013, 230, 44-49.
- [329] A. Brandt & A. Balducci. A Study About the Use of Carbon Coated Iron Oxide-Based Electrodes in Lithium-Ion Capacitors. *Electrochimica Acta* 2013, 108, 219-225.
- [330] Y. Gogotsi. Nanostructured Films and Coatings. *Springer Netherlands*, 2000, Vol. 78, Ch. 3.
- [331] L.-R. Zhao, J. Wang, Y. Li, C.-W. Wang, F. Zhou & W.-M. Liu. Anodic Aluminum Oxide Films Formed in Mixed Electrolytes of Oxalic and Sulfuric Acid and Their Optical Constants. *Physica B: Condensed Matter* 2010, 405, 456-460.
- [332] G. E. J. Poinern, N. Ali & D. Fawcett. Progress in Nano-Engineered Anodic Aluminum Oxide Membrane Development. *Materials* 2011, 4, 487-526.
- [333] D. Gu, H. Bongard, Y. Meng, K. Miyasaka, O. Terasaki, F. Zhang, Y. Deng, Z. Wu, D. Feng, Y. Fang, B. Tu, F. Schüth & D. Zhao. Growth of Single-Crystal Mesoporous Carbons with Im $\bar{3}m$ Symmetry. *Chemistry of Materials* 2010, 22, 4828-4833.
- [334] T. E. Everhart & R. F. M. Thornley. Wide-Band Detector for Micro-Microampere Low-Energy Electron Currents. *Journal of Scientific Instruments* 1960, 37, 246.
- [335] J. Goldstein, D. E. Newbury, D. C. Joy, C. E. Lyman, P. Echlin, E. Lifshin, S. L. & M. J.R. Scanning Electron Microscopy and X-ray Microanalysis: Third Edition. *Springer*, 2007.
- [336] L. Reimer & H. Kohl. Transmission Electron Microscopy: Physics of Image Formation. *Springer*, 2008.
- [337] M. Himmerlich, S. Krischok, V. Lebedev, O. Ambacher & J. A. Schaefer. Morphology and Surface Electronic Structure of MBE Grown InN. *Journal of Crystal Growth* 2007, 306, 6-11.
- [338] S. Hüfner. Photoelectron Spectroscopy: Principles and Applications. *Springer*, 2003.
- [339] NT-MDT, NTEGRA Spectra - Instruction Manual, www.ntmdt.com, 06 Mai 2015.

Bibliography

- [340] R. L. McCreery. Raman Spectroscopy for Chemical Analysis. *Wiley*, 2005.
- [341] P. R. Griffiths & J. A. De Haseth. Fourier Transform Infrared Spectrometry. *Wiley*, 2007.
- [342] L. Spieß, G. Teichert, R. Schwarzer, H. Behnken & C. Genzel. Moderne Röntgenbeugung: Röntgendiffraktometrie für Materialwissenschaftler, Physiker und Chemiker. *Vieweg & Teubner*, 2012.
- [343] M. Schmuck, C. Stangl & C. Bayer, Primäre und wiederaufladbare Lithium-Batterien, ictm.tugraz.at/files/attachments/6848/122908_Script_Lithium_Batterien_2011.pdf, 06 Mai 2015.
- [344] P. L. Taberna, P. Simon & J. F. Fauvarque Electrochemical Characteristics and Impedance Spectroscopy Studies of Carbon-Carbon Supercapacitors. *Journal of The Electrochemical Society* 2003, 150, A292-A300.
- [345] Y.-J. Ma, F. Zhou, L. Lu & Z. Zhang. Low-Temperature Transport Properties of Individual SnO₂ Nanowires. *Solid State Communications* 2004, 130, 313-316.
- [346] M. S. Arnold, P. Avouris, Z. W. Pan & Z. L. Wang. Field-Effect Transistors Based on Single Semiconducting Oxide Nanobelts. *The Journal of Physical Chemistry B* 2002, 107, 659-663.
- [347] Y. Zhang, A. Kolmakov, Y. Lilach & M. Moskovits. Electronic Control of Chemistry and Catalysis at the Surface of an Individual Tin Oxide Nanowire. *The Journal of Physical Chemistry B* 2005, 109, 1923-1929.
- [348] I. Perez, E. Robertson, P. Banerjee, L. Henn-Lecordier, S. J. Son, S. B. Lee & G. W. Rubloff. TEM-Based Metrology for HfO₂ Layers and Nanotubes Formed in Anodic Aluminum Oxide Nanopore Structures. *Small* 2008, 4, 1223-1232.
- [349] J. M. Themlin, M. Chtaib, L. Henrard, P. Lambin, J. Darville & J. M. Gilles. Characterization of Tin Oxides by X-Ray Photoemission Spectroscopy. *Physical Review B* 1992, 46, 2460-2466.
- [350] H. W. Nesbitt & D. Banerjee. Interpretation of XPS Mn(2p) Spectra of Mn Oxyhydroxides and Constraints on the Mechanism of MnO₂ Precipitation. *American Mineralogist* 1998, 83, 305-315.
- [351] B. Y. Chang & S. M. Park. Electrochemical Impedance Spectroscopy. *Annual Review of Analytical Chemistry*, 2010, 3, 207-229.
- [352] X. Wen, D. Zhang, L. Shi, T. Yan, H. Wang & J. Zhang. Three-Dimensional Hierarchical Porous Carbon with a Bimodal Pore Arrangement for Capacitive Deionization. *Journal of Materials Chemistry* 2012, 22, 23835-23844.
- [353] C. Z. Yuan, B. Gao, L. F. Shen, S. D. Yang, L. Hao, X. J. Lu, F. Zhang, L. J. Zhang & X. G. Zhang. Hierarchically Structured Carbon-Based Composites: Design, Synthesis and Their Application in Electrochemical Capacitors. *Nanoscale* 2011, 3, 529-545.
- [354] D. P. Dubal, D. S. Dhawale, R. R. Salunkhe & C. D. Lokhande. Conversion of Interlocked Cube-Like Mn₃O₄ into Nanoflakes of Layered Birnessite MnO₂ during Supercapacitive Studies. *Journal of Alloys and Compounds* 2010, 496, 370-375.
- [355] A. L. M. Reddy, M. M. Shaijumon, S. R. Gowda & P. M. Ajayan. Multisegmented Au-MnO₂/Carbon Nanotube Hybrid Coaxial Arrays for High-Power Supercapacitor Applications. *The Journal of Physical Chemistry C* 2010, 114, 658-663.
- [356] D. P. Dubal, D. S. Dhawale, R. R. Salunkhe & C. D. Lokhande. Conversion of Chemically Prepared Interlocked Cubelike Mn₃O₄ to Birnessite MnO₂ Using Electrochemical Cycling. *Journal of The Electrochemical Society* 2010, 157, A812-A817.

Bibliography

- [357] Z. Song, W. Liu, M. Zhao, Y. Zhang, G. Liu, C. Yu & J. Qiu. A Facile Template-Free Synthesis of α -MnO₂ Nanorods for Supercapacitor. *Journal of Alloys and Compounds* 2013, 560, 151-155.
- [358] L. Basiricò & G. Lanzara. Moving Towards High-Power, High-Frequency and Low-Resistance CNT Supercapacitors by Tuning the CNT Length, Axial Deformation and Contact Resistance. *Nanotechnology* 2012, 23, 305401.
- [359] D. Pech, M. Brunet, H. Durou, P. Huang, V. Mochalin, Y. Gogotsi, P.-L. Taberna & P. Simon. Ultrahigh-Power Micrometre-Sized Supercapacitors Based on Onion-Like Carbon. *Nature Nanotechnology* 2010, 5, 651-654.
- [360] F. Scholz. *Electroanalytical Methods: Guide to Experiments and Applications*. Springer, 2009.
- [361] M. A. Chougule, S. G. Pawar, P. R. Godse, R. N. Mulik, Shashwati Sen & V. B. Patil. Synthesis and Characterization of Polypyrrole (PPy) Thin Films. *Soft Nanoscience Letters* 2011, 1, 6-10.
- [362] H. S. Kim, D. H. Park, Y. B. Lee, D.-C. Kim, H.-J. Kim, J. Kim & J. Joo. Doped and De-Doped Polypyrrole Nanowires by Using a BMIMPF₆ Ionic Liquid. *Synthetic Metals* 2007, 157, 910-913.
- [363] P. C. Mindroiu M., Popescu S., Demetrescu I. Polypyrrole as Conducting Polymer Coating on Ti₆Al₇Nb Alloy. *Materiale Plastic* 2009, 4, 394-398.
- [364] M. Li, Z. Wei & L. Jiang. Polypyrrole Nanofiber Arrays Synthesized by a Biphasic Electrochemical Strategy. *Journal of Materials Chemistry* 2008, 18, 2276-2280.
- [365] Y.-C. Liu, B.-J. Hwang, W.-J. Jian & R. Santhanam. In Situ Cyclic Voltammetry-Surface-Enhanced Raman Spectroscopy: Studies on the Doping–Undoping of Polypyrrole Film. *Thin Solid Films* 2000, 374, 85-91.
- [366] Y. C. Liu & B. J. Hwang. Identification of Oxidized Polypyrrole on Raman Spectrum. *Synthetic Metals* 2000, 113, 203-207.
- [367] Hibben J. H. The Raman Spectra of Oxalic Acid. *Journal of Chemical Physics* 1935, 3, 675-679.
- [368] J. Yan, A. Sumboja, X. Wang, C. Fu, V. Kumar & P. S. Lee. Insights on the Fundamental Capacitive Behavior: A Case Study of MnO₂. *Small* 2014, 10, 3568-3578.
- [369] C. Meng, C. Liu, L. Chen, C. Hu & S. Fan. Highly Flexible and All-Solid-State Paperlike Polymer Supercapacitors. *Nano Letters* 2010, 10, 4025-4031.
- [370] M. F. El-Kady, V. Strong, S. Dubin & R. B. Kaner. Laser Scribing of High-Performance and Flexible Graphene-Based Electrochemical Capacitors. *Science* 2012, 335, 1326-1330.
- [371] K. Letchford & H. Burt. A Review of the Formation and Classification of Amphiphilic Block Copolymer Nanoparticulate Structures: Micelles, Nanospheres, Nanocapsules and Polymersomes. *European Journal of Pharmaceutics and Biopharmaceutics* 2007, 65, 259-269.
- [372] S. Gao, Y. Sun, F. Lei, L. Liang, J. Liu, W. Bi, B. Pan & Y. Xie. Ultrahigh Energy Density Realized by a Single-Layer Beta-Co(OH)₂ All-Solid-State Asymmetric Supercapacitor. *Angewandte Chemie International Edition* 2014, 53, 12789-12793.
- [373] H. B. Li, M. H. Yu, F. X. Wang, P. Liu, Y. Liang, J. Xiao, C. X. Wang, Y. X. Tong & G. W. Yang. Amorphous Nickel Hydroxide Nanospheres with Ultrahigh Capacitance and Energy Density as Electrochemical Pseudocapacitor Materials. *Nature Communications* 2013, 4, 1894.

Bibliography

- [374] H. B. Wu, H. Pang & X. W. Lou. Facile Synthesis of Mesoporous $\text{Ni}_{0.3}\text{Co}_{2.7}\text{O}_4$ Hierarchical Structures for High Performance Supercapacitors. *Energy & Environmental Science* 2013, 6, 3619-3626.
- [375] C. Yuan, J. Li, L. Hou, X. Zhang, L. Shen & X. W. Lou. Ultrathin Mesoporous NiCo_2O_4 Nanosheets Supported on Ni Foam as Advanced Electrodes for Supercapacitors. *Advanced Functional Materials* 2012, 22, 4592-4597.
- [376] J. Duay, S. A. Sherrill, Z. Gui, E. Gillette & S. B. Lee. Self-Limiting Electrodeposition of Hierarchical MnO_2 and $\text{M}(\text{OH})_2/\text{MnO}_2$ Nanofibril/Nanowires: Mechanism and Supercapacitor Properties. *ACS Nano* 2013, 7, 1200-1214.
- [377] Y. Lei, B. Daffos, P. L. Taberna, P. Simon & F. Favier. MnO_2 -Coated Ni Nanorods: Enhanced High Rate Behavior in Pseudo-Capacitive Supercapacitor. *Electrochimica Acta* 2010, 55, 7454-7459.
- [378] R. Liu & S. B. Lee. MnO_2 /Poly(3,4-ethylenedioxythiophene) Coaxial Nanowires by One-Step Coelectrodeposition for Electrochemical Energy Storage. *Journal of the American Chemical Society* 2008, 130, 2942-2943.
- [379] Z. Fan, J. Yan, T. Wei, L. Zhi, G. Ning, T. Li & F. Wei. Asymmetric Supercapacitors Based on Graphene/ MnO_2 and Activated Carbon Nanofiber Electrodes with High Power and Energy Density. *Advanced Functional Materials* 2011, 21, 2366-2375.
- [380] C. Zhou, Y. Zhang, Y. Li & J. Liu. Construction of High-Capacitance 3D $\text{CoO}@\text{Polypyrrole}$ Nanowire Array Electrode for Aqueous Asymmetric Supercapacitor. *Nano Letters* 2013, 13, 2078-2085.
- [381] Web of Science, apps.webofknowledge.com, 06 Mai 2015.

8 Appendix

Table A1 | Literature survey of reported MnO₂ based core/shell and bare MnO₂ supercapacitor materials. The reported specific capacitance refers to a three-electrode measurement in an aqueous electrolyte.

Electrode material	Specific capacitance at low and high power	Cycle retention	Mass loading	Synthesis method	Binder	Electrolyte	Control of structural parameters
MnO ₂ /aMEGO ^(a) [124]	850 F g ⁻¹ (0.25 A g ⁻¹) 187 F g ⁻¹ (20 A g ⁻¹)	87.7 % after 1000 cycles	0.7 to 1.4 mg	self-controlled redox process	yes	1 M H ₂ SO ₄	no structural control
MnO ₂ /Mn/MnO ₂ NT ^(a) [117]	955 F g ⁻¹ (1.5 A g ⁻¹) 660 F g ⁻¹ (24 A g ⁻¹)	97.5 % after 3000 cycles	0.32 mg cm ⁻²	template assisted electrodeposition	no	1 M Na ₂ SO ₄	some structural control
MnO ₂ on tin oxide NW ^(a) [120]	800 F g ⁻¹ (1 A g ⁻¹) 255 F g ⁻¹ (50 A g ⁻¹)	98.8 % after 2000 cycles	0.08 mg	solution based method	no	1 M Na ₂ SO ₄	no structural control shown
Zn ₂ SnO ₄ /MnO ₂ Nanocable ^(a) [121]	642 F g ⁻¹ (1 A g ⁻¹)	98.8 % after 1000 cycles	not reported	solution based method	no	1 M Na ₂ SO ₄	no structural control shown
MnO ₂ /TiN NT ^(a) [119]	681 F g ⁻¹ (2 A g ⁻¹) 390 F g ⁻¹ (400 A g ⁻¹)	97 % after 1000 cycles	0.015 mg 0.06 mg cm ⁻²	ALD, electrodeposition	no	1 M Na ₂ SO ₄	some structural control
MnO ₂ /Au/Ni foam ^(a) [122]	390 F g ⁻¹ (5 A g ⁻¹) 331 F g ⁻¹ (15 A g ⁻¹)	97 % after 2000 cycles	0.4 mg cm ⁻²	electrodeposition	no	1 M Na ₂ SO ₄	no structural control
MnO ₂ /Ni foam ^(a) [123]	241 F g ⁻¹ (1 A g ⁻¹) 331 F g ⁻¹ (15 A g ⁻¹)	90 % after 1000 cycles	1.03 mg cm ⁻²	hydrothermal	no	1 M Na ₂ SO ₄	no structural control
hollow-sphere like MnO ₂ ^[105]	167 F g ⁻¹ (2.5 mA) 124 F g ⁻¹ (10 mA)	89 % after 350 cycles	~10 mg	hydrothermal	yes	0.1 M Na ₂ SO ₄	some structural control
MnO ₂ NT array ^(a) [115]	349 F g ⁻¹ (1 A g ⁻¹) 245 F g ⁻¹ (10 A g ⁻¹)	81 % after 2000 cycles	not reported	template assisted electrodeposition	no	1 M Na ₂ SO ₄	selection of NT or NW array

Appendix

Electrode material	Specific capacitance at low and high power	Cycle retention	Mass loading	Synthesis method	Binder	Electrolyte	Control of structural parameters
MnO ₂ NW network ^(a) [24]	279 F g ⁻¹ (1 A g ⁻¹) 152 F g ⁻¹ (20 A g ⁻¹)	98.3 % after 1000 cycles	not reported	hydrothermal	yes	1 M Na ₂ SO ₄	no structural control
MnO ₂ NW on CNT paper ^(b) [110]	167.5 F g ⁻¹ (0.077 A g ⁻¹) 107.9 F g ⁻¹ (0.77 A g ⁻¹)	88 % after 3000 cycles	not reported	electrodeposition	no	0.1 M Na ₂ SO ₄	no structural control
flower like MnO ₂ ^(a) [104]	168 F g ⁻¹ (0.2 A g ⁻¹) 107.9 F g ⁻¹ (0.77 A g ⁻¹)	not investigated	not reported	hydrothermal	no	1 M Na ₂ SO ₄	some structural control
clew-like MnO ₂ ^(a) [106]	120 F g ⁻¹ (5 mV s ⁻¹)	not investigated	0.2 mg cm ⁻²	hydrothermal	yes	1 M Na ₂ SO ₄	urchin-like to clew-like morphology
MnO ₂ nanobelt ^(a) [108]	268 F g ⁻¹ (0.2 A g ⁻¹)	100 % after 1000 cycles	not reported	hydrothermal	yes	1 M Na ₂ SO ₄	Some structural control
needle-like MnO ₂ ^(a) [109]	209.8 F g ⁻¹ (2 mA cm ⁻²)	not investigated	7.6 mg cm ⁻²	precipitation	yes	1 M Na ₂ SO ₄	needle-like to spindle-like morphology
MnO ₂ NW array on Ti/Si substrate ^(a) [111]	254 F g ⁻¹ (10 mV s ⁻¹)	not investigated	not reported	template assisted electrodeposition	No	0.5 M Na ₂ SO ₄	NW length
Graphene/MnO ₂ composite ^(a) [125]	327.5 F g ⁻¹ (10 mV s ⁻¹)	88 % after 1000 cycles	2.7–3.2 mg	chemical reduction	yes	1 M Na ₂ SO ₄	no structural control
MnO ₂ /TiN NT array ^(a) [118]	834 F g ⁻¹ (9 A g ⁻¹) 662 F g ⁻¹ (45 A g ⁻¹)	72 % after 350 cycles	0.01 to 0.04 mg	ALD, electrodeposition	no	1 M LiClO ₄	NT wall thickness
M(OH) ₂ /MnO ₂ NW ^(a) [376]	298 F g ⁻¹ (50 mV s ⁻¹) 174 F g ⁻¹ (250 mV s ⁻¹)	82.5 % after 1000 cycles	not reported	template assisted electrodeposition	no	1 M LiClO ₄	NW length
CNT/MnO ₂ ^(b) [128]	365 F g ⁻¹ (0.385 A g ⁻¹) 295 F g ⁻¹ (15 A g ⁻¹)	89 % after 500 cycles	0.13 mg cm ⁻¹	PECVD grown CNT electrodeposition	no	0.1 M Na ₂ SO ₄	CNT length

Appendix

Electrode material	Specific capacitance at low and high power	Cycle retention	Mass loading	Synthesis method	Binder	Electrolyte	Control of structural parameters
MnO ₂ nanorod ^(a) [357]	366 F g ⁻¹ (0.2 A g ⁻¹) 137 F g ⁻¹ (5 A g ⁻¹)	73.9 % after 1000 cycles	10 mg	chemical	yes	1 M KOH	no structural control
Coral-like MnO ₂ ^(a) [127]	221 F g ⁻¹ (0.5 A g ⁻¹)	86 % after 3000 cycles	not reported	ZnO template assisted growth	no	1 M Na ₂ SO ₄	no structural control
CNT/MnO ₂ ^(a) [126]	463 F g ⁻¹ (5 A g ⁻¹) 423 F g ⁻¹ (20 A g ⁻¹)	91 % after 100 cycles	0.1 mg	CNT of PT/Si waver electrodeposition	no	1 M KCl	no structural control
Co ₃ O ₄ @Pt@MnO ₂ ^(a) [181]	539 F g ⁻¹ (1 A g ⁻¹)	89.8 % after 5000 cycles	0.1 to 0.3 mg	hydrothermal	no	1 M Na ₂ SO ₄	no structural control
MnO ₂ /Graphene nanosheet ^(a) [176]	267 F g ⁻¹ (0.2 A g ⁻¹) 208 F g ⁻¹ (10 A g ⁻¹)	92 % after 7000 cycles	not reported	hydrothermal	no	PVA/H ₃ PO ₄ gel	ultra-thin nanosheets
Ni/MnO ₂ ^(a) [377]	190 F g ⁻¹	80 % after 500 cycles	0.0177-0.250 mg	electrodeposition	no	0.5 M K ₂ SO ₄	NW length and shell thickness
MnO ₂ /PEDOT ^(a) [378]	210 F g ⁻¹ (5 mA cm ⁻²) 185 F g ⁻¹ (25 mA cm ⁻²)	not investigated	approx. 0.1 mg	electrochemical co-deposition	no	1 M Na ₂ SO ₄	NW length
AuPd/MnO ₂ nanopillar ^(a) [129]	603 F g ⁻¹ (10 A g ⁻¹) 293 F g ⁻¹ (100 A g ⁻¹)	93 % after 5000 cycles	<0.02 mg cm ⁻²	nano-imprint lithography, electrodeposition	no	1 M Na ₂ SO ₄	ordered nanopillar array
Carbon/MnO ₂ ^(a) [144]	793 F g ⁻¹ (1.5 A g ⁻¹) 520 F g ⁻¹ (20 A g ⁻¹)	97 % after 9000 cycles	0.22 mg cm ⁻²	ZnO template assisted growth	no	1 M Na ₂ SO ₄	no structural control
MnO ₂ /Ni ^(a) [131]	570 F g ⁻¹ (2 A g ⁻¹) 271 F g ⁻¹ (100 A g ⁻¹)	83 % after 3000 cycles	0.08-0.40 mg cm ⁻²	Ni template, electrodeposition	no	1 M Na ₂ SO ₄	very high structural controllability
a) performance based on MnO ₂ mass							
b) performance based on entire electrode mass							

Appendix

Table A2 | Literature survey of aqueous symmetric and asymmetric supercapacitors measured in a two-cell configuration. Specific energy values at high and low specific power are listed if reported.

Electrode materials (negative//positive)	Type	Specific energy [Wh kg ⁻¹] ^(a)	Specific power [kW kg ⁻¹] ^(b)	Electrolyte	Binder	Potential window	Mass loading	Features and controllability
Graphene/MoO ₃ // Graphene/MnO ₂ ^[196]	asym.	42.6 ~9	0.276 ~1.8	1 M Na ₂ SO ₄	yes	2 V	not reported	none
PEDOT//MnO ₂ /PEDOT [203]	asym.	12.6 1.3	0.21 8.5	gel electrolyte, 1 M LiClO ₄ /Acetonitrile:propylene carbonate solvent /PMMA	no	1.7 V	8.29 mg	flexible, some structural control
Graphene//MnO ₂ NW/Graphene ^[213]	asym.	30.4 7.0	0.1 5.0	1 M Na ₂ SO ₄	yes	2.0 V	not reported	none
ACN//Graphene/MnO ₂ [379]	asym.	51.1 8.2	0.102 16.5	1 M Na ₂ SO ₄	yes	1.8 V	not reported	none
AC//CoO@PPy NW ^[380]	asym.	43.5 11.8	0.0875 5.5	3 M NaOH	yes//no	1.8 V	1.98 mg	none
Fe ₃ O ₄ //MnO ₂ ^[190]	asym.	8.1	0.405	0.1 M K ₂ SO ₄	yes	1.8 V	not reported	none
Carbon//MnO ₂ ^[190]	asym.	17.3	0.605	0.1 M K ₂ SO ₄	yes	2.2 V	not reported	none
Fe ₃ O ₄ //MnO ₂ ^[193]	asym.	7	0.82	0.1 M K ₂ SO ₄	yes	1.8 V	not reported	none

Appendix

Electrode materials (negative//positive)	Type	Specific energy [Wh kg ⁻¹] ^(a)	Specific power [kW kg ⁻¹] ^(b)	Electrolyte	Binder	Potential window	Mass loading	Features and controllability
AC//MnO ₂ ^[188]	asym.	19 10	0.2 3.6	0.65 K ₂ SO ₄	yes	2.2 V	not reported	none
AC//MnO ₂ ^[207]	asym.	10	16 ^(c)	0.1 M K ₂ SO ₄	yes	2.0 V	not reported	Stability measurements of 195000 cycles
AC//K _{0.27} MnO ₂ ^[32]	asym.	25.3 17.6	0.14 2	0.5 M K ₂ SO ₄	yes	1.8 V	not reported	none
LiMn ₂ O ₄ //MnO ₂ ^[208]	asym.	24	0.18	1 M Li ₂ SO ₄	yes	2 V	23.5 mg	none
AC//MnO ₂ ^[189]	asym.	28.8 20.8	0.5 8	1 M KCl	yes	2 V	not reported	none
GHCS//GHCS/MnO ₂ [210]	asym.	22.1 4.1	0.1 5.5	1 M Na ₂ SO ₄	yes	2 V	not reported	none
AC//λ-MnO ₂ ^[209]	asym.	36	0.314	1 M Li ₂ SO ₄	yes	2.2 V	25 mg	none
Graphene//Graphene/Mn O ₂ NW ^[213]	asym.	30.4 7	0.1 4	1 M Na ₂ SO ₄	yes	2.0 V	not reported	79 % after 1000 cycles
Graphene//Graphene/γ- MnO ₂ ^[214]	asym.	11.4	25.8 ^(c)	1 M KCl	no	0.9 V	0.2 to 0.5 mg cm ⁻²	none
Graphene Hydrogel//MnO ₂ ^[33]	asym.	23.2 14.9	1 10	0.5 M Na ₂ SO ₄	no	2 V	2 mg	83 % after 5000 cycles

Appendix

Electrode materials (negative//positive)	Type	Specific energy [Wh kg ⁻¹] ^(a)	Specific power [kW kg ⁻¹] ^(b)	Electrolyte	Binder	Potential window	Mass loading	Features and controllability
AC/fFWNT//RGO/MnO ₂ /f FWNT ^[211]	asym.	27 24	0.13 7.8	1 M Na ₂ SO ₄	no	2 V	not reported	flexible
ACNF//CNF/MnO ₂ ^[212]	asym.	30.6 8.7	0.2 20.8	0.5 M H ₂ SO ₄	no	2 V	not reported	none
MnO ₂ //MnO ₂ ^[190]	sym.	3.3	0.265	0.1 M K ₂ SO ₄	yes	1.0 V	not reported	none
Au/CNT/MnO ₂ //Au/CNT/ MnO ₂ ^[355]	sym.	4.5	33 ^(c)	0.1 M Na ₂ SO ₄	no	0.7 V	not reported	Some structural control inherited from AAO template
OMC//OMC ^[204]	sym.	4 6	0.8 1.05	30 wt. % KOH	yes	0.9 V	10 mg	none
HPGC//HPGC ^[205]	sym.	9 5.3	0.01 25	6 M KOH	yes	1 V	5 mg cm ⁻²	none
ALG-C//ALG-C ^[206]	sym.	7.4 3.5	3 11	1 M H ₂ SO ₄	yes	1 V	not reported	none
MnO ₂ /PEDOT// MnO ₂ /PEDOT ^[203]	sym.	7.7 0.2	0.213 4.0	gel electrolyte, 1 M LiClO ₄ /Acetonitrile:propylene carbonate solvent /PMMA	no	1.0 V	5.86 mg	flexible, some structural control
a) highest and lowest reported values b) highest and lowest reported values; power densities calculated from $P_{\text{real}} = E/t_{\text{discharge}}$ unless otherwise indicated c) power density at matched impedance								

Appendix

Table A3 | Specific capacitance values of the o-SnO₂/MnO₂ and c-SnO₂/MnO₂ nanotube array. The data is plotted in Figure 5-13a.

current density [A g ⁻¹]	o-SnO ₂ /MnO ₂		c-SnO ₂ /MnO ₂	
	Specific capacitance [F g ⁻¹]	C _{Er,MnO₂} [F g ⁻¹]	Specific capacitance [F g ⁻¹]	C _{Er,MnO₂} [F g ⁻¹]
1	910	173	534	173
2	653	79	413	79
5	505	58	302	58
10	408	33	219	33
20	316	17	162	17
30	268	16	144	16
40	239	13	135	13
50	217	13	129	13

Table A4 | Specific capacitance values of the SnO₂/PPy nanotube array. The data is plotted in Figure 5-19a.

current density [A g ⁻¹]	SnO ₂ /PPy	
	Specific capacitance [F g ⁻¹]	C _{Er,PPy} [F g ⁻¹]
1	260	32
2	256	27
5	250	21
10	241	17
20	226	13
30	213	10
40	201	8
50	189	7

Table A5 | Device performance of the PPy//MnO₂ asymmetric device. The data is plotted in Figure 5-24b.

current density [A g ⁻¹]	specific energy [Wh kg ⁻¹]	specific power [kW kg ⁻¹]	E _{Er,asy} [Wh kg ⁻¹]	P _{Er,asy} [kW kg ⁻¹]
1	27.2	0.85	3.5	0.03
2	23.4	1.57	1.9	0.04
5	19.2	3.71	1.4	0.07
10	16.1	6.93	0.8	0.10
20	13.3	13.06	0.5	0.14
30	10.7	17.35	0.4	0.19
40	9.0	20.90	0.3	0.21
50	7.8	24.85	0.3	0.27

Appendix

Table A6 | Device performance of the MnO₂//MnO₂ symmetric device. The data is plotted in Figure 5-24b.

current density [A g ⁻¹]	specific energy [Wh kg ⁻¹]	specific power [kW kg ⁻¹]	E _{Er,sym} [Wh kg ⁻¹]	P _{Er,sym} [kW kg ⁻¹]
1	16.8	0.21	3.2	0.01
2	12.1	0.41	1.5	0.02
5	8.1	0.95	0.9	0.03
10	5.5	1.74	0.4	0.04
20	3.6	3.24	0.2	0.05
30	2.6	4.35	0.2	0.07
40	1.9	5.17	0.1	0.08
50	1.5	6.00	0.1	0.10

Table A7 | Specific capacitance values of the C-TiN and TiN nanotube array. The data is plotted in Figure 5-32c.

current density [A g ⁻¹]	C-TiN Specific capacitance [F g ⁻¹]	TiN Specific capacitance [F g ⁻¹]	C-TiN (1 M Na ₂ SO ₄) Specific capacitance [F g ⁻¹]
1	167	139	49
2	156	114	41
5	146	93	32
10	135	77	25
25	114	56	19 (20 A g ⁻¹)
50	95	40	14 (30 A g ⁻¹)

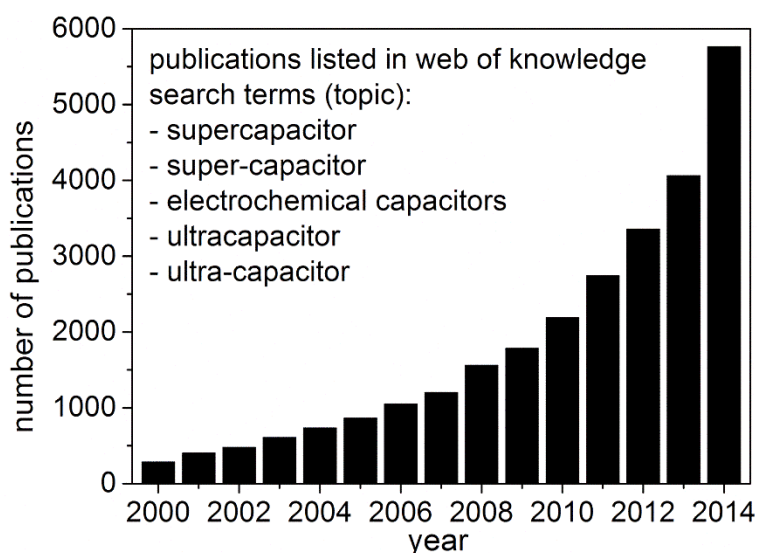


Figure A1 | Number of publications per year listed in *Web of Knowledge*^[381] related to supercapacitors with search terms: supercapacitor, super-capacitor, electrochemical capacitor, ultracapacitor and ultra-capacitor.

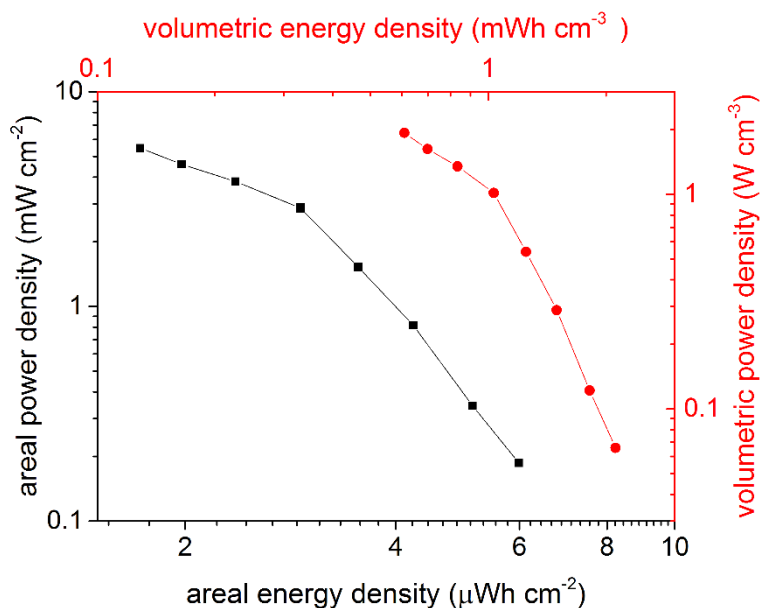


Figure A3 | Areal and volumetric energy and power density of the asymmetric PPy//MnO₂ supercapacitor. The device exhibits a maximum areal energy density of 5.99 $\mu\text{Wh cm}^{-2}$ at an areal power density of 0.19 mW cm^{-2} and shows a maximum volumetric energy density of 2.12 mWh cm^{-3} at 0.07 W cm^{-3} . A literature comparison to the reported devices in Figure 5-24b cannot be given because areal and volumetric performance values are not reported.

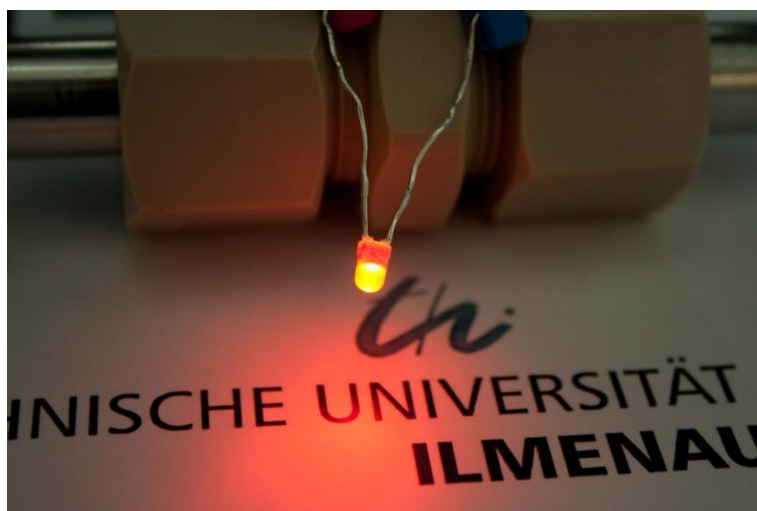


Figure A4 | The asymmetric PPy//MnO₂ supercapacitor can light up a red LED.

Appendix

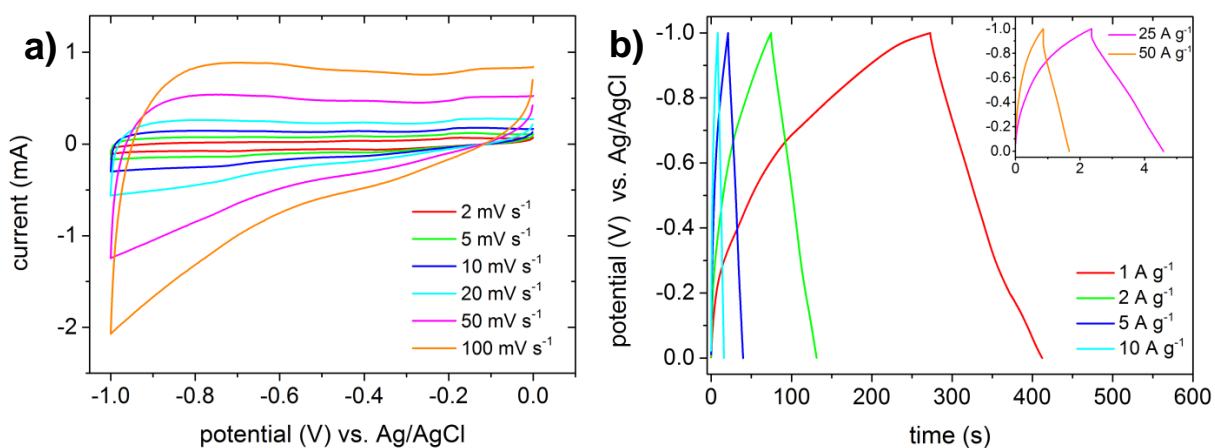


Figure A5 | Electrochemical performance of the bare TiN nanotube array. (a) CV and (b) charge/discharge performance of the bare TiN nanotube array.^[17]

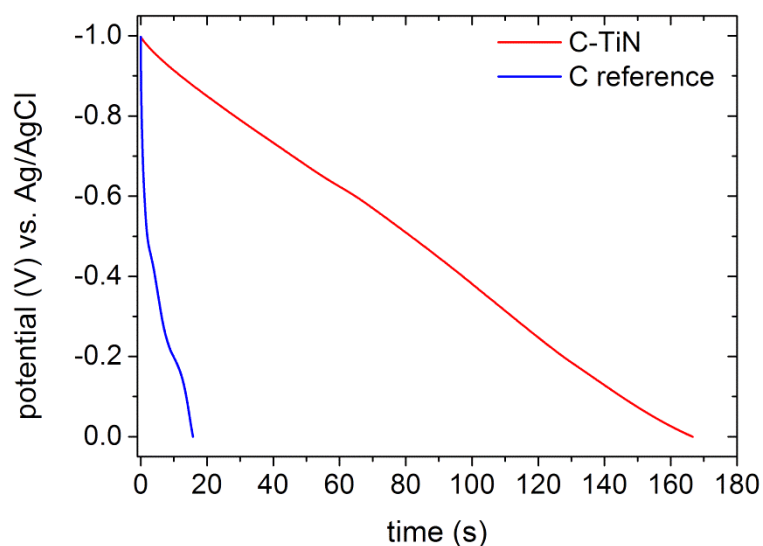


Figure A6 | Charge/discharge performance of the C-TiN nanotube array at 1 A g⁻¹ in comparison to a bare C nanotube array without TiN deposition. This comparison shows that the bare nanotube array contributes about 9.5 % to the C-TiN performance.^[17]

Acknowledgment

Foremost, I would like to thank Prof. Yong Lei for providing me with the opportunity to complete my Ph.D. thesis in his research group at the TU Ilmenau. I especially want to thank him for his support and guidance throughout the entire project. He has been actively interested in this work and has always been available for discussions and fruitful advice. He has not only been a scientific adviser to me during my Ph.D., moreover, he has introduced the Chinese culture to me and gave me the opportunity to visit China on several occasions and work in excellent Chinese universities. I am truly thankful for the unforgettable experience and memories that I could gain during this time.

I also want to thank Prof. Dr. Yi Xie from the University of Science and Technology of China for giving me the opportunity to work in her group for four months. I am pleased that the fruitful exchange has led to two co-authored papers. The stay has generated many good and long lasting memories, both from a scientific and non-scientific point of view.

Moreover, I need to thank Prof. Dr. Shu-Hong Yu from the University of Science and Technology of China for inviting me into his research group. The welcoming atmosphere has inspired me and the collaborating work has resulted in excellent scientific results. Many evenings at small barbeque places with his students have made the stay an unforgettable experience.

Further, I would like to thank my group members for a pleasant and inspiring working environment. It was a great pleasure to work in such an international and diverse scientific group. My special thanks go to Huaping Zhao and Liaoyong Wen for fruitful discussions, exchange of ideas and supplying chemical knowledge whenever needed.

In regard to TEM measurements, I thank Nina Winkler and Martin Peterlechner from the University of Münster for their effort and time. For XPS measurements, I thank Marcel Himmerlich for supplying help and knowledge.

I also acknowledge the “Bundesministerium für Bildung und Forschung” (ZIK-3DNanoDevice: 03Z1MN11) and the “European Research Council” (ThreeDsurface: 240144) for the financial support of this work.

For the non-scientific part, I thank Soizic and my parents for supporting me during the entire process of my Ph.D.

Scientific contributions

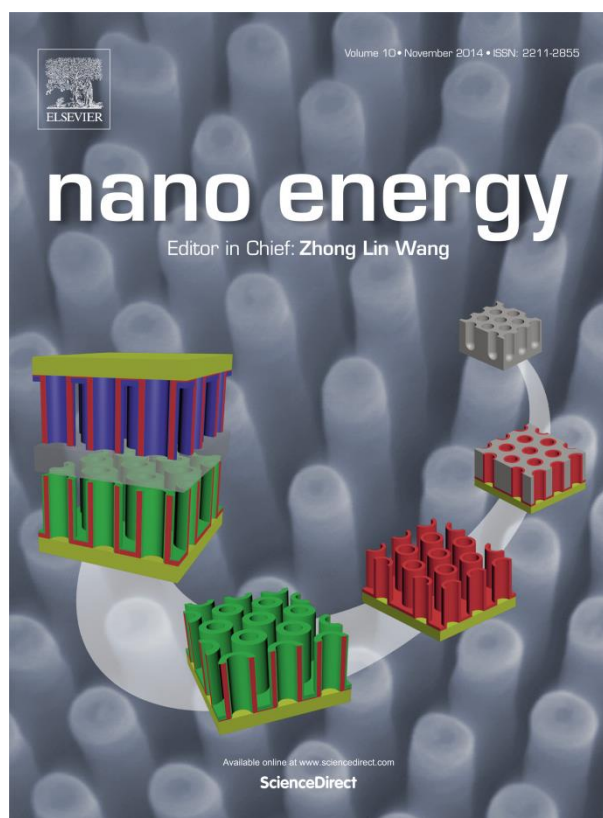
In total I have published 12 papers in SCI-indexed international scientific journals during the period of my Ph.D., including 6 papers with impact factor higher than 10 (*Nano Energy*, *Advanced Materials*, *Advanced Energy Materials*, *Nature Communication*, *Journal of the American Chemical Society*, *Angewandte Chemie International Edition*) and 6 papers with impact factor between 3 and 8 (*Small*, *Applied Physics Letters*, *Journal of Power Sources*, *Journal of Materials Chemistry A*, *Catalyst Today*). The published papers were cited for more than 250 times during 2014 and 2015 (Source: google scholar database).

I also gave 17 contributions at conferences and meetings, including 2 conference proceedings, 12 talks and 3 posters.

The excellent results based on the asymmetric PPy//MnO₂ supercapacitor have provoked the prestigious journal *Nano Energy* (IF 10.211) to highlight the publication on the cover page of the journal.

Cover

The paper “A Complete Three-Dimensionally Nanostructured Asymmetric Supercapacitor with High Operating Voltage Window based on PPy and MnO₂” by **Grote F.** and Lei Y. was selected as the cover page of *Nano Energy* in Volume 10, 2014.



Peer-reviewed Publications in SCI-indexed Scientific Journals

1. Xu Y., Zhou M., Wang X., Wang C.L., Liang L.Y., **Grote F.**, Wu M.H., Mi Y., Lei Y., Enhancement of Sodium Ion Battery Performance Enabled by Oxygen Vacancies. *Angewandte Chemie International Edition* 2015, DOI: 10.1002/anie.201503477 (IF 11.261).
2. **Grote F.**, Yu Z. Y., Wang J. L., Yu S. H., Lei Y., Self-Stacked Reduced Graphene Oxide Nanosheets Coated with Cobalt-Nickel Hydroxide by One-Step Electrochemical Deposition Towards Flexible Electrochromic Supercapacitor. *Small* 2015, DOI:10.1002/smll.201501037 (IF 8.368; Small hot article Top 10 - 07/2015).
3. Zhan Z., **Grote F.**, Wang Z., Xu R. and Lei Y., New Approach to Enhance the Performance of Localized Surface Plasmon Resonance: Degenerating Quadrupole and Dipole Modes. *Advanced Energy Materials*, DOI: 10.1002/aenm.201501654 (IF 16.146).
4. **Grote F.**, Zhao H., Lei Y, Self-Supported Carbon Coated TiN Nanotube Arrays: Innovative Carbon Coating Leads to an Improved Cycling Ability for Supercapacitor Applications. *Journal of Materials Chemistry A* 2015, 3, 3465-3470 (IF 7.443).
5. Mi Y., Wen L., Wang Z., Zhao H., Zhou Y., **Grote F.** and Lei Y., Ultra-Low Mass Loading of Platinum Nanoparticles on Bacterial Cellulose Derived Carbon Nanofibers for Efficient Hydrogen Evolution. *Catalyst Today*, DOI:10.1016/j.cattod.2015.08.019 (IF 3.893)
6. **Grote F.**, Lei Y., A Complete Three-Dimensionally Nanostructured Asymmetric Supercapacitor with High Operating Voltage Window based on PPy and MnO₂. *Nano Energy* 2014, 10, 63-70 (IF 10.325).
7. Zhao H., Wang C.L., Vellacheri R., Zhou M., Xu Y., Fu Q., Wu M.H., **Grote F.**, Lei Y., Self-Supported Metallic Nanopore Arrays with Highly-Oriented Nanoporous Structure as Ideally Nanostructured Electrode for Supercapacitor Application. *Advanced Materials* 2014, 26, 7654-7659 (IF 17.493).
8. Zhu H., Xiao C., Cheng H., **Grote F.**, Zhang X., Yao T., Wang C., Wei S., Lei Y., and Xie Y., Magnetocaloric Effects in a Freestanding and Flexible Graphene-Based Superlattice Synthesized with a Spatially Confined Reaction. *Nature Communications* 2014, 5, 3960 (IF 11.47).

Scientific contributions

9. **Grote F.**, Liaoyong Wen, Lei Y., Nano-Engineering of Three-Dimensional Core/Shell Nanotube Arrays for High Performance Supercapacitors. *Journal of Power Sources* 2014, 256, 37-42 (IF 6.217).
10. **Grote F.**, Kühnel R.-S. Balducci A., Lei Y., Template Assisted Fabrication of Free-Standing MnO₂ Nanotube and Nanowire Arrays and Their Application in Supercapacitors. *Applied Physics Letters* 2014, 104 (IF 3.302).
11. Wen L., Mi Y., Wang C., Fang Y., **Grote F.**, Zhao H., Zhou M., Lei Y., Cost-Effective Atomic Layer Deposition Synthesis of Pt Nanotube Arrays: Application for High Performance Supercapacitor. *Small* 2014, 10, 3162-3168 (IF 8.368).
12. Xie J., Zhang J., Li S., **Grote F.**, Zhang X., Zhang H., Wang R., Lei Y., Pan B., Xie Y., Controllable Disorder Engineering in Oxygen-incorporated MoS₂ Ultrathin Nanosheets for Efficient Hydrogen Evolution. *Journal of the American Chemical Society* 2013, 135, 17881-17888 (IF 12.113).

Publications in Conference Proceedings

1. **Grote F.**, Lei Y.*, Template-Assisted Fabrication of Self-Supported 3D Functional Nanostructure Arrays Towards High Performance Devices. *VDE VERLAG GmbH GMM-Fachbericht-Mikro-Nano-Integration* 2014, 35-38.
2. Wen L., Zhao H., **Grote F.**, Lei Y.*, Template-based surface nano-patterning and device applications, *Proceedings - IMAPS/ACerS 8th International Conference and Exhibition on Ceramic Interconnect and Ceramic Microsystems Technologies* 2012, 123-131.

Talks

1. **Grote F.**, Lei Y.*, Improving Electrochemical Energy Storage in Supercapacitors by Introducing 3D Nanostructures and Asymmetric Device Configurations, 2st International Conference on Challenges and Perspectives of Functional Nanostructures, July 30-31, 2015, Ilmenau, Germany.
2. **Grote F.**, Lei Y.*, Nano-Engineered Three-Dimensional Core/Shell Nanotube Arrays Towards the Realization of High Performance Micro Electrochemical Capacitors, 5th GMM Workshop on Micro-Nano-Integration, October 08-09, 2014, Ilmenau, Germany.
3. **Grote F.**, Lei Y.*, Improving Electrochemical Energy Storage in Supercapacitors by Introducing Novel Materials, 3D Nanostructures and Asymmetric Device

Scientific contributions

- Configurations, 1st International Conference on Challenges and Perspectives of Functional Nanostructures, July 29-31, 2014, Ilmenau, Germany.
4. **Grote F.**, Wen L., Zhao H., Lei Y.*, Nano-Engineered Three-Dimensional Core/Shell Nanotube Arrays for Realizing High Performance Asymmetric Supercapacitors, 78th Annual Conference of the DPG, March/April 31-04, 2014, Dresden, Germany.
 5. **Grote F.**, Lei Y.*, Nano-Engineered Three-Dimensional Core/Shell Nanotube Arrays for Realizing High Performance Asymmetric Supercapacitors, Institutsseminar der Physik, 2013, TU Ilmenau, Germany.
 6. **Grote F.**, Lei Y.*, Three-Dimensional Nano-Structuring for High Performance Devices, MNI Ilmenau VDI, March 07, 2013, Ilmenau, Germany.
 7. **Grote F.**, Lei Y.*, Three-Dimensional Nano-Structuring for High Performance Bio-Devices, BCube, January 31, 2013, Dresden, Germany.
 8. **Grote F.**, Zhao H., Lei Y.*, Design and Synthesis of Core/Shell SnO₂/MnO₂ Nanotube Arrays for High Performance Supercapacitor Application, 77th Annual Conference of the DPG, March 10-15, 2013, Regensburg, Germany.
 9. **Grote F.**, Wen L., Zhan Z., Al-Haddad A., Mi Y., Tarish S., Wang C., Vellacheri R., Zhao H., Lei Y.*, Realizing Three-Dimensional Nanostructures Using Nano-Templates: Concept, Properties and High Performance Devices, 77th Annual Conference of the DPG, March 10-15, 2013, Regensburg, Germany.
 10. Wen L., Mi Y., **Grote F.**, Al-Haddad A., Zhan Z., Zhao H., Lei Y.*, Nano-Engineered Three-Dimensional Pt/MnO₂ Thin Films for Flexible, High Performance Supercapacitors, 77th Annual Conference of the DPG, March 10-15, 2013, Regensburg, Germany.
 11. **Grote F.**, Mi Y., Zhao H., Lei Y.*, High Performance Super-Capacitors based on Template-Prepared One-Dimensional MnO₂ Nanostructures, 76th Annual Conference of the DPG, March 25-30, 2012, Berlin, Germany.
 12. **Grote F.**, Xu J., Zhao H., Lei Y.*, Template-Fabrication of Highly Ordered MnO₂ One-Dimensional Nanostructure Arrays and their Device Applications as Super-Capacitors, 75th Annual Conference of the DPG, March 13-18, 2011, Dresden, Germany.

Posters

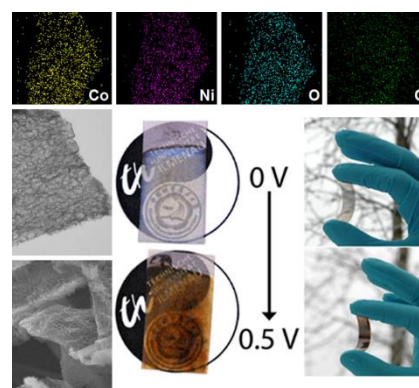
1. **Grote F.**, Lei Y.*, Nano-Engineered Three-Dimensional Core/Shell Nanotube Arrays Towards the Realization of High Performance Micro Electrochemical Capacitors, 5th GMM Workshop on Micro-Nano-Integration, October 08-09, 2014, Ilmenau, Germany.
2. **Grote F.**, Lei Y.*, Template Fabrication of Highly Ordered MnO₂ Nanowire and Nanotube Arrays for Supercapacitor Application, Advanced Automotive Battery Conference, June 18-22, 2012, Mainz, Germany.
3. Zhao H., **Grote F.**, Xu F., Yang S., Lei Y.*, Template-Assisted Growth of Regular Arrays of One Dimensional Nanostructures using Anodic Aluminum Oxide Membranes, 75th Annual Conference of the DPG, March 13-18, 2011, Dresden, Germany.

Extended work

During the process of my Ph.D. I have not only worked on AAO template prepared three-dimensional nanostructures for supercapacitor applications. Moreover, I have been interested in reduced graphene oxide, electrochromic supercapacitors, hydrothermal synthesis, and hydrogen evolution reaction. In particular, during the fruitful exchange programs in the group of Prof. Yu and Prof. Xie within the BMBF project, I had the possibility to learn new techniques and broaden my scientific profile. The scientific visits have resulted in extended works. The abstracts and the table of content figures of the respective papers are presented in this section to highlight the achieved results beyond the scope of this thesis.

1. Self-stacked reduced graphene oxide nanosheets coated with cobalt-nickel hydroxide by one-step electrochemical deposition towards flexible electrochromic supercapacitor (in cooperation with Prof. Yu)

The implementation of an optical function into supercapacitors is an innovative approach to make energy storage devices smarter and meet the requirements of smart electronics. Here, we report for the first time that nickel-cobalt hydroxide on reduced graphene oxide can be utilized for flexible electrochromic supercapacitors. A new and straightforward one-

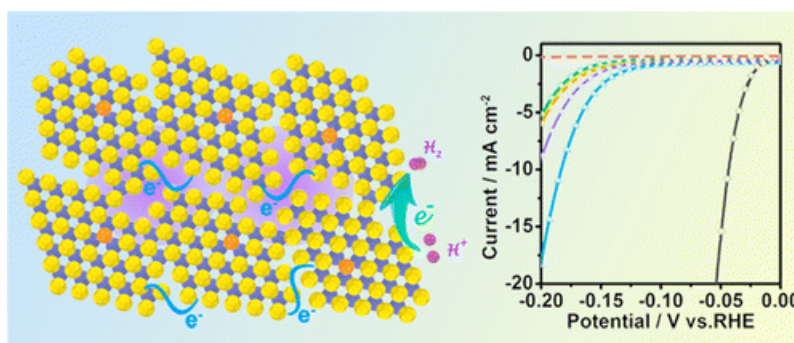


step electrochemical deposition process is introduced that is capable of simultaneous reducing GO and depositing amorphous $\text{Co}_{(1-x)}\text{Ni}_x(\text{OH})_2$ on the rGO. It is shown that the rGO nanosheets are homogeneously coated by metal hydroxide and are vertically stacked. No high temperature processes are used so that flexible polymer-based substrates can be coated. The synthesized self-stacked rGO- $\text{Co}_{(1-x)}\text{Ni}_x(\text{OH})_2$ nanosheet material exhibits pseudocapacitive charge storage behavior with excellent rate capability, high Columbic efficiency and non-diffusion limited behavior. It is shown that the electrochemical behavior of the $\text{Ni}(\text{OH})_2$ can be modulated, by simultaneously depositing nickel and cobalt hydroxide, into broad oxidization and reduction bands. Further, the material exhibits electrochromic property and can switch between a bleached and

transparent state. Literature comparison reveals that the performance characteristics of the rGO-Co_(1-x)Ni_x(OH)₂ nanosheet material, in terms of gravimetric capacitance, areal capacitance and long term cycling stability, are among the highest reported values of supercapacitors with electrochromic property. (*Small* 2015, accepted and in press)

2. Controllable Disorder Engineering in Oxygen-incorporated MoS₂ Ultrathin Nanosheets for Efficient Hydrogen Evolution (in cooperation with Prof. Xie)

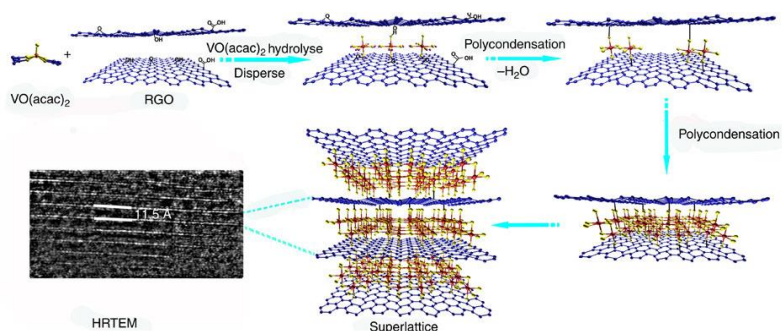
Molybdenum disulfide (MoS₂) has emerged as a promising electrocatalyst for catalyzing protons to hydrogen via the so-called hydrogen



evolution reaction (HER). In order to enhance the HER activity, tremendous effort has been made to engineer MoS₂ catalysts with either more active sites or higher conductivity. However, at present, synergistically structural and electronic modulations for HER still remain challenging. In this work, we demonstrate the successfully synergistic regulations of both structural and electronic benefits by controllable disorder engineering and simultaneous oxygen incorporation in MoS₂ catalysts, leading to the dramatically enhanced HER activity. The disordered structure can offer abundant unsaturated sulfur atoms as active sites for HER, while the oxygen incorporation can effectively regulate the electronic structure and further improve the intrinsic conductivity. By means of controllable disorder engineering and oxygen incorporation, an optimized catalyst with a moderate degree of disorder was developed, exhibiting superior activity for electrocatalytic hydrogen evolution. In general, the optimized catalyst exhibits onset overpotential as low as 120 mV, accompanied by extremely large cathodic current density and excellent stability. This work will pave a new pathway for improving the electrocatalytic activity by synergistically structural and electronic modulations. (*J. Am. Chem. Soc.* 2013, 135, 17881-17888)

3. Magnetocaloric effects in a freestanding and flexible graphene-based superlattice synthesized with a spatially confined reaction (in cooperation with Prof. Xie)

Superlattices have attracted great interest because of their tailorable electronic properties at the interface. However, the lack of



an efficient and low-cost synthetic method represents a huge challenge to implement superlattices into practical applications. Herein, we report a space-confined nanoreactor strategy to synthesize flexible freestanding graphene-based superlattice nanosheets, which consist of alternately intercalated monolayered metal-oxide frameworks and graphene. Taking vanadium oxide as an example, clear-cut evidences in extended X-ray absorption fine structure, high-resolution transmission electron microscopy and infrared spectra have confirmed that the vanadium oxide frameworks in the superlattice nanosheets show high symmetry derived from the space-confinement and electron-donor effect of graphene layers, which enable the superlattice nanosheets to show emerging magnetocaloric effect. Undoubtedly, this freestanding and flexible superlattice synthesized from a low-cost and scalable method avoids complex transferring processes from growth substrates for final applications and thus should be beneficial to a wide variety of functionalized devices. (*Nat. Commun.* 2014, 5, 3960)